APPLICATIONS OF DISTRIBUTED OPTICAL FIBER SENSING BASED ON RAYLEIGH SCATTERING SPECTRUM DEMODULATION

YUYAO WANG

PhD

The Hong Kong Polytechnic University

2024

The Hong Kong Polytechnic University

Department of Electrical and Electronic Engineering

Applications of Distributed Optical Fiber Sensing Based on Rayleigh Scattering Spectrum Demodulation

Yuyao WANG

A thesis submitted in partial fulfillment of the requirements for the degree of Doctor of Philosophy

April 2024

CERTIFICATE OF ORIGINALITY

I hereby declare that this thesis is my own work and that, to the best of my knowledge and belief, it reproduces no material previously published or written, nor material that has been accepted for the award of any other degree or diploma, except where due acknowledgement has been made in the text.

_____ (Signed)

_____Yuyao WANG_____ (Name of student)

Dedicated

To my Families

Abstract

Distributed optical fiber sensors (DOFS) have garnered significant research interest due to their extensive sensing range, immunity to electromagnetic interference, and multi-parameter measurement capabilities. Among these, phase-sensitive optical time domain reflectometers (Φ-OTDR) and optical frequency domain reflectometers (OFDR), which are based on Rayleigh scattering, offer high sensitivity and the advantage of single-ended measurements, presenting substantial application potential. However, practical implementations still face challenges. For example, in spectral demodulated Φ-OTDR, the dynamic range is often constrained by the frequency range of the Rayleigh spectrum, limiting the sensor's application in large parameter measurements. Moreover, traditional DOFS using standard single-mode fibers (SMF) can only measure temperature, strain, and vibration, failing to meet the requirements of diverse parameter measurements in practical applications. This thesis delves into various applications and performance enhancements of spectral demodulated DOFS. The specific research contributions are as follows:

Firstly, we proposed and demonstrated a novel salinity sensor based on frequency scanning Φ-OTDR and polyimide-coated SMF. Leveraging the hygroscopic property of polyimide material and the high sensitivity of Φ-OTDR, we successfully measured salinity with a sensitivity of 782 MHz/(mol/L). To address the cross-sensitivity issue between temperature and salinity unresolved by SMF, we confirmed the feasibility of simultaneous temperature and salinity measurements using polyimide-coated polarization-maintaining fiber (PMF). The fast and slow axes of the PMF were separately interrogated with pulse sequences with orthogonal polarization states, enabling the decoupling of the two parameters with a single fiber. The proposed sensor

achieved temperature sensitivities of -1407.8 MHz/K and -1348.9 MHz/K on the slow and fast polarization axes, and salinity sensitivities of 1028 MHz/(mol/L) and 1008.6 MHz/(mol/L) on the slow and fast polarization axes, respectively. The successful discrimination between salinity and temperature was also verified.

In terms of performance enhancement, we proposed a large dynamic range coherent optical time domain reflectometer (COTDR) based on dual-sideband modulation and a sub-chirped-pulse extraction algorithm (SPEA). We employed a dual-sideband linear frequency modulation (LFM) signal generated by an intensity modulator (IM). The two frequency spectrum sidebands can be recovered with in-phase/quadrature (I/Q) detection and SPEA, thereby doubling the dynamic range of COTDR without compromising the system's bandwidth.

Lastly, we proposed a highly sensitive pressure sensor based on OFDR, assisted by a dual-sideband LFM probe signal and an SMF with a thick acrylic resin coating. Due to the opposite slopes of the LFM signal sidebands, opposite frequency shifts appear in the positive and negative frequency spectrum sidebands. The sensitivity is doubled by subtracting the two frequency shifts. A thick acrylic resin coating enhances the fiber's compressibility, enabling high pressure sensitivity without the need for a special fiber design. A sensitivity of 3979 MHz/MPa and a measurement accuracy of 0.97 KPa are achieved on a 500 m fiber with a 35 cm spatial resolution (SR). The system's rapid responsiveness was also validated through the dynamic measurement of a pressure release process.

Publications

Journal papers:

[1] **Yuyao Wang**, Hua Zheng*, and Chao Lu, High-sensitivity distributed relative salinity sensor based on frequency-scanning φ-OTDR, *Optics Express* 30(13) 22860-22870 (2022).

[2] **Yuyao Wang**, Hua Zheng*, Huan Wu, Dongmei Huang, Changyuan Yu, and Chao Lu, Coherent OTDR with large dynamic range based on double-sideband linear frequency modulation pulse, *Optics Express* 31(11) 17165-17174 (2023).

[3] **Yuyao Wang**, Hua Zheng*, Huan Wu, Dongmei Huang, Changyuan Yu, and Chao Lu, High-sensitivity distributed temperature and salinity sensor based on frequency scanning Φ-OTDR and polyimide-coated polarization maintaining fiber, *Optics & Laser Technology* 175 (2024) 110755.

[4] Hua Zheng, **Yuyao Wang*,** Huan Wu, Dongmei Huang, Changyuan Yu, and Chao Lu, High sensitivity distributed dynamic pressure sensor based on dual-linear frequency modulated optical frequency domain reflectometry. *Optics Letters*, 49(12) 3452-3455 (2024).

[5] Hua Zheng, Huan Wu*, **Yuyao Wang**, et al. High-sensitivity distributed optical fiber sensor for simultaneous hydrostatic pressure and temperature measurement based on birefringent frequency-scanning φ-OTDR, *Optics & Laser Technology* 175 (2024) 110756.

Conference paper:

[1] Yaxi Yan, **Yuyao Wang**, Liwang Lu, et al. Multi-point distributed optical fiber vibration sensing based on forward transmission[C]//2023 Opto-Electronics and Communications Conference (OECC). IEEE, 2023: 1-3.

Acknowledgment

It's time to graduate in the blink of an eye, and as I reflect on my journey, I am filled with gratitude for the invaluable support and guidance I have received from my mentors and friends during my Ph.D. I would like to take this opportunity to express my heartfelt appreciation to all those who have helped me during my Ph.D. stage.

First and foremost, I extend my deepest thanks to my supervisor, Professor Lu Chao, for warmly welcoming me into his group and providing unwavering support throughout my doctoral studies. Over the past four years, Professor Lu's far-sighted thinking and profound expertise in academia have been instrumental in shaping my research path. His rigorous academic attitude serves as a benchmark for my own growth. Beyond academia, Professor Lu embodies kindness and patience, generously sharing his past experiences, guiding me towards a promising future, and encouraging me to seize every opportunity. I am profoundly grateful for his mentorship, and I will forever cherish the guidance he has bestowed upon me.

I would like to express my sincere appreciation to my co-supervisor, Professor Yu Changyuan, for his invaluable guidance, support, and mentorship throughout my academic journey. Professor Yu's profound knowledge, expertise, and dedication have significantly impacted my development as a student and researcher.

I am also immensely grateful to Dr. Zheng Hua, a postdoctoral fellow in the same research group, who introduced me to the fascinating field of distributed optical fiber sensing. Dr. Zheng's guidance and assistance have been invaluable to my research endeavors. Whenever I encountered challenges in experiments or faced difficulties in writing and revising papers, I could always rely on Dr. Zheng's expertise and patient

advice. I extend my sincere appreciation to him for his unwavering support.

Furthermore, I would like to express my gratitude to my colleagues in the research team, whose companionship has made my journey more enjoyable. To Dr. Huang Dongmei, Dr. Wu Huan, Dr. Zhang Jianbo, Dr. Wang Yu, Dr. Wu Xiong, Dr. Yan Yaxi, Dr. Wang Zhuo, Ms. Qu Jiaqi, Dr. Chen Hongjie, Ms. Wang Yue, Mr. Lu Liwang, Mr. Wang Jingchuan, Mr. Fang Zheng, Dr. Cui Jingxian, and Mr. Lo Vincent, I offer my heartfelt thanks. Their tremendous support, both professionally and personally, has left a lasting impact on me. I have felt their warmth and camaraderie throughout, and I am truly grateful for their presence in my life.

I am grateful to my roommate during my doctoral studies, Ms. Qing Yamin. She is a generous, resilient, decisive, and highly adept young individual. As two individuals navigating the unfamiliar terrain of Hong Kong, we have shared the trials of isolation, house-hunting, furnishing our abodes, and facing the challenges of the COVID-19 pandemic. The mutual care and support we have shown each other during these times will undoubtedly be treasured memories in the years to come.

I am appreciative of the understanding and unwavering support of my family, whose unconditional love has allowed me to dedicate myself to my research endeavors. Your love has always been the driving force behind my pursuit of success. The pursuit of a doctoral degree has presented unique challenges for me. However, the setbacks, trials, and lessons accumulated during this journey are undeniably invaluable assets for my future endeavors. I aspire to repay the assistance I have received by contributing meaningfully to my field in the future, thus enriching the significance of my doctoral journey.

Content

List of abbreviations

A

ASE	Amplified spontaneous emission
AWG	Arbitrary waveform generator

B

BDG	Brillouin dynamic grating
BOTDA	Brillouin optical time domain analysis
BPD	Balanced photodetector
BPF	Bandpass filter

C

CDF	Cumulative distribution function
CGP	Concatenately generated phase
COTDR	Coherent optical time domain reflectometer
CRLB	Cramér-Rao lower bound

D

DC	Direct current
DOFS	Distributed optical fiber sensors

E

EDFA	Erbium-doped fiber amplifier
EOM	Electro-optic modulator

F

FBG	Fiber Bragg grating

FDM	Frequency-division multiplexing
FFT	Fast Fourier transform
F-P	Fabry-Perot
FUT	Fiber under test
FWHM	Full width at half maximum

I

I	In-phase
IFFT	Inverse fast Fourier transform
IM	Intensity modulator
IMI	Imbalanced Michelson interferometer
IMZI	Imbalanced Mach-Zehnder interferometer

L

LFM	Linear frequency modulation
LMS	Least mean square
LO	Local oscillator

M

MI	Modulation instability
MZI	Mach-Zehnder interferometer

N

NLL	Narrow linewidth laser

O

OFDR	Optical frequency domain reflectometer
OFS	Optical fiber sensor

OPCR	Optical pulse compression reflectometry
Osc	Oscilloscope
OTDR	Optical time domain reflectometry

P

PBC	Polarization beam combiner
PBS	Polarization beam splitters
PC	Polarization controller
PCF	Photonic crystal fibers
PD	Photodetector
PDF	Probability density function
PGC	Phase-generated carrier
PMF	Polarization-maintaining fiber
PSD	Power spectral density
PSF	Point spread function
PZT	Piezoelectric transducer

Q

Q	Quadrature

R

RBS	Rayleigh backscattering
RF	Radio frequency source
RI	Refractive index

S

SD	Standard deviation

SMF	Single-mode fiber
SNR	Signal-to-noise ratio
SPEA	Sub-chirped-pulse extraction algorithm
SPR	Surface plasmon resonance
SR	Spatial resolution
STFT	Short-time Fourier transform

#

Φ-OTDR	Phase-sensitive optical time domain reflectometers

List of Figures

List of Tables

1 Introduction

1.1 Overview

In 1966, Charles Kuen Kao proposed the use of optical fiber as a waveguide for communication purposes. This concept was successfully brought to life by Corning Corporation in 1970. This marked the beginning of a new era in optical communication, opening up a world of possibilities. As a transmission medium, optical fiber boasts several advantages including low attenuation for long transmission distance, large capacity, and high cost-effectiveness. These benefits have not only spurred the growth of optical fiber communication but have also fostered the development of optical fiber sensors (OFS).

OFS operates by measuring external parameters through the monitoring of phase, intensity, wavelength, and polarization state information of light as it travels through the fiber. Compared to other sensing techniques, OFS offers superior anti-corrosion and anti-electromagnetic interference properties, along with a small size, lightweight, remote sensing, and non-intrusive detection capabilities. To date, OFS has been widely used to measure strain, stress, pressure, temperature, acoustic waves, displacement, and other parameters.

OFS has a broad range of applications, including seismic signal monitoring, road and vehicle monitoring, intrusion detection of protected facilities, and structural health monitoring of bridges, among others [1], [2], [3], [4], [5]. The structures monitored typically cover large spatial ranges or long distances, from several kilometers to tens of kilometers, making them ideal for remote and unattended monitoring. These application scenarios require substantial sensing range, necessitating simultaneous monitoring at

multiple locations. DOFS meet these requirements by enabling spatially resolved measurements of parameters along a single fiber in a continuous manner.

DOFS can be categorized based on their sensing principles into Rayleigh [6], Brillouin [7], [8], and Raman scattering-based DOFS [9], [10]. Of these, Rayleigh scattering-based DOFS is particularly noteworthy for its high accuracy, high sensitivity, and single-end measurement capabilities, which have sparked significant research interest in recent years. The work carried out in the thesis focuses on the DOFS based on Rayleigh backscattering (RBS), conducting a comprehensive study on its performance enhancement and application aspects.

1.1 Research advance in DOFS based on RBS

1.1.1 Optical time domain reflectometry

The concept of optical time domain reflectometry (OTDR) was first introduced in 1976 by Barnoski et al [11]. In this technique, a low-coherence light source is modulated into an optical pulse and injected into the fiber under test (FUT). The RBS light that is generated within the fiber is then detected, allowing for the monitoring and localization of faults in optical fiber links. This groundbreaking development made it possible to detect various issues such as attenuation, connector losses, and points of weak reflection within the fiber by employing the OTDR system. Subsequent advancements in laser technology have led to the development of Φ-OTDR, which uses coherent light sources to measure vibrations along optical fibers. Φ-OTDR leverages a variety of demodulation techniques to interpret the backscattered signal, including intensity demodulation, phase demodulation, and spectral demodulation, which will be expounded upon subsequently.

1.1.1.1 Intensity demodulation

In Φ-OTDR that employs intensity demodulation, the coherence length of the light source is required to exceed the width of the optical pulse. The RBS trace displays random fluctuations due to the interference of Rayleigh backscattered light within the pulse width. Any external disturbance induces alterations in the intensity of the detection trace, rendering it suitable for intrusion detection. In 1994, Juskaitis et al. accomplished the detection of external perturbations on a 30 m SMF using the intensity demodulation technique, achieving a spatial resolution (SR) of 2 m [12].

In Φ-OTDR, the linewidth and frequency stability of the laser play pivotal roles in system performance. A narrow linewidth laser enhances the interference effect of RBS light, thereby enhancing measurement sensitivity. The minimal frequency drift of the laser ensures heightened measurement precision. In 2007, a field test of intrusion detection was conducted using Φ-OTDR, employing an Erbium-doped fiber Fabry-Perot laser with a linewidth of <3 KHz and a frequency drift of a few KHz per second. Intruders on foot and in vehicles were successfully detected on a 19 km sensing fiber, achieving an SR of 100 m [13].

Subsequent studies aimed to enhance the performance of Φ-OTDR. Lu et al. proposed the utilization of moving average and moving differential signal processing in a heterodyne detection Φ-OTDR. A broad frequency wave generated by a pencil break event was identified with an SR of 5 m on a 1.2 km fiber, with the system exhibiting the highest frequency response of 1 KHz [14]. Distributed amplification techniques were incorporated to extend the sensing range by compensating for optical power attenuation during transmission. In 2004, first-order Raman amplification was integrated into Φ-OTDR. Vibration at a frequency of 250 Hz was successfully detected

on a 125 km sensing fiber, achieving an SR of 10 m [15]. Wang et al. proposed a hybrid distributed amplification approach combining second-order Raman amplification, first-order Raman amplification, and Brillouin amplification, enabling an expansion of the sensing range of Φ-OTDR to 175 km with an SR of 25 m [16].

While Φ-OTDR based on intensity demodulation can localize perturbations and provide a preliminary estimation of the perturbation frequency through periodic intensity variations, the nonlinear correlation between intensity alterations and perturbation variations impedes the quantitative measurement of disturbances.

1.1.1.2 Phase demodulation

As the exploration of Φ-OTDR advances, Φ-OTDR based on Rayleigh scattering phase demodulation has piqued increasing interest. Thanks to the direct correlation between phase variation and external perturbations, precise quantification of external disturbances can be achieved through phase demodulation. Various phase demodulation techniques have been developed, including the 3×3 imbalanced Mach-Zehnder interferometer (IMZI) [17], [18], [19], [20], the phase-generated carrier (PGC) method [21], and the dual-pulse approach [22], [23], [24], [25], as depicted in Fig. 1-1.

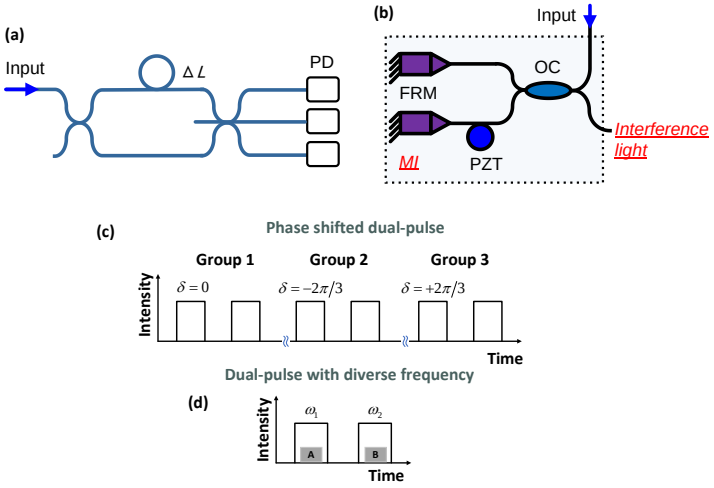

Figure 1-1: (a) 3×3 imbalanced Mach-Zehnder interferometer [20]; (b) Phase-generated carrier [21]; (c) Dual-pulse phase shifted Φ-OTDR [22]; (d) Dual-pulse with diverse frequency Φ-OTDR [23].

The 3×3 IMZI and the PGC method share a common principle of extracting phase information through the interference of two branches of Rayleigh scattered signals with a relative time delay. While IMZI employs a 3x3 coupler to capture three signal branches with phase disparities of 120°, PGC incorporates a piezoelectric transducer (PZT) into one arm of the imbalanced Michelson interferometer (IMI) for self-heterodyne detection of the RBS signal. By leveraging the mathematical relationship between light intensity and phase, the phase can be computed through digital signal processing. The SR of this methodology is contingent upon the gauge length defined by the time delay discrepancy between the interfering arms. However, the utilization of phase demodulation techniques with interferometers complicates the system architecture and necessitates shielding the interferometer structure from external environmental disturbances.

The dual-pulse Φ-OTDR, initially proposed by Dakin et al. in 1990 [24] and later refined by Alekseev et al. in 2014 and 2015 [22], [23], involves injecting a pair of probe pulses with varying phase shifts or frequencies into the FUT. The two pulses are temporally separated to acquire two Rayleigh backscattering signals with a time delay between them. This approach bears resemblance to the PGC and 3×3 IMZI schemes; however, instead of utilizing uneven fiber arms in interferometers to generate the delayed Rayleigh signals, this scheme directly launches two pulses into the FUT to obtain two Rayleigh signals with relative delays.

In the phase-shifted dual-pulse Φ-OTDR [22], three sets of dual pulses are employed, with the second pulse in each set undergoing phase shifts of 0, $-2\pi/3$, and $+2\pi/3$

respectively, as illustrated in Fig. 1-1 (c). Consequently, the interference intensities produced by the three pulse sets are phase-shifted by 120° relative to each other. Subsequently, phase information can be extracted based on the mathematical correlation between optical intensities and phase. Due to the necessity of three pulse sets to construct a phase signal, the frequency response of the phase-shifted dual-pulse method is reduced by a factor of three. In the dual-pulse Φ-OTDR with diverse frequencies (as depicted in Fig. 1-1 (d)) [23], heterodyne detection is achieved by introducing a frequency offset between the two pulses. Through a single launch of the dual pulse, the phase signal is accurately retrieved using the I/Q demodulation technique. Building upon this methodology, He. et al. successfully conducted multiple-event measurements with impressive outcomes, detecting a 1 kHz vibration signal with a low noise level and a remarkable 49.17 dB signal-to-noise ratio (SNR) [25].

This method offers the advantage of eliminating additional interferometric structures, simplifying the system setup, and enhancing measurement stability under environmental perturbations. However, the challenge lies in the inability to reconstruct the complex field of RBS light, which hinders the integration of advanced digital signal processing techniques into this scheme.

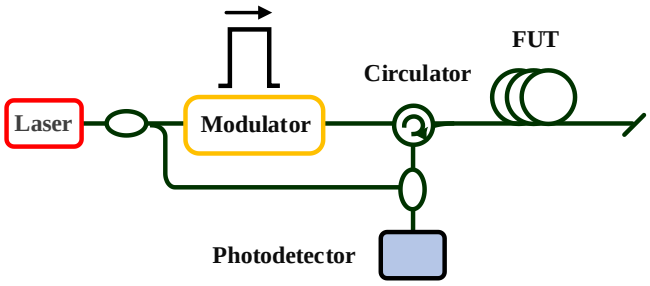

Figure 1-2: Φ-OTDR with heterodyne detection [26].

In 2011, Pan et al. pioneered the application of the digital coherent detection technique in Φ-OTDR [26]. The experimental setup, illustrated in Fig. 1-2, involves the

mixing of the RBS light with the local oscillator (LO) via a 2x2 coupler. This mixture is then detected by a balanced photodetector (BPD). Through digital signal processing, the phase information of the RBS light is extracted, showcasing the technique's effectiveness. In 2016, Wang et al. introduced the I/Q demodulation method to Φ-OTDR, utilizing a 90° optical hybrid and homodyne detection [27]. This innovation, by employing homodyne detection, significantly reduces the bandwidth demands on photodetectors. Their method successfully detected dynamic strain over a 12.56 km FUT with an SR of 10 meters. The integration of digital coherent detection in Φ-OTDR marks a significant advancement. It amplifies the weak RBS light with the strong LO light, substantially enhancing the system's sensitivity. Furthermore, the reconstruction of the RBS light field allows for the application of various sophisticated signal modulation and demodulation techniques. This not only improves the sensing capabilities of Φ-OTDR systems but also opens up new avenues for research and development in the field of optical fiber sensing.

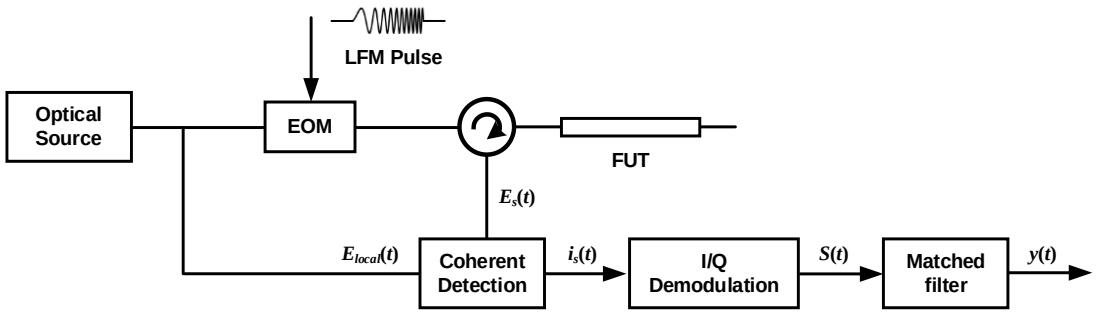

Figure 1-3: Basic setup of OPCR based on pulse compression [28].

In 2015, the innovative optical pulse compression reflectometry (OPCR) technique was introduced, as depicted in Fig. 1-3. This method employs an LFM pulse to interrogate the FUT, while a single-frequency continuous light serves as the LO. The received signal undergoes processing via a matched filter. A key advantage of this technique is that the system's SR is not constrained by the pulse width sent into the FUT.

Instead, it hinges on the bandwidth of the LFM signal, facilitating the simultaneous attainment of high spatial resolution and extended sensing ranges. Utilizing a 221 MHz bandwidth and a 2 ns width LFM signal, researchers achieved a spatial resolution of 47 cm over a 5.4 km fiber span [28]. In the same vein, Wang et al., in 2015, introduced a time-gated digital OFDR for vibration sensing, drawing on principles akin to those of the OPCR technique. Their approach successfully captured a 600 Hz vibration with a spatial resolution of 3.5 m along a 40 km fiber [29].

Further advancements were made to bolster the performance of time-gated digital OFDR. In 2017, frequency-division multiplexing (FDM) technology was integrated into this method to enhance the system's frequency response [30]. By injecting LFM signals covering various frequency bands into the fiber and applying digital matching filters to the backscattered signals, it became possible to differentiate between signals from distinct LFM pulses. This innovation allowed for the coexistence of multiple LFM pulses within the fiber, effectively boosting the sampling rate. As a result, vibration events at frequencies up to 9 kHz were detected on a 24.7 km fiber, achieving an SR of 10 m and an SNR of 30 dB. In 2021, the field saw the proposal of a continuous chirped-wave phase-sensitive OTDR [31]. This technique adeptly leverages both the frequency and time domain properties of the RBS signal, unlocking $p\varepsilon/\sqrt{Hz}$ strain sensitivity, metric spatial resolution, and megahertz sensing bandwidth over kilometer-scale optical fibers. Crucially, in the digital domain, parameters such as spatial resolution, sensing bandwidth, and strain sensitivity can be adjusted flexibly. This adaptability is paramount for pushing the boundaries of DOFS technologies based on RBS, offering new horizons in the exploration of their performance limits.

While Φ-OTDR based on phase demodulation has showcased remarkable

capabilities in distributed acoustic sensing, offering high-frequency response, high spatial resolution, and extended sensing distances, it encounters specific challenges that limit its application scope:

- Despite significant advancements in laser technology that have enabled the production of lasers with very narrow linewidths, phase noise remains an unavoidable issue. For measurements of static or quasi-static parameters, such as temperature and pressure, phase demodulation proves to be ineffective. This limitation underscores the need for alternative sensing techniques when dealing with such parameters.

- The mutual interference among a multitude of scattering points within the probe pulse leads to a phenomenon known as interference fading. This results in very weak interference light intensity at certain positions, potentially causing inaccuracies in phase demodulation outcomes at these locations. To mitigate interference fading, various strategies have been explored, including the use of light at different frequencies to probe the Rayleigh scattering in fibers [32], [33], [34], [35], and the adoption of space-division multiplexed probes in few-mode fibers [36]. Nonetheless, these approaches often necessitate extra bandwidth resources or specific system configurations, presenting a trade-off between performance improvement and system complexity.

- In the phase recovery stage, the periodic nature of trigonometric functions means that phase demodulation results are confined within the range of $[-\pi, \pi]$. To reconstruct the true phase, an unwrapping algorithm must be employed, which requires that the phase difference between adjacent points does not exceed π [37]. This limitation restricts the dynamic range of the system. Although various

unwrapping algorithms [38], [39] and system enhancement methods [40] have been proposed to facilitate the recovery of large signals, they tend to add complexity to the demodulation process or the system as a whole.

1.1.1.3 Spectrum demodulation

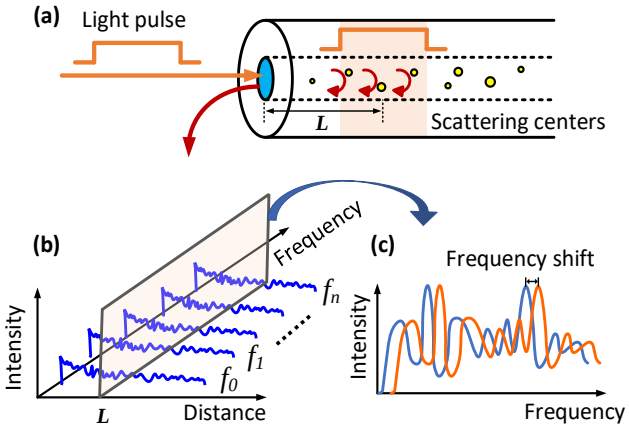

Figure 1-4: Principle of frequency scanning Φ-OTDR [41]. (a) Rayleigh scattering in optical fiber; (b) Detected RBS intensity traces with different optical frequencies;(c) The reference and the measurement RBS spectra.

Spectrum demodulation techniques have emerged as a solution to the limitations associated with phase demodulation methods in distributed sensing. Introduced by Koyamada et al. in 2009 [42], the principle of spectrum demodulation is depicted in Fig. 1-4. This technique involves scanning the frequency of the probing pulses to capture the RBS intensity as a function of both fiber distance and optical frequency. Variations in temperature or strain induce shifts in the Rayleigh spectrum, and by conducting a cross-correlation between the reference and measured spectra, information about these external perturbations can be discerned. While this method allows for non-fading measurements of static parameters with an extensive dynamic range, the necessity of pulse frequency scanning via a microwave synthesizer can significantly prolong the spectrum acquisition time, thus constraining the system's ability to perform dynamic measurements.

To improve the system's frequency response, Liehr et al. employed a distributed feedback laser diode as the light source, modulating the laser current to obtain the Rayleigh scattering spectrum at a fast pace, achieving kHz-range repetition rates [43]. In 2020, Zhang et al. leveraged an arbitrary waveform generator (AWG) to swiftly vary the optical pulse frequency, achieving a sampling rate of 27.8 kHz over a 55 m fiber. They also used a backscatter-enhanced fiber to ensure a high SNR. This approach reduced the noise floor to below $1.8n\varepsilon/\sqrt{Hz}$ for vibrations under 700 Hz and even lower for higher frequencies, all without the need for trace averaging [41].

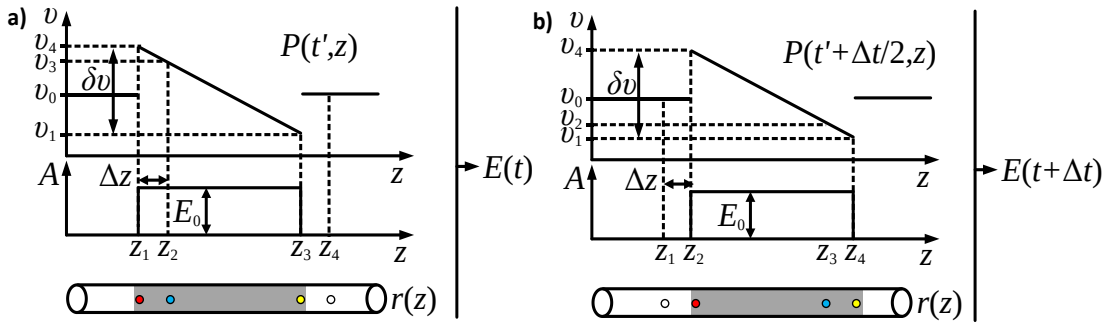

Figure 1-5: Principle of chirped pulse Φ-OTDR [44].

Chirped pulse Φ-OTDR, first reported by J. Pastor-Graells et al. in 2016 and illustrated in Fig. 1-5 [44], introduces a chirped pulse into the FUT, with the Rayleigh signal being directly detected. The phase variation caused by strain results in a temporal shift of the chirped pulse. Cross-correlating the backscattering traces within a time window allows for quantitative demodulation of external disturbances. Chirped pulses negate the need for frequency scanning, enabling single-shot measurements. The system demonstrated a temperature/strain resolution of $1mK/4n\varepsilon$ and a kHz measurement speed, maintaining reliability over extended periods. In 2019, Luis Costa et al. explored the strain sensitivity limit of chirped pulse Φ-OTDR using the Cramér-Rao lower bound (CRLB), employing interpolation strategies and laser noise

compensation to achieve a sensitivity of $10^{-12}\ \varepsilon/\sqrt{Hz}$ over a km-long fiber [45].

The SR of the time delay estimation schemes mentioned is typically dependent on the pulse width, presenting a trade-off between high SR and long sensing distances. In 2020, Xiong et al. proposed a spectral demodulation scheme based on pulse compression, which circumvents this mutual constraint [46]. The SPEA allows for the retrieval of Rayleigh signals across different frequencies. A single measurement is sufficient to acquire the RBS spectrum, and external disturbances are determined by cross-correlating the reference RBS spectrum with the measured spectrum. This method boasts several advantages, including high SR, high SNR, a broad measurement range, resilience to fading, and the capability to measure both static and dynamic parameters. Its superior performance has garnered considerable interest within the research community.

1.1.2 Optical frequency domain reflectometry

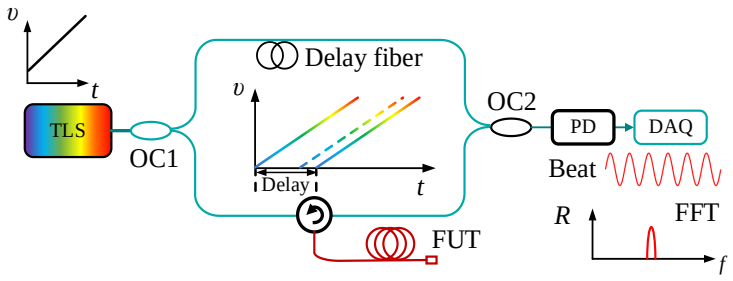

TLS: tunable laser source; OC: optical coupler;
PD: photodetector; DAQ: data acquisition;
FUT: fiber under test;

Figure 1-6: Principle of OFDR [47].

OFDR was first proposed in 1981 [48], with the basic principle illustrated in Fig. 1-6. In this technique, by utilizing a tunable laser source as both the probing light and LO, information on the distribution of Rayleigh scattering along the sensing fiber can be extracted in the frequency domain. The SR of the system is determined by the

bandwidth of the LFM signal. Thanks to the wide spectral range of tunable light sources, OFDR has the capability to achieve millimeter or even sub-millimeter levels of spatial resolution[49], [50], [51], [52].

1.1.2.1 Phase demodulation

Recent advancements in the phase demodulation method of OFDR have underscored its potential in fully exploiting the theoretical SR of OFDR. In 2017, a method involving a 3×3 coupler and a cross-multiply and differentiate phase demodulation technique was introduced to demodulate the phase information of the OFDR signal, with cross-correlation used solely to pinpoint the location of perturbations, achieving an SR of 10 cm [53]. By 2020, a phase demodulation scheme that eschews additional interferometric structures was proposed, relying on the differential relative phase between reference and measurement states [54]. However, the measurable phase range's limitation to just a few radians also restricted the maximum strain range of this method. In 2021, a robust phase unwrapping scheme based on density distribution was reported alongside a phase correlation method to recover coherence deteriorated by fiber deformation, allowing for highly accurate strain measurements with millimeter-level resolution [52].

1.1.2.2 Spectrum demodulation

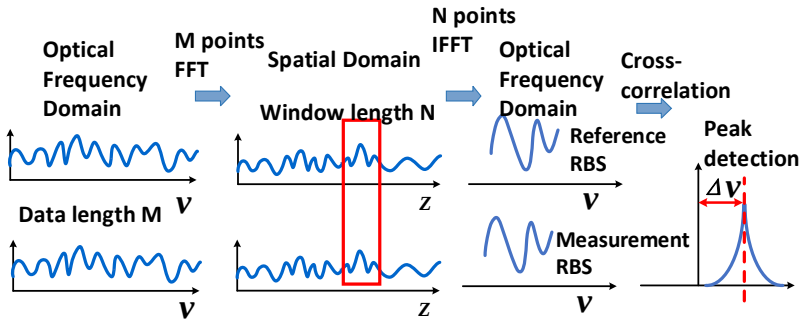

Figure 1-7: Frequency spectrum demodulation process in OFDR [55].

Spectrum demodulation based on cross-correlation was proposed by Froggatt et al. [56] and has been widely accepted and adopted in OFDR sensing. Compared to phase demodulation methods, its superiority is primarily manifested in terms of a large dynamic range and immunity to interference fading. The demodulation process is demonstrated in Fig. 1-7 and as follows:

1: Initially, two measurements are conducted with the OFDR to acquire both the reference signal and the measurement signal.

2: The time-domain reference and measurement RBS traces are converted into spatial domain signals through fast Fourier Transform (FFT);

3: Selecting a gauge length in the spatial domain with a sliding window. The length of the window determines the SR of the system.

4: Padding zeros in the selected RBS signals in the spatial domain and subsequently using inverse fast Fourier transform (IFFT) converts each local RBS signal to the optical spectrum domain.

5: The cross-correlation between the reference spectrum and the measurement spectrum is computed, leading to the determination of the frequency shift, which signifies external strain or temperature variations.

The presence of phase noise in the laser is a critical element that significantly impacts the efficacy of OFDR. On one hand, the frequency tuning nonlinearity contributes to the broadening of the system's point spread function (PSF), leading to decreased positioning accuracy. On the other hand, random phase noise diminishes the coherence of the light source. As the sensing distance extends, not only does the PSF widen, but its amplitude also experiences an exponential decline, resulting in a severe degradation of the system's performance. Extensive efforts have been dedicated to mitigating phase noise in OFDR [47], [57]. Various compensation methods have been proposed,

including frequency sampling [58], [59], [60], resampling algorithms [61], [62], [63], [64], [65], the concatenately generated phase (CGP) approach [66], [67], [68], [69], [70], and the deskew filter [71], [72].

The frequency sampling method introduces an auxiliary interferometer into OFDR, utilizing the zero-crossing points of the signal from the auxiliary interferometer to trigger data acquisition in the main interferometer. While this technique eliminates the need for post-processing of data, the system's measurement range is limited by the length of the delay fiber in the auxiliary interferometer. To overcome this constraint, various resampling methods have been proposed. In the resampling process, signals from both the auxiliary interferometer and the main interferometer are collected. Subsequently, leveraging the frequency information from the signals in the auxiliary interferometer, interpolation or resampling is applied to the signal in the main interferometer to achieve uniform frequency interval sampling. These interpolation algorithms include cubic spline interpolation [64], [73], non-uniform fast Fourier transform [65], among others. However, the resampling algorithm cannot completely eliminate the nonlinearity tuning effects of the light source and may not perform optimally over long distances.

The "CGP" scheme, proposed by Fan et al. in 2007, involves segmenting the sensing fiber into multiple sections, with each section's laser phase noise compensated using different CGPs [66], [67], [68], [69]. This method ultimately achieved a spatial resolution of 7 cm on a 100 km fiber. The drawback of this scheme is that the compensation performance deteriorates when it deviates from the optimal compensation point. The deskew filter algorithm, introduced by Ding et al. in OFDR, compensates for frequency nonlinearity across the entire fiber in a single operation [71]. In experiments, this method achieved a spatial resolution of 1.6 m on an 80 km fiber.

In 2014, the same group optimized the deskew filter with a more accurate nonlinear phase estimation method, the spatial resolution was improved to 2 times and the reflectivity was enhanced by 5 dB compared with the previous deskew filter [72].

Although the resampling algorithm and phase noise compensation schemes have enhanced SR and measurement range, these approaches involve computationally intensive processes and rely on auxiliary interferometers, thereby increasing system complexity. In 2021, Xiong et al. utilized a narrow linewidth laser and I/Q modulator to generate an LFM signal, achieving an SR of 28.4 cm and a dynamic range of 60 $\mu\varepsilon$ for strain measurements on a 920 m fiber [74]. This method does not require the use of auxiliary interferometers or compensation algorithms, effectively addressing the phase noise issue in OFDR from the source.

1.2 Distributed optical fiber salinity/pressure sensing

Despite the significant advancements in distributed fiber optic sensing technology, the current scope of measurable parameters remains largely confined to temperature, strain, and vibration, indicating a narrow application range. However, research into the measurement of new parameters is crucial to address the sensing requirements of diverse application scenarios.

The measurement of salinity is particularly critical in disciplines such as oceanography, climate research, and the management of oceanic resources. Despite its importance, reports on distributed salinity sensing are scarce. A notable development occurred in 2020 when Zhang et al. pioneered the measurement of distributed salinity. They utilized Brillouin dynamic gratings (BDG) in conjunction with polyimide-coated photonic crystal fibers (PCF) to achieve this feat. Their method, however, yielded a sensitivity of only 139.6 MHz per mol/L and a measurement accuracy of 0.072 mol/L

[75]. While this was a significant step forward, the sensitivity and precision achieved may not meet the stringent requirements necessary for certain practical applications. Further research and development are needed to enhance the performance of distributed salinity sensing techniques to fulfill the demands of high-precision measurements in various industrial domains.

Pressure measurement is a critical aspect in a variety of sectors, including oil and gas exploration, transportation, and the monitoring of pore water pressure within geotechnical structures [76], [77]. To date, sensors based on both Brillouin and Rayleigh scattering have been developed for distributed salinity sensing. In 2016, a pressure sensor that combined BDG with a thin-diameter polarization-maintaining PCF was successfully demonstrated, achieving a sensitivity of 199 MHz/MPa and a measurement error of less than 0.03 MPa [78]. In light of the complexity associated with the BDG system, a more straightforward pressure sensor employing Brillouin optical time domain analysis (BOTDA) was introduced in 2020. This sensor, featuring a double-layer polymer coating, attained a sensitivity of -3.61 MHz/MPa and a measurement error of 0.09 MPa [79]. Despite these innovations, the pressure sensitivities of Brillouin scattering-based DOFS are still somewhat limited. To overcome this challenge, pressure sensors utilizing Φ-OTDR have been developed, showing promising high sensitivities and measurement accuracies. For example, Φ-OTDR systems incorporating high birefringent PCF [80] or elliptical core fiber with side air holes [81] have achieved sensitivities of -2190 MHz/MPa and 1590 MHz/MPa, respectively. These developments mark a significant enhancement in pressure sensitivity over Brillouin scattering-based DOFS. Despite these advancements, there has been a noticeable gap in the reporting of dynamic pressure measurements. Addressing this, Qiu et al. in 2022 successfully achieved dynamic pressure

measurement using Φ-OTDR with a standard SMF, reaching a sampling rate of 33.3 kHz and an SR of 2 m [82]. It is important to note, however, that the sensitivity of 702.5 MHz/MPa reported in this study is considerably lower than those obtained with specialized fibers. Therefore, further research is needed to develop dynamic pressure sensing techniques that can achieve high sensitivities and measurement accuracies. This will enable more effective monitoring and control of dynamic pressure variations across various industries and applications.

1.3 Research objectives and organization of the thesis

In examining the current challenges and future directions of DOFS utilizing Rayleigh scattering spectrum demodulation, several key issues emerge that necessitate resolution:

1) In spectral demodulation schemes, the dynamic range of the system's measurable parameters within the spectrum demodulation scheme is confined by the scope of the Rayleigh spectrum. When employing LFM signals alongside pulse compression techniques, the bandwidth of the LFM signal determines the system's dynamic range. Consequently, as the demand for a broader dynamic range escalates, both the AWG and the optical receiver are required to support higher bandwidths. This requirement precipitates a notable escalation in the overall system costs.
2) Presently, the bulk of salinity sensing research is anchored in DOFS that leverage Brillouin scattering. This approach, however, is hampered by limited sensitivity, necessitating the use of specialized optical fibers to achieve enhanced sensitivity. The exploration into leveraging Φ-OTDR for high-sensitivity distributed salinity

sensing is still at a nascent stage.

3) There is room for improvement in dynamic pressure measurement, particularly in terms of sensitivity, measurement accuracy, and spatial resolution, within the existing sensing schemes. Further research and technological breakthroughs are required in this area.

This thesis is dedicated to enhancing the performance of DOFS systems and broadening their application spectrum beyond the traditional realms of temperature, strain, and vibration measurements. The research objectives are outlined as follows:

- To achieve high-sensitivity salinity measurement utilizing a frequency scanning Φ-OTDR in conjunction with a polyimide-coated SMF. To mitigate the issue of temperature cross-sensitivity in salinity measurements, PMF will be utilized to differentiate between these two parameters effectively.
- To extend the dynamic range of Φ-OTDR systems based on SPEA through the implementation of dual-sideband modulation and I/Q detection techniques. This approach aims to double the dynamic range without necessitating an increase in system bandwidth.
- To develop a high-sensitivity distributed dynamic pressure sensor by employing a dual-sideband modulated OFDR alongside a coating thickness-enhanced SMF. The utilization of both positive and negative sidebands will yield two counteracting frequency shifts, effectively doubling the sensor's pressure sensitivity. Additionally, the application of a thicker coating on the fiber is anticipated to further augment sensitivity.

The structure of this thesis is organized as follows:

Chapter 1 provides an overview of the application value and advantages inherent in DOFS. It proceeds to offer a comprehensive review of existing Rayleigh scattering-based DOFS methodologies, highlighting the challenges these systems encounter and proposing strategies for improvement. The chapter concludes by presenting the research motivation and the thesis's organizational framework.

Chapter 2 delves into the fundamental principles underpinning DOFS that utilize Rayleigh spectrum pattern demodulation. The chapter begins by explaining the Rayleigh scattering mechanism and its statistical characteristics within optical fibers. Subsequently, it discusses the temperature and strain sensitivities of optical fibers. The chapter then thoroughly examines the principles of spectral demodulated DOFS, including frequency-scanning Φ-OTDR, Φ-OTDR based on the pulse compression technique, and OFDR.

Chapter 3 introduces a novel salinity sensor that leverages a polyimide-coated fiber in conjunction with frequency scanning Φ-OTDR technology. Initially, the feasibility of the proposed sensor design is validated using a polyimide-coated SMF. With a coating thickness of 15 μm, the sensor achieves a salinity sensitivity coefficient of 782 MHz/(mol/L). To overcome the issue of cross-sensitivity between salinity and temperature, the chapter proposes a dual-parameter measurement scheme using polyimide-coated PMF. The PMF's two orthogonal polarization axes exhibit distinct sensitivity coefficients to temperature and salinity, enabling the differentiation of these parameters. Experimental results validate the sensor's capability to discriminate

between temperature and salinity with measurement accuracies of 0.0344 K and 0.0469 mol/L, respectively, over a 100-meter fiber span.

Dynamic range is a critical attribute for DOFS systems. In Chapter 4, we address the limitations in dynamic range imposed by the frequency span of LFM pulses in spectrum pattern demodulated Φ-OTDR. The chapter presents an Φ-OTDR system with an enhanced dynamic range that utilizes a dual-sideband LFM signal. By employing an intensity modulator and a 2x4 optical hybrid, the system generates a dual-sideband LFM signal and recovers the complex optical field of the dual-sideband RBS signal. This approach allows for the full utilization of the system's bandwidth, achieving a dynamic strain measurement of 3.09 $\mu\varepsilon$, which corresponds to a frequency shift of 461 MHz, using the proposed method.

Chapter 5 showcases the development and testing of a high-sensitivity pressure sensor that employs a dual-sideband OFDR technique, combined with a thick acrylic resin-coated SMF. Initially, the theory of the dual-sideband linear frequency modulated OFDR and the effects of pressure-induced strain on the fiber are elaborated first. Following the theoretical overview, the chapter presents experimental results, including the measurement of pressure sensitivity and the sensor's performance in dynamic pressure scenarios. Remarkably, the sensor achieved a pressure sensitivity of 3979 MHz/MPa, and was capable of sampling dynamic pressure at a rate of 1.25 KHz, demonstrating its potential for high-precision applications.

Chapter 6 provides a comprehensive conclusion of the research conducted and outlines future research directions.

2 Basic Principles of Distributed Optical Fiber Sensors Based on Rayleigh Scattering

2.1 Mechanism of Rayleigh scattering

Rayleigh scattering occurs when the dimensions of the scattering particles are significantly smaller than the wavelength of the incident light, typically less than one-tenth of the wavelength. As light propagates through a medium with density fluctuations, the electromagnetic field of the optical wave interacts with the electrons in the particles, causing them to oscillate at the same frequency as the incident light. This oscillation induces the formation of electric dipoles within the particles. These dipoles, in turn, cause the incident light waves to scatter and deviate from their original path. This phenomenon is known as Rayleigh scattering. Since the frequency of the incident light remains unchanged during this interaction, Rayleigh scattering is classified as a form of elastic scattering.

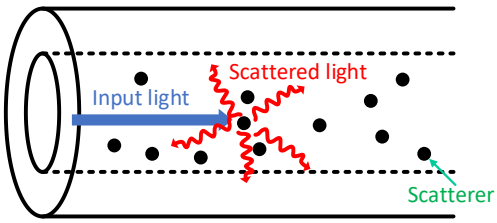

Figure 2-1: A schematic of Rayleigh scattering in fiber [83].

As depicted in Figure 2.1, optical fibers contain a multitude of scatterers. These scatterers originate during the fiber manufacturing process, where the glass material is cooled and solidified into the fiber structure. However, this cooling process is not

flawless and can result in variations in density and composition throughout the fiber. Such nonuniformities may arise from several factors, including inconsistent mixing of the materials, the presence of impurities, or variations in the cooling rate. When light is introduced into the fiber, it interacts with these inhomogeneities, leading to Rayleigh scattering in all directions. According to reference [84], the Rayleigh scattering coefficient in fiber can be mathematically expressed as follows:

$$\gamma_R = \frac{8\pi^3}{3\lambda^4} n^8 p^2 \beta_T KT \tag{2-1}$$

where λ is the wavelength of the incident light, n is the refractive index (RI) of the fiber core, p represents the average photoelastic coefficient, K is the Boltzmann constant, T and β_T are fictive temperature and the isothermal compressibility at T, respectively. For a standard SMF-28, the parameters take these values: n=1.46, p=0.286, $K = 1.38\times10^{-23} JK^{-1}$, T=1950 K, $\beta_T = 7\times10^{-11} m^2 N^{-1}$. The above equation indicates that the Rayleigh scattering intensity is inversely proportional to $1/\lambda^4$. Only a fraction of scattering light can be recaptured and propagates backward in the fiber. The power of Rayleigh backscattering light can be expressed as [85], [86]:

$$P_R = PS\gamma_R \frac{vT_p}{2} \tag{2-2}$$

where $S = \left(\lambda/\pi nw\right)^2/4$ is the recapture factor, w is the Gaussian beam spot size, P is the optical power of incident light, v is the velocity of light, and T_p is the temporal width of the optical pulse. In a common standard SMF, the optical fiber loss at 1550 nm is between -50 to -40 dB per meter ($\approx 4.5\times10^{-5}$ m^{-1}).

2.2 Statistical properties of Rayleigh scattering in fiber

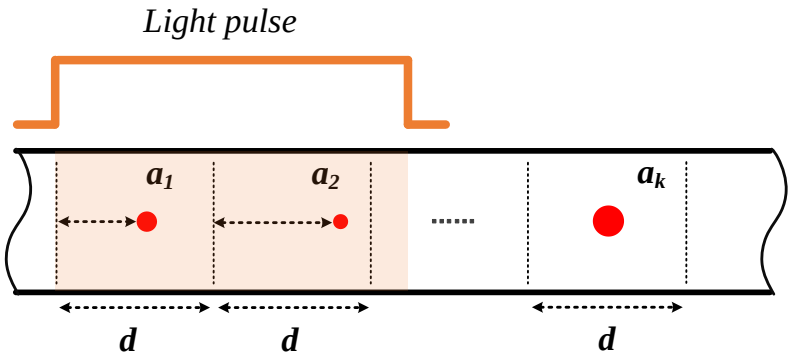

Figure 2-2: Discrete model of Rayleigh scattering in optical fibers.

In optical fibers, there are a large number of scattering points. To simplify the model, Healey et al. characterized the inhomogeneities in fibers as one-dimensional distributed scatterers with statistically independent random reflectivity, as illustrated in Fig. 2-2 [87]. The fiber is segmented into a series of scattering centers with an equal distance *d*, where *d* is smaller than the wavelength of the incident light according to the Rayleigh scattering hypothesis. Each scattering center can be viewed as an independent reflecting mirror, with its position randomly distributed within the scattering centers. The reflected light from the k-th scattering center can be expressed as:

$$\boldsymbol{r}_k = \boldsymbol{p}_k a_k \exp\left(j\phi_k\right) \tag{2-3}$$

where $\boldsymbol{p}_k$ is the polarization state of the RBS light, a_k and ϕ_k are the amplitude and phase of backscattering light, respectively. Assuming the fiber attenuation coefficient is α, a random vector process can be utilized to model the unit-impulse response of the fiber:

$$\boldsymbol{h}(t) = \exp(-\alpha v t)\sum_k \boldsymbol{p}_k a_k \delta(t - t_k) \tag{2-4}$$

$\delta(t-t_k)$ is the Dirac function which equals 1 when $t = t_k$, and 0 otherwise. t_k is the round-trip time delay of the RBS light generated by the k-th scatterer which can be

obtained by the effective location of the k-th scatterer z_k and the group velocity of light wave v:

$$t_k = 2z_k / v \tag{2-5}$$

Supposing an excitation pulse signal with an amplitude of e and an angular frequency of ω is injected into fiber:

$$x(t) = e(t)\cos\left[\omega t - \phi(t)\right] \tag{2-6}$$

where $\phi(t)$ is the random phase noise. The $x(t)$ can be regarded as a scalar here since the polarization factor has already been taken into account in the impulse response mentioned in Eq. (2-4). When the coherence time of the light source Δ is smaller than the pulse width, the excitation signal can be divided into multiple sections $x_i(t)$ with a duration equal to the laser coherence time:

$$x(t) = \sum_i x_i(t) = \sum_i e(t - i\Delta)\cos\left[\omega_i(t - i\Delta) - \phi_i\right] \tag{2-7}$$

Within each section, the fields generated by different scatterers must be considered as vectors due to the presence of a stable, albeit random, relative phase between them. Consequently, the superposition of scattered light is a vectorial process, where the outcome is influenced by the relative phase of the scattering light. This vectorial superposition can lead to either constructive or destructive interference, thereby amplifying or diminishing the intensity of the light. However, it is important to note that the light intensity from one section cannot be coherently superimposed with that from another section, as they are statistically independent. In such cases, the optical powers from different sections are incoherent and, therefore, can be simply summed to obtain the total power.

By convolving the unit-impulse response $\boldsymbol{h}(t)$ and the excitation pulse signal $x(t)$,

we can obtain the Rayleigh backscattering wave:

$$\begin{aligned} y(t) &= x(t) * h(t) \\ &= \sum_i x_i(t) * h(t) = \sum_i y_i(t) \end{aligned} \tag{2-8}$$

The above equation suggests that the backscattering signal $y(t)$ is the result of the superposition of statistically independent field components originating from randomly distributed numerous scatterers. The light intensity can be expressed as:

$$I(t) = \sum_i I_i(t) = \sum_i |y(t)|^2 \tag{2-9}$$

where M_f is the number of statistically independent waves (degree of freedom). The probability density function (PDF) of the RBS light intensity follows a gamma distribution [88], [89]:

$$P_I(I) = \frac{I^{M_f - 1}}{(M_f - 1)!} \left(\frac{M_f}{\bar{I}} \right)^{M_f} \exp\left(-\frac{M_f I}{\bar{I}} \right) \tag{2-10}$$

The PDF with different M_f is shown in Fig. 2-3. In COTDR, a narrow linewidth laser (NLL) source is typically employed. When utilizing a single-frequency laser source with a single polarization state, the degree of freedom is equal to 1. Under this condition, all scattered light within the pulse width remains coherent, and the statistical characteristic of the light intensity adheres to an exponentially decaying function. Consequently, the intensity of the RBS signal is characterized by a jagged pattern, displaying random and significant fluctuations over distance, with the intensity being low at most positions along the fiber. The weakest point in the RBS trace, known as fading, can lead to the failure of external perturbation measurement in phase demodulated Φ-OTDR, as the signal intensity at this point is nearly zero. As illustrated in Fig. 2-3, an increase in the degrees of freedom results in a more concentrated PDF

and reduced fluctuations in the RBS trajectory. This observation provides a theoretical basis for strategies aimed at mitigating the effects of coherent fading.

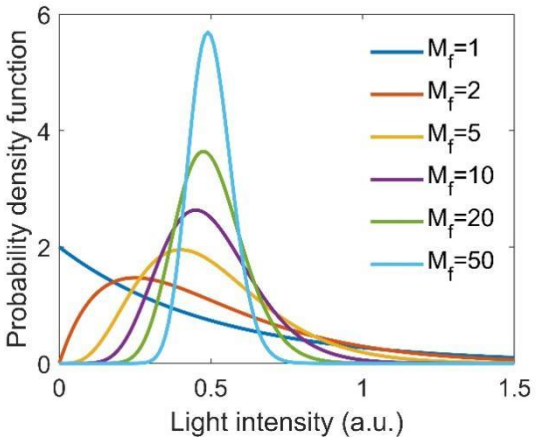

Figure 2-3: PDF with different M_f [89].

As elaborated in Eq. (2-8), the backscattering optical field is the summation of all the scattering signals within the pulse width. It can be modeled as a zero-mean circular complex Gaussian variable, with the real part and imaginary part being uncorrelated and both following a Gaussian distribution [90], [91], [92]. The joint PDF of the real part R and imaginary part I is:

$$P\left(E_R, E_I\right) = \frac{1}{2\pi\sigma^2}\exp\left(-\frac{E_R^2 + E_I^2}{2\sigma^2}\right) \tag{2-11}$$

where σ is the variance. The joint PDF for amplitude $|E|$ and phase θ of the backscattering signal can be derived by the relation $E_R = |E|\sin\theta$ and $E_I = |E|\cos\theta$ [93]:

$$P\left(|E|, \theta\right) = \frac{|E|}{2\pi\sigma^2}\exp\left(-\frac{|E|^2}{2\sigma^2}\right) \tag{2-12}$$

Since the amplitude $|E|$ and phase θ of the backscattering optical field are statistically independent, the amplitude follows a Rayleigh distribution, while the phase is uniformly distributed within a range of $[-\pi, \pi]$:

$$P(|E|) = \int_{-\pi}^{\pi} P(|E|,\theta) d\theta = \frac{|E|}{\sigma^2} \exp\left(-\frac{|E|^2}{2\sigma^2}\right), \text{ and} \tag{2-13}$$

$$P(\theta) = \int_{0}^{\infty} P(|E|,\theta) d|E| = \frac{1}{2\pi} \tag{2-14}$$

2.3 Temperature and strain sensitivities of Rayleigh spectrum

When the light propagates in a fiber, the phase can be expressed as:

$$\phi = \frac{2\pi v n L}{c} \tag{2-15}$$

where v denotes the optical frequency, n is the RI of the fiber core, L represents the fiber length, and c stands for the velocity of light in a vacuum, respectively. External perturbations can induce variations in fiber RI and length of the fiber. By adjusting the frequency of the light source, the phase variation caused by external perturbations can be compensated. In the following, the temperature and strain sensing principles will be elaborated in detail.

- **Temperature sensitivity**

Temperature affects the optical phase in two ways: fiber length variation caused by thermal expansion or contraction, and RI variation due to the thermo-optic effect. The relationship between phase variation $\Delta\phi_T$ and temperature change ΔT can be expressed as follows [92], [94]:

$$\frac{\Delta\phi_T}{\Delta T} = \frac{2\pi v n L}{c}\left(\frac{1}{L}\frac{dL}{dT} + \frac{1}{n}\frac{dn}{dT}\right) \tag{2-16}$$

In the given equation, the effect of fiber diameter variation has been disregarded. Within the parentheses, the first term represents the thermal expansion coefficient,

while the second term denotes the thermo-optic coefficient. For silica fiber, typical values for these coefficients are approximately:

$$\frac{1}{L}\frac{dL}{dT} = 4.5\times10^{-7}K^{-1} \tag{2-17}$$

$$\frac{1}{n}\frac{dn}{dT} = 2\times10^{-5}K^{-1} \tag{2-18}$$

Based on the above equations, it is evident that the phase change resulting from thermal expansion is considerably smaller compared to the thermo-optic effect. Hence, the thermal expansion coefficient is typically negligible. In the present study, the focus lies on the Rayleigh spectrum shift induced by temperature. A commonly used parameter to quantify this sensitivity is the temperature sensitivity coefficient, which can be expressed as:

$$\frac{\Delta\nu}{\Delta T} = \frac{\nu}{n}\frac{dn}{dT} \approx 1.33 GHz/K \tag{2-19}$$

- **Strain sensitivity**

The phase change $\Delta\phi_s$ induced by strain ε can be written as [92], [95]:

$$\Delta\phi_s = \frac{2\pi\nu}{c}\left(n\varepsilon L + L\Delta n(\varepsilon)\right) \tag{2-20}$$

wherein the first term and the second term represent the strain-induced variation in fiber length and the strain-induced variation in fiber refractive index (known as the strain-optic effect), respectively. In this context, the strain-induced change in fiber diameter is disregarded due to its relatively small magnitude compared to the other two terms. The strain-optic effect results in a change in the optical indicatrix:

$$\Delta\left(\frac{1}{n^2}\right)_i = \sum_{j=1}^{6} p_{ij}S_j \tag{2-21}$$

where p_{ij} and S_j denote the photoelastic tensor and the strain vector, respectively. When considering the longitudinal strain, the strain vector can be expressed as:

$$S_j = [\varepsilon \quad -\mu\varepsilon \quad -\mu\varepsilon \quad 0 \quad 0 \quad 0] \tag{2-22}$$

here μ is the Poisson's ratio. For a homogeneous isotropic medium, the strain-optic tensor p_{ij} is given by:

$$p_{ij} = \begin{bmatrix} p_{11} & p_{12} & p_{12} & 0 & 0 & 0 \\ p_{12} & p_{11} & p_{12} & 0 & 0 & 0 \\ p_{12} & p_{12} & p_{11} & 0 & 0 & 0 \\ 0 & 0 & 0 & p_{44} & 0 & 0 \\ 0 & 0 & 0 & 0 & p_{44} & 0 \\ 0 & 0 & 0 & 0 & 0 & p_{44} \end{bmatrix} \tag{2-23}$$

where $p_{44} = (p_{11} - p_{12})/2$. Hence, the optical indicatrix change in *y* and *z* directions (*i*=2,3) caused by strain is:

$$\Delta\left(\frac{1}{n^2}\right)_{2,3} = \varepsilon(1-\mu)\,p_{12} - \mu\varepsilon\,p_{11} \tag{2-24}$$

The refractive index change for light propagating in the *x* direction can be expressed as:

$$\Delta n(\varepsilon) = -\frac{1}{2}n^3\Delta\left(\frac{1}{n^2}\right)_{2,3} = \frac{1}{2}n^3\left[\varepsilon(1-\mu)\,p_{12} - \mu\varepsilon\,p_{11}\right] \tag{2-25}$$

Substituting Eq. (2-25) into Eq. (2-20), we can get:

$$\Delta\phi_s = \frac{2\pi v n L\varepsilon}{c}\left\{1 - \frac{1}{2}n^2\left[(1-\mu)\,p_{12} - \mu p_{11}\right]\right\} \tag{2-26}$$

Taking $n = 1.5$, $\mu = 0.17$, $p_{11} = 0.11$, and $p_{12} = 0.25$, the frequency shift caused by the longitudinal strain can be deduced:

$$\frac{\Delta v}{\varepsilon \times 10^{-6}} = v\left\{1 - \frac{1}{2}n^2\left[(1-\mu)\,p_{12} - \mu p_{11}\right]\right\} = 152.44 \text{ MHz}/\mu\varepsilon \tag{2-27}$$

2.4 Φ-OTDR based on frequency scanning

2.4.1 Basic principle of frequency scanning Φ-OTDR

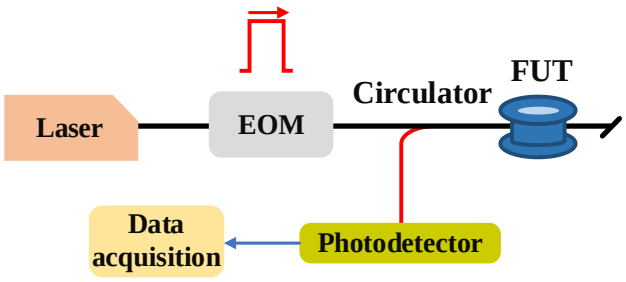

Figure 2-4: Basic configuration of Φ-OTDR.

Fig. 2-4 shows the basic configuration of a direct detection Φ-OTDR. The continuous light emitted by the laser is chopped into an optical pulse and frequency shifted by an electro-optic modulator (EOM). The light pulse is launched into the FUT and then the RBS signal is guided into a photodetector (PD) through the circulator. Finally, the RBS signal is digitalized and processed. Assuming the optical field of the pulse to be:

$$p_0(t) = A(t)\exp\{j\varphi(t)\} \tag{2-28}$$

where $A(t)$ and $\varphi(t)$ are the amplitude function and the phase function defined by:

$$\varphi(t) = 2\pi(v_0 + f)t \tag{2-29}$$

$$A(t) = rect\left(\frac{t}{T_p}\right) \tag{2-30}$$

where v_0 is the optical carrier frequency, f and T_p denote the modulation frequency and the pulse width, respectively. We assume that the number of scatterers is N_s, and each scatterer is characterized by its amplitude a_i and time delay τ_i. The time delay can be calculated based on the distance z_i:

$$\tau_i = \frac{2nz_i}{c} \tag{2-31}$$

The Rayleigh backscattering light field is the summation of the reflected light fields from all scatterers within the pulse width [42]:

$$\begin{aligned} E(t, f) &= \sum_{i=1}^{N_s} a_i \exp\left(-\alpha \frac{c\tau_i}{n}\right) p_0(t-\tau_i) \\ &= \sum_{i=1}^{N_s} a_i \exp\left(-\alpha \frac{c\tau_i}{n}\right) \exp\left\{ j2\pi(v_0 + f)(t-\tau_i)\right\} rect\left(\frac{t-\tau_i}{T_p}\right) \end{aligned} \tag{2-32}$$

in which α denotes the fiber attenuation coefficient. The intensity of the RBS signal can be obtained using the direct-detection method:

$$\begin{aligned} I(t, f) &= R_{PD} \left| E(t, f) \right|^2 \\ &= R_{PD} \sum_{i=1}^{N_s} a_i^2 \exp\left(-2\alpha \frac{c\tau_i}{n}\right) rect\left(\frac{t-\tau_i}{T_p}\right) \\ &\quad + 2R_{PD} \sum_{i=1}^{N_s} \sum_{j=i+1}^{N_s} a_i a_j \cos\varphi_{ij} \exp\left(-\alpha \frac{c(\tau_i + \tau_j)}{n}\right) \times rect\left(\frac{t-\tau_i}{T_p}\right) rect\left(\frac{t-\tau_j}{T_p}\right) \end{aligned} \tag{2-33}$$

where R_{PD} is the responsivity of the photodetector, $\varphi_{ij} = 2\pi(v_0 + f)(\tau_i - \tau_j)$, representing the phase difference between the *i*-th and *j*-th backscattering waves. The first term in Eq. (2-33) represents the sum of the optical power of scattering light, which remains unchanged with variations in external temperature or fiber strain. The second term in Eq. (2-33) involves the interference of Rayleigh backscattered light generated by different scatterers, resulting in a speckle pattern of intensity trajectories. This speckle pattern is the phenomenon of interest. Eq. (2-33) describes the Rayleigh scattering intensity $I(t, f)$ as a two-dimensional function of time *t* and frequency *f*, and is commonly referred to as the Rayleigh scattering pattern. The Rayleigh scattering pattern $I(z, f)$ as a function of distance and frequency can be obtained through the

relationship between the time and distance: $z = ct/2n$, as shown in Fig. 2-5.

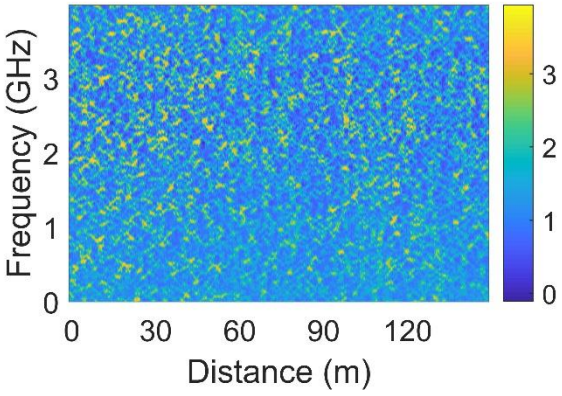

Figure 2-5: The Raleigh scattering pattern.

According to Eq. (2-15), the phase difference φ_{ij} can also be expressed as:

$$\varphi_{ij} = \frac{4\pi n(v_0 + f)(z_i - z_j)}{c} = \frac{4\pi n(v_0 + f) z_{ij}}{c} \tag{2-34}$$

From the Eq. (2-34), it is evident that φ_{ij} is directly proportional to the RI, optical frequency, and the separation distance between scatterers. Both the RI and the separation distance are susceptible to variations induced by temperature and strain. By adjusting the optical frequency, it is possible to counteract the phase alterations triggered by temperature and strain changes, thereby restoring the intensity of the RBS light. As illustrated in Fig. 2-6, the impact of temperature and strain is manifested as a frequency shift within the spectrum.

To accurately demodulate the frequency shift observed between the reference spectrum and the measurement spectrum, the cross-correlation technique is commonly utilized:

$$R_{rm}(t, \Delta f) = \frac{\sum_{i=1}^{n}\left(I_r(t, f_i) - \overline{I_r}(t)\right)\left(I_m(t, f_i + \Delta f) - \overline{I_m}(t)\right)}{\sqrt{\left(\sum_{i=1}^{n}\left(I_r(t, f_i) - \overline{I_r}(t)\right)^2\right)\left(\sum_{i=1}^{n}\left(I_m(t, f_i + \Delta f) - \overline{I_m}(t)\right)^2\right)}} \tag{2-35}$$

where n is the frequency number in the scanning process, and:

$$\overline{I_x}(t) = \frac{1}{n}\sum_{i=1}^{n} I_x(t, f_i), \quad x = r, m \tag{2-36}$$

Based on Equation (2-35), the cross-correlation spectrum can be formulated as a function of both time (which corresponds to fiber distance) and optical frequency. This allows for the quantitative extraction of distributed temperature and strain information directly from the cross-correlation spectrum.

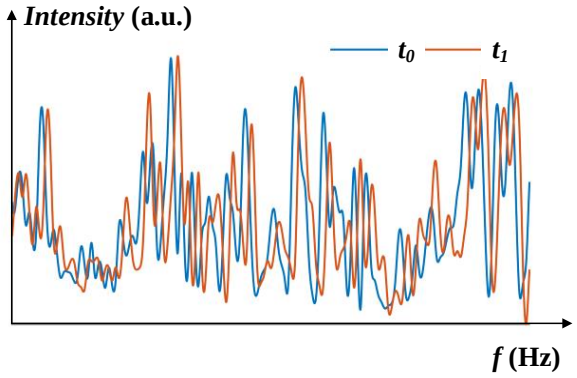

Figure 2-6: The frequency drift caused by the temperature/strain.

2.4.2 Key parameters of frequency scanning Φ-OTDR

For distributed optical fiber sensing systems, evaluating the sensing performance involves several key criteria:

Spatial resolution

Spatial resolution refers to the smallest distance over which a change can be detected by the sensor. In single pulse coherent OTDR, the SR is determined by the optical pulse width T_p. As shown in Fig. 2-7, at $t=t_0$, a fraction of the light pulse is reflected by the scatterers and then the scattering light propagates backward. Then the pulse continues to travel forward in fiber. When it comes to $t=t_0+t'$($t' < T_p/2$), another fraction of light is reflected. The reflected light at t_0 and t_0+t' will overlap with each other, making the

reflected light indistinguishable. At the time when $t=t_0+T_p/2$, the reflected light pulse will be temporally separated from the reflected light generated at t_0. Therefore, the spatial resolution of the system Δz is one-half the pulse's spatial width:

$$\Delta z = \frac{cT_p}{2n} \tag{2-37}$$

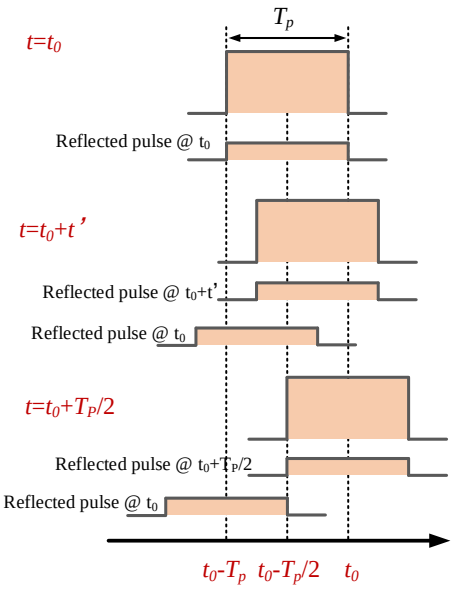

Figure 2-7: The propagation of the optical pulse and its backscattering signal.

Measurement range

The measurement range is the maximum distance over which measurements can be accurately taken. As the transmission distance extends, the energy of the pulse propagating through the fiber attenuates, leading to a point where the backscattered energy from the pulse at the distal end of the fiber becomes indistinguishable from noise. Consequently, the measurement range is fundamentally limited by the SNR.

The generation of noise within the system can be attributed to several sources. These include the wideband amplified spontaneous emission (ASE) noise introduced by optical amplifiers, optical pulse leakage due to suboptimal extinction ratios, and electrical noise such as thermal noise and shot noise emanating from the photodetector.

The signal power of the system is contingent upon the pulse energy and the reflectivity of the fiber. Given that the reflectivity of a specific optical fiber is constant, enhancements in signal power can be achieved either by extending the pulse width or by increasing the peak power of the pulse.

However, these approaches present a set of trade-offs. In the context of pulse-interrogated frequency scanning Φ-OTDR, an increase in pulse width adversely affects SR, establishing a compromise between achieving a broad measurement range and maintaining high SR. Moreover, there is a limit to how much the peak power of the incident pulse can be increased, constrained by the onset of nonlinear effects within the fiber. Modulation instability (MI) is typically the first nonlinear effect to manifest as the optical power crosses a certain threshold [96]. Beyond this threshold, broad sidelobes may emerge in the optical spectrum, diminishing the coherence of RBS light and leading to position-dependent signal fading in long-range sensing applications.

To extend the measurement range of Φ-OTDR systems, several strategies have been employed, including Raman amplification [15], Brillouin amplification [97], and hybrid amplification techniques [16]. These methods aim to compensate for the optical power attenuation during transmission, thereby enhancing the system's ability to accurately measure over longer distances.

Dynamic range

Dynamic range is defined as the maximum measurable physical quantity of a system. In spectrum-demodulated Φ-OTDR, a reference RBS spectrum taken before a perturbation and a live measurement RBS spectrum taken after the perturbation must be collected by adjusting the optical pulse frequency or launching the LFM signal into the sensing fiber. The measured quantities are then estimated by calculating the cross-

correlation between the measurement and reference spectra, and determining the lag of the maximum in the cross-correlation function.

As the frequency shift increases, the measurement spectrum pattern may move outside the window of the reference spectrum, reducing the effective spectrum area and potentially leading to failure in frequency shift estimation. The dynamic range of spectrum-demodulated Φ-OTDR is therefore limited by the frequency scanning range of the optical pulse or LFM signal.

Measurement time

The measurement time of frequency scanning Φ-OTDR T_m is determined by:

$$T_m = N\left(N_{ave}T_r + t_s\right) \tag{2-38}$$

where N is the number of the frequencies in the scanning process, N_{ave} is the average times of RBS traces, T_r is the pulse period which is the reciprocal of the repetition rate, and t_s is the frequency switching latency. To prevent overlap of RBS traces between adjacent pulses injected into the fiber, it is necessary to make the pulse period larger than the round-trip time of the pulse in fiber. T_r needs to satisfy:

$$T_r > \frac{2nL}{c} \tag{2-39}$$

where L is the length of the sensing fiber. A larger measurement fiber length L will result in a greater measurement time T_m, which gives rise to a mutually restrictive relationship between the measurement speed and the measurement range. In addition, for a given frequency scanning interval, the frequency scanning range is proportional to the frequency number N, which brings another trade-off between the dynamic range of the measured parameter and the measurement speed.

2.5 Φ-OTDR based on chirped pulse and pulse compression

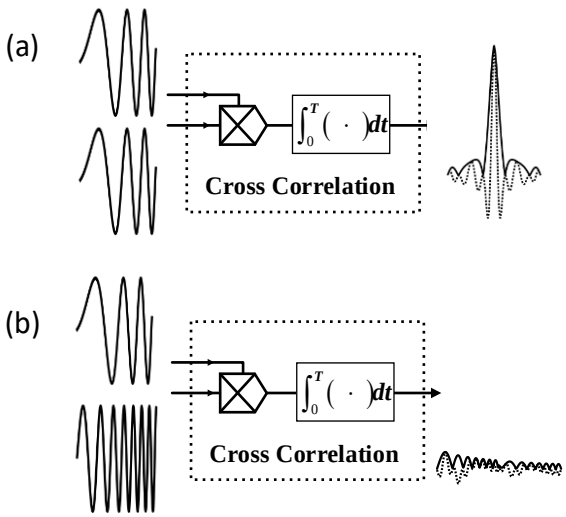

Figure 2-8: Principle of pulse compression. (a) match filtering; (b) non-match filtering [30].

The concept of pulse compression originated from the radar field. Fig. 2-8 illustrates the principle of pulse compression using linear frequency modulation. In Fig. 2-8 (a), when two LFM signals with the same frequency sweep range and sweep rate are cross-correlated, a correlation peak with sidelobe suppression is generated. However, if the two LFM signals differ in frequency sweep range and sweep rate, the cross-correlation result shows weak ripples, as depicted in Fig. 2-8 (b). In pulse compression Φ-OTDR, an LFM pulse is transmitted into the FUT, and the RBS signal is detected by a coherent receiver using a single-frequency continuous light as the LO. This section introduces the principle of pulse compression Φ-OTDR, followed by the coherent detection methods utilizing a 2x2 coupler and a 90 ℃ optical hybrid. Additionally, the spectrum demodulation technique based on the SPEA is explained.

Hypothesizing an electrical LFM signal with a starting frequency of f_m, a chirp rate of k, and a pulse duration of T is used to modulate the laser light source:

$$p(t)=\exp\left\{j2\pi f_m t+j\pi k t^2\right\}rect(t/T) \tag{2-40}$$

The continuous light with a carrier frequency of v_0 is modulated into:

$$p_o(t) = \exp\left\{ j2\pi(v_0 + f_m)t + j\pi kt^2 \right\} rect(t/T) \tag{2-41}$$

Then the optical pulse is launched into the FUT and the RBS signal can be written as:

$$E_{RS}(t) = \sum_{i=1}^{N_s} a_i \exp\left(-\alpha \frac{c\tau_i}{n} \right) p_o(t - \tau_i) \tag{2-42}$$

where a_i is the reflective amplitude of the i-th scatterer, τ_i is time delay of the i-th scatterer, N_s represents the number of scatterers, and α stands for the attenuation coefficient of fiber. c and n are the light velocity in vacuum and the RI of fiber, respectively. In coherent detection, the LO signal is the continuous light with the expression:

$$E_{LO}(t) = A_{LO} \exp\left\{ j2\pi v_0 t \right\} \tag{2-43}$$

The interference intensity between the LO and the RBS signal is proportional to the square of the composite optical field:

$$\begin{aligned} s_m(t) &\propto \left| E_{LO}(t) + E_{RS}(t) \right|^2 \\ &\left| E_{LO}(t) \right|^2 + \left| E_{RS}(t) \right|^2 + E_{RS}(t) E_{LO}^{*}(t) + E_{RS}^{*}(t) E_{LO}(t) \end{aligned} \tag{2-44}$$

In the above equation, the first two terms are direct currents representing light intensities of LO and RBS respectively, and do not contain sensing information. The last two terms are beat signals between the LO and RBS, which is the term of interest. It can be expressed as:

$$
\begin{aligned}
s_m(t) &= 2R_{PD}E_{RS}(t)E_{LO}^{*}(t) \\
&= 2R_{PD}A_{LO}\sum_{i=1}^{N_s} a_i \exp\left(-\alpha\frac{c\tau_i}{n}\right)\exp\{-j2\pi v_0\tau_i\} \\
&\quad \times \exp\left\{j2\pi f_m(t-\tau_i)+j\pi k(t-\tau_i)^2\right\} rect\left(\frac{t-\tau_i}{T}\right) \\
&= 2R_{PD}A_{LO}\cdot h_{FUT}(t) * p(t)
\end{aligned}
\tag{2-45}
$$

R_{PD} represents the responsivity of the photodetector, * represents convolution operation. And $h_{FUT}(t)$ is the impulse response of heterodyne detection of FUT, which is given by:

$$
h_{FUT}(t) = \sum_{i=1}^{N_s} \overline{a_i} \exp(-j2\pi v_0\tau_i)\delta(t-\tau_i) \tag{2-46}
$$

where $\overline{a_i} = a_i \exp(-\alpha c\tau_i/n)$.

Then a matched filter $p^*(-t)$ can be generated in the digital domain and convolved with the beat signal in Eq. (2-45):

$$
\begin{aligned}
s(t) &= s_m(t) * p^*(-t) \\
&= 2R_{PD}A_{LO}\cdot h_{FUT}(t) * p(t) * p^*(-t) \\
&= 2R_{PD}A_{LO}\cdot h_{FUT}(t) * R(t)
\end{aligned}
\tag{2-47}
$$

in which:

$$
\begin{aligned}
R(t) &= p(t) * p^*(-t) \\
&= rect\left(\frac{t}{2T}\right)\frac{\sin\left[\pi kt(T-|t|)\right]}{\pi kt}\exp\left\{-j2\pi\left(f_m+\frac{kT}{2}\right)t\right\}
\end{aligned}
\tag{2-48}
$$

$R(t)$ is the compressed pulse which can be regarded as the equivalent interrogating pulse of the system. Therefore, the SR of the system is no longer limited by the pulse width injected into the fiber, but by the full width at half maximum (FWHM) of $R(t)$ which is given by:

$$
\Delta z = \frac{c}{2nkT} = \frac{c}{2nB} \tag{2-49}
$$

where B is the bandwidth of the LFM signal. The larger the bandwidth, the higher

the spatial resolution. So, the SNR of the system can be enhanced by increasing the width of the LFM signal without sacrificing the spatial resolution.

2.5.1 Coherent detection methods

In pulse compression Φ-OTDR, the recovery of the complex optical field, as described in Eq. (2-45), necessitates the use of a coherent receiver. This receiver employs a strong LO to serve as the optical frequency reference. Subsequently, the received signal is convolved with a digital matched filter to achieve pulse compression. Coherent detection techniques, such as balanced coherent detection and I/Q detection, are instrumental in this process.

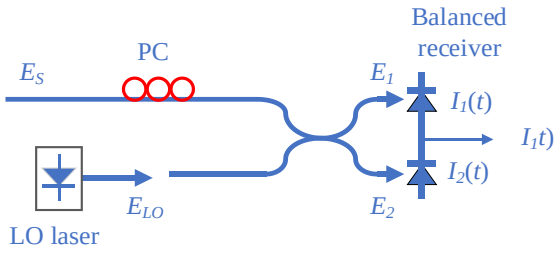

Figure 2-9: Sketch map of balanced coherent detection [98].

Balanced coherent detection is a technique employed to measure the beat frequency between the signal and the LO, as illustrated in Fig. 2-9. A polarization controller (PC) is used to align the polarization states between the signal and LO, and a balanced receiver is utilized to eliminate the direct current (DC) component. A 3 dB coupler is employed to mix the LO E_{LO} and the signal E_S ,and its transfer matrix is:

$$\begin{bmatrix} b_1 \\ b_2 \end{bmatrix} = \frac{1}{\sqrt{2}} \begin{bmatrix} 1 & j \\ j & 1 \end{bmatrix} \begin{bmatrix} a_1 \\ a_2 \end{bmatrix} \tag{2-50}$$

Therefore, the output signal of the two ports is:

$$\vec{E}_1(t) = \left[\vec{E}_S(t) + j\vec{E}_{LO}(t) \right] / \sqrt{2} \tag{2-51 a}$$

$$\vec{E}_2(t) = j\left[\vec{E}_S(t) - j\vec{E}_{LO}(t)\right]/\sqrt{2} \tag{2-51 b}$$

The photocurrents detected by the two photodiodes can be derived:

$$i_1(t) = \frac{1}{2}R_{PD}\left[\left|A_S(t)\right|^2 + \left|A_{LO}(t)\right|^2 + 2A_S(t)\cdot A_{LO}(t)\sin\left(\omega_{IF}t + \Delta\varphi\right)\right] \tag{2-52 a}$$

$$i_2(t) = \frac{1}{2}R_{PD}\left[\left|A_S(t)\right|^2 + \left|A_{LO}(t)\right|^2 - 2A_S(t)\cdot A_{LO}(t)\sin\left(\omega_{IF}t + \Delta\varphi\right)\right] \tag{2-52 b}$$

where $A_{LO}(t)$ and $A_S(t)$ are the amplitude of LO and signal, $\omega_{IF} = \omega_{LO} - \omega_S$ is the frequency difference between them, known as the intermediate frequency. $\Delta\varphi = \varphi_{LO} - \varphi_S$ represents the phase difference. In the balanced receiver, two head-to-toe connected photodiodes are used and the DC components in Eq. (2-52) can be canceled by subtracting $i_1(t)$ and $i_2(t)$:

$$\Delta i(t) = i_1(t) - i_2(t) = 2R_{PD}A_S(t)A_{LO}(t)\sin\left(\omega_{IF}t + \Delta\varphi\right) \tag{2-53}$$

When a balanced coherent detection is applied in the pulse compression Φ-OTDR, the photocurrent would be:

$$\begin{aligned}\Delta i(t) = 2R_{PD}A_{LO}\sum_{i=1}^{N_s} a_i \exp\left(-\alpha\frac{c\tau_i}{n}\right) \\ \times\sin\left[-2\pi v_0\tau_i + 2\pi f_m\left(t-\tau_i\right) + \pi k\left(t-\tau_i\right)^2\right] rect\left(\frac{t-\tau_i}{T}\right)\end{aligned} \tag{2-54}$$

Generally, the optical power of the LO is much greater than the RBS. This disparity in power levels is advantageous because the strong LO can effectively amplify the weak RBS signal through the process of coherent detection. As a result of this amplification, the SNR of the detected signal is enhanced The amplitude and phase of the detected signal can be demodulated with digital processing [26], [99].

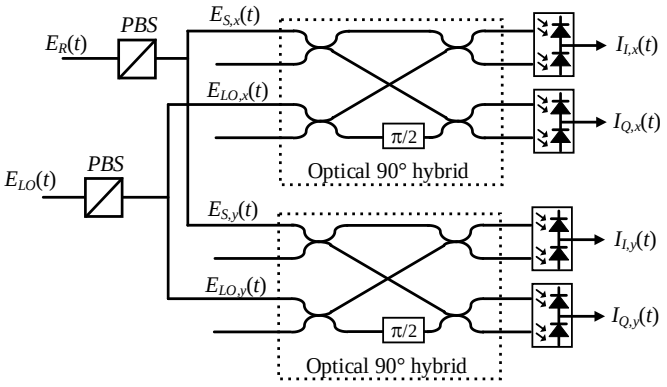

Figure 2-10: Block diagram of a 2×8 90-degree hybrid coupler [83], [100].

The I/Q detection method, which utilizes a 90° optical hybrid, is another approach for recovering the full optical field, as depicted in Fig. 2-10. This method incorporates phase diversity, polarization diversity, and balanced detection techniques to achieve comprehensive demodulation of the light field. By introducing an additional branch of the LO with a 90° phase shift and splitting the signal into two separate paths, in-phase (I) and quadrature (Q) components of the signal can be simultaneously obtained. Since the I/Q demodulation is achieved in the optical domain rather than in the electrical domain in this method, techniques such as positive and negative frequency multiplexing [101] can be effectively implemented using the optical hybrid. Meanwhile, two polarization beam splitters (PBS) are used to achieve polarization diversity and overcome the fading arising from the polarization mismatch between the LO and signal. Taking the *x* polarization state as the example, the output optical field of four ports of couplers are:

$$\vec{E}_1(t) = \left[\vec{E}_S(t) + j\vec{E}_{LO}(t)\right]/2 \tag{2-55 a}$$

$$\vec{E}_2(t) = j\left[\vec{E}_S(t) - j\vec{E}_{LO}(t)\right]/2 \tag{2-55 b}$$

$$\vec{E}_3(t) = \left[\vec{E}_S(t) - \vec{E}_{LO}(t)\right]/2 \tag{2-55 c}$$

$$\vec{E}_4(t) = j\left[\vec{E}_S(t) + \vec{E}_{LO}(t)\right]/2 \tag{2-55 d}$$

So that the photocurrent of the two balanced photodetectors can be expressed as:

$$\begin{aligned}\Delta i_Q(t) &= R_{PD}\left[\left|\overrightarrow{E_1}(t)\right|^2-\left|\overrightarrow{E_2}(t)\right|^2\right] \\ &= R_{PD}A_S(t)A_{LO}(t)\sin(\omega_{IF}t+\Delta\varphi)\end{aligned} \tag{2-56 a}$$

$$\begin{aligned}\Delta i_I(t) &= R_{PD}\left[\left|\overrightarrow{E_4}(t)\right|^2-\left|\overrightarrow{E_3}(t)\right|^2\right] \\ &= R_{PD}A_S(t)A_{LO}(t)\cos(\omega_{IF}t+\Delta\varphi)\end{aligned} \tag{2-56 b}$$

The complex optical field can be constructed as:

$$E=\Delta i_I(t)+j\Delta i_Q(t) \tag{2-57}$$

In pulse compression Φ-OTDR, the optical field of Eq. (2-45) detected by the I/Q detector is:

$$\begin{aligned}\Delta i_Q(t) &= R_{PD}A_{LO}\sum_{i=1}^{N_s}a_i\exp\left(-\alpha\frac{c\tau_i}{n}\right) \\ &\times\sin\left[-2\pi v_0\tau_i+2\pi f_m(t-\tau_i)+\pi k(t-\tau_i)^2\right]rect\left(\frac{t-\tau_i}{T}\right)\end{aligned} \tag{2-58 a}$$

$$\begin{aligned}\Delta i_I(t) &= R_{PD}A_{LO}\sum_{i=1}^{N_s}a_i\exp\left(-\alpha\frac{c\tau_i}{n}\right) \\ &\times\cos\left[-2\pi v_0\tau_i+2\pi f_m(t-\tau_i)+\pi k(t-\tau_i)^2\right]rect\left(\frac{t-\tau_i}{T}\right)\end{aligned} \tag{2-58 b}$$

2.5.2 Spectrum demodulation based on SPEA

Eq. (2-45) indicates that the Rayleigh scattering signal is the convolution of the impulse response of fiber $h_{FUT}(t)$ and the chirped pulse function $p(t)$. Although phase demodulation can be employed after pulse compression to obtain the information of measurands [102], [103], the primary focus of this work is on the RBS spectrum pattern demodulation. In this section, the signal demodulation from the frequency domain is analyzed.

Taking Fourier transform to the fiber impulse response of heterodyne detection

$h_{FUT}(t)$ in Eq. (2-46):

$$\begin{aligned} h_{FUT}(\omega) &= \int_{-\infty}^{+\infty} h_{FUT}(t) e^{-j\omega t} dt \\ &= \sum_{i=1}^{N_s} \overline{a_i} \exp\{-j2\pi v_0 \tau_i\} \int_{-\infty}^{+\infty} \delta(t-\tau_i) e^{-j\omega t} dt \end{aligned} \tag{2-59}$$

The Dirac function δ has the property of:

$$\int_{-\infty}^{+\infty} f(x)\delta(x-x_0)dx = f(x_0) \tag{2-60}$$

and Eq. (2-59) can be expressed as:

$$h_{FUT}(\omega) = \sum_{i=1}^{N_s} \overline{a_i} \exp\{-j(\omega_0+\omega)\tau_i\} \tag{2-61}$$

where $\omega_0 = 2\pi v_0$. In Eq. (2-61), $\overline{a_i}$ is the amplitude of the i-th scatterer considering the fiber attenuation, which is a random variable. Therefore, the impulse response of fiber in the frequency domain also fluctuates randomly. A chirped pulse can act as a filter for the fiber's impulse response in the frequency domain, with the filtered signal varying in accordance with the frequency range of the chirped pulse.

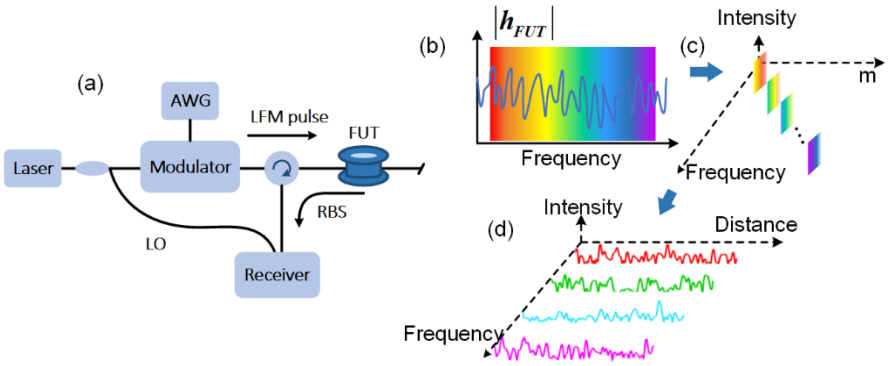

Figure 2-11: Principle of Φ-OTDR based on pulse compression and spectrum demodulation. (a) system configuration; (b-d) principle of SPEA [46].

Fig. 2-11 depicts the configuration of pulse compressed Φ-OTDR and illustrates how the SPEA is utilized to enable single-shot measurements. A LFM signal with a wide bandwidth is injected into the FUT to capture the RBS signal. In Fig. 2-11 (b), the

acquired signal encompasses a wide span of the fiber impulse response in the frequency domain due to the large bandwidth of the probing LFM signal. Referring back to Eq. (2-45), the RBS signal in the frequency domain can be expressed as:

$$s_m(\omega) = 2R_{PD}A_L h_{FUT}(\omega)\, p(\omega) \tag{2-62}$$

If a chirped pulse $p'(t)$ with a much smaller frequency range than $p(t)$ is used to compress the detected RBS signal in digital domain, the obtained compressed signal is:

$$s'_m(\omega) = 2R_{PD}A_L h_{FUT}(\omega)\, p'(\omega) = s_m(\omega)h(\omega) \tag{2-63}$$

where $h(\omega) = p'(\omega)/p(\omega)$. In the digital domain, we generate sub-chirped pulses $p_m(t)(m = 1, 2, ..., N)$ with equidistant frequency spacing and a much smaller frequency range than $p(t)$ (as shown in Fig. 2-11 (c)). Using matched sub-chirped filters $p_m^*(-t)$ to filter the Rayleigh scattering signal, we can get:

$$s_{mfm}(\omega) = \frac{|p_m(\omega)|^2}{p(\omega)} s_m(\omega) \tag{2-64}$$

To simplify the expression, construct the transfer matrix $H(\omega)$:

$$H(\omega) = \left[\frac{|p_1(\omega)|^2}{p(\omega)} \quad \frac{|p_2(\omega)|^2}{p(\omega)} \quad \cdots \quad \frac{|p_N(\omega)|^2}{p(\omega)} \right] \tag{2-65}$$

The RBS matrix is given by:

$$s_{mf} = s(\omega) I_{1\times N} \circ H(\omega) \tag{2-66}$$

where $A \circ B$ represents the Hadamard product. $I_{1\times N}$ is a matrix with 1 row and N columns and all elements 1. Then the RBS spectrum can be acquired through IFT and taking the absolute value. With the SPEA algorithm, the time-consuming frequency scanning process to construct the Rayleigh spectrum is not needed and single-shot measurement can be achieved. Since sub-chirped pulses are used here, the SR is eventually determined by the bandwidth of the sub-chirped pulse.

2.6 Optical frequency domain reflectometry

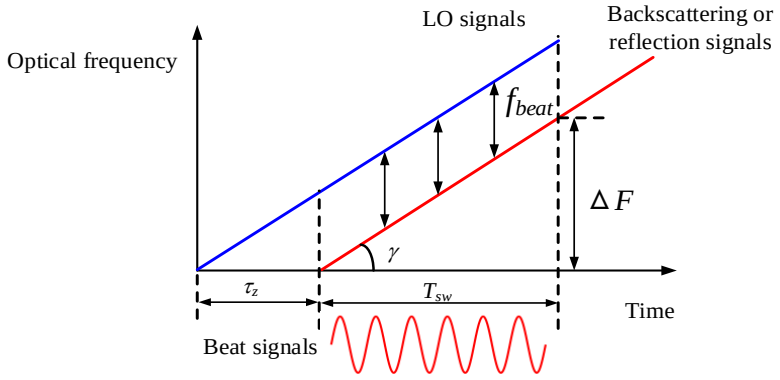

Figure 2-12: Schematic diagram of OFDR principle [57].

The time-frequency relationship of OFDR is shown in Fig. 2-12. A LFM signal with a slope of γ is used as the LO light and the probe light simultaneously. As the probe light travels in the sensing fiber and is reflected by the scatterers at position z, a time delay τ_z related to z is generated between the LO and RBS signal:

$$\tau_z = 2Zn/c \tag{2-67}$$

where n and c are the RI of fiber and the vacuum velocity of light, respectively. The beat frequency f_{beat} can be written as:

$$f_{beat} = \tau_z \gamma = 2Zn\gamma/c \tag{2-68}$$

From Eq. (2-68), the magnitude of beat frequency is proportional to the position of scatterers. Therefore, the spatial domain signal can be obtained by applying FFT to the time domain signal.

The LO can be expressed as:

$$E_r(t) = E_0(t)\exp\left\{j\left[2\pi f_0 t + \pi\gamma t^2 + \phi(t)\right]\right\} \tag{2-69}$$

$\phi(t)$ is the random phase of the laser source. Supposing the fiber attenuation coefficient is α, the reflectivity of fiber is:

$$R(\tau_z) = r(\tau_z)\exp(-\alpha\tau_z c/n) \tag{2-70}$$

The RBS light with a time delay τ_z can be written as:

$$\begin{aligned} E_s(t) &= \sqrt{R(\tau_z)}E_r(t-\tau_z) \\ &= \sqrt{R(\tau_z)}E_0 \exp\left\{ j\left[2\pi f_0(t-\tau_z) + \pi\gamma(t-\tau_z)^2 + \phi(t-\tau_z) \right] \right\} \end{aligned} \tag{2-71}$$

The beat signal between the LO and the RBS can be written as:

$$\begin{aligned} I_{beat}(t) &\propto 2E_r(t)\cdot E_s^*(t) \\ &= 2\sqrt{R(\tau_z)}E_0^2 \cos\left[2\pi\left(f_0\tau_z + f_{beat}t + \frac{1}{2}\gamma{\tau_z}^2 + \phi(t) - \phi(t-\tau_z) \right) \right] \end{aligned} \tag{2-72}$$

In the above equation, $f_{beat}t$ represents the beat frequency, and $\phi(t)-\phi(t-\tau_z)$ is the phase noise. The PSF refers to the power spectral density (PSD) of the beat signal I_{beat} [47]:

$$P(f, f_{beat}) = 2RE_0^4\delta(f - f_{beat}) \tag{2-73}$$

The FWHM of the PSF determines the SR of the OFDR system. Theoretically, the optimal SR Δz and the sensing range L of OFDR are:

$$\begin{cases} \Delta z = \dfrac{c}{2n\Delta F} \\ L \propto \dfrac{c}{2n\Delta\upsilon} \end{cases} \tag{2-74}$$

where ΔF and $\Delta\upsilon$ are the frequency sweeping range and the laser linewidth. In an OFDR using a tunable laser source, the phase noise term in Eq. (2-72) is non-negligible, which is the primary factor leading to the degeneration of PSF and the system's performance. The phase noise contains two parts: the frequency tuning nonlinearity and the stochastic laser phase noise. The frequency tuning nonlinearity of the laser source results in the broadening of the PSF, deteriorating the SR of the system. Additionally, the stochastic laser phase noise reduces the light source's coherence, which not only degrades the spatial resolution but also exponentially decreases the amplitude of the PSF. One effective approach to overcome the frequency tuning nonlinearity and the

phase noise is using an NLL and an EOM to generate the LFM signal [74]. The configuration is shown in Fig. 2-13.

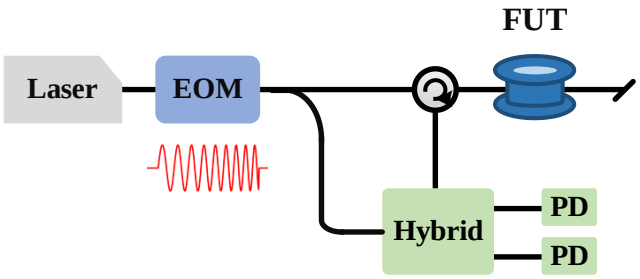

Figure 2-13: Basic setup of OFDR using an NLL source and an EOM.

The spectrum demodulation process is shown in Fig. 1-7 in section 1.2.2.3. After converting the signal to the spatial domain through FFT, a sliding window is applied to the spatial domain signal and IFFT is employed to convert the local RBS signal to the optical spectrum domain. The length of the sliding window is a crucial parameter that would finally determine the SR. The following equation is satisfied between SR Δx and the number of points in the window N:

$$\Delta x = N\Delta z \tag{2-75}$$

where Δz is the optimal SR defined in Eq. (2-74). To ensure a high SR, N should be small. However, it also results in a reduction of points in the frequency spectrum after IFFT, deteriorating the frequency resolution and the strain resolution.

To quantify the strain resolution, we collected 800 RBS traces of an unperturbed fiber with the OFDR and computed the frequency shifts of the Rayleigh spectra using cross-correlation. The frequency range of the LFM signal and the system's sampling rate were 3.5 GHz and 1.25 kHz, respectively. The PSD of the frequency shift results with different sliding window widths are shown in Fig. 2-14.

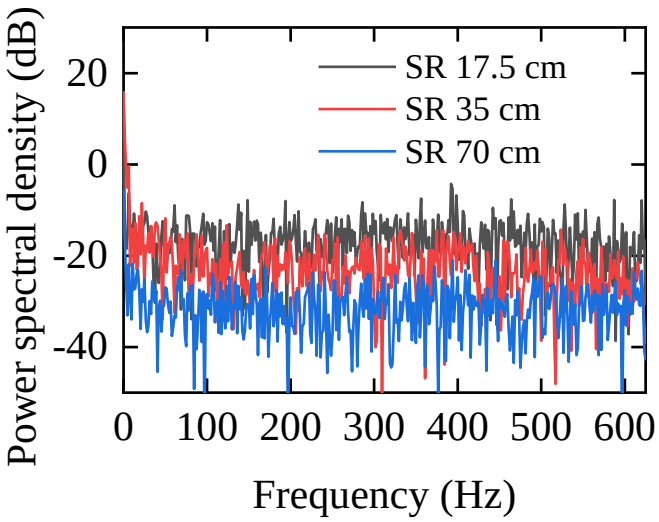

Figure 2-14: The PSD in case of different spatial resolutions.

From Fig. 2-14, the higher the spatial resolution, the noise level in the PSD also gets higher. The noise levels for spatial resolutions 17.5 cm, 35 cm, and 70 cm are -13.3 dB, -22.7 dB, and -27.5 dB, respectively, corresponding to 0.0014 $\mu\varepsilon/\sqrt{Hz}$, 488 $p\varepsilon/\sqrt{Hz}$, and 281 $p\varepsilon/\sqrt{Hz}$ strain resolutions.

We calculated the PSD along the fiber distance and analyzed the noise level in the PSD. The PDFs of the noise level at different fiber locations are shown in Fig. 2-15 (a). As the spatial resolution gets larger, the PDF becomes narrower, indicating a more stable measurement of strain. Then the cumulative distribution functions (CDF) are also computed. The 99% of the CDF is used to characterize the strain resolution of the system, which are 536 $p\varepsilon/\sqrt{Hz}$, 1323 $p\varepsilon/\sqrt{Hz}$, and 0.03 $\mu\varepsilon/\sqrt{Hz}$ for 70 cm, 35 cm, and 17.5 cm SR, respectively. When determining the number of data points N in the sliding window, it is important to strike a balance between the spatial resolution and sensing accuracy requirements in practical applications.

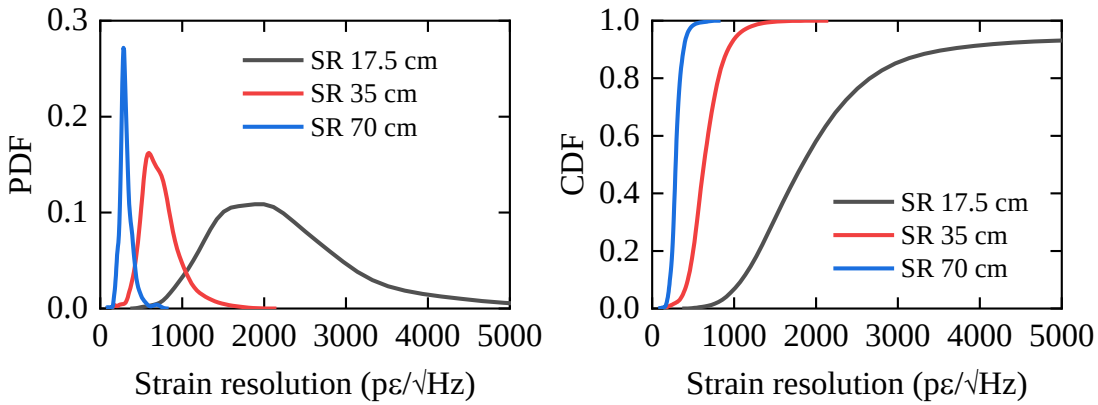

Figure 2-15: (a) The PDF of the strain resolutions; (b) The corresponding CDF.

2.7 Summary

In this chapter, we first introduce the mechanism of Rayleigh scattering. We then discuss the statistical characteristics of Rayleigh scattering in optical fibers, along with the temperature and strain sensitivity of the Rayleigh spectrum. Additionally, we elaborate on the theories of DOFS based on frequency scanning Φ-OTDR, pulse compression Φ-OTDR, and OFDR. The theoretical foundation laid out in this chapter serves as the basis for the experimental investigations detailed in the following chapters.

3 Distributed Salinity Sensing Based on Frequency-Scanning Φ-OTDR

3.1 Introduction

Salinity holds significant importance in various fields such as oceanography, climate studies, and ocean resource management [104], [105], [106]. For instance, in ocean resource development, salinity measurements offer valuable insights into salinity gradients and the adaptability of marine organisms, aiding in activities like aquaculture, fishing, and marine energy development. In climate research, precise measurement of salinity in the ocean helps to track changes in surface and deep-water circulation, thus revealing the ocean's impact and feedback mechanisms on climate change. These applications underscore the need for high-performance salinity sensors.

Commercially available salinity sensors typically fall into two categories: electrical and optical sensors. Electrical sensors often measure the conductivity of solutions to determine salinity [107], while optical methods typically utilize prismatic structures to measure the RI of the solution indirectly for salinity determination [108], [109]. While these sensors have made significant advancements in sensitivity and accuracy over the years, a limitation is that they are unable to facilitate remote salinity measurements.

In recent years, OFS has garnered attention for environmental monitoring due to their corrosion resistance, safety, immunity to electromagnetic interference, and remote sensing capabilities. Several types of optical fiber sensors have been developed for salinity measurements, including fiber Bragg grating (FBG) [110], [111], [112], Fabry-Perot (F-P) cavity [113], [114], surface plasmon resonance (SPR) [115], [116], [117],

and special fiber structures [118], [119], [120], [121]. The principles of measuring salinity using these sensors can be categorized into two types. One approach involves obtaining salinity information by measuring the RI of the sample. For example, the F-P cavity [113] and the special fiber structures based on no-core fiber [118] have achieved high-sensitivity salinity sensing through RI measurements. In these methods, changes in salinity lead to variations in RI, altering the optical path of light passing through the samples, which in turn induces wavelength shifts in the interferometric spectrum of the sensors. Such sensors generally require intricate structural designs and complex fabrication procedures. Another type of sensor does not measure RI but instead utilizes hygroscopic materials such as polyimide or hydrogel. By interacting with the surrounding medium, these hygroscopic materials convert salinity into strain on the optical fiber, enabling salinity measurements. For instance, L. Men et al. proposed a multiplexed FBG sensor with polyimide and acrylate coating for simultaneous salinity and temperature measurement, achieving a salinity sensitivity of 0.0165 nm/(mol/L) and a temperature sensitivity of 0.0094 nm/°C [111]. In 2015, X. Zhang et al. introduced a salinity sensor based on an F-P cavity with a solid polyimide diaphragm and a spliced face, which attained a higher sensitivity of 0.45 nm/(mol/L) [114]. While these sensors exhibit high sensitivity and functionalities such as temperature and salinity discrimination, a common limitation is that salinity can only be measured at discrete points, and the salinity distribution profile along the optical fiber cannot be obtained.

DOFS offers the capability to spatially resolve and interrogate measurands along an unmodified optical fiber, thereby replacing tens of thousands of single-point sensors. DOFS based on BDG has emerged as a solution for continuous salinity measurements. In a study referenced as [75], salinity is measured by mapping the birefringence through BDG, while temperature compensation is achieved by monitoring the Brillouin

frequency shift of the fiber. With the support of a highly sensitive PCF, this approach demonstrated a salinity sensitivity of 139.6 MHz/(mol/L) and a salinity accuracy of 0.072 mol/L, coupled with an SR of 15 cm. Despite these achievements, the Brillouin scattering sensing mechanism presents challenges in further enhancing the sensitivity of the system, thereby limiting its application in high-sensitivity salinity measurement.

In this chapter, we propose and investigate high-sensitivity salinity sensors based on frequency-scanning Φ-OTDR and polyimide-coated fibers. The polyimide material used for fiber coating exhibits hygroscopic properties, causing the coating to swell or shrink with changes in external salinity. This, in turn, induces strain variations in the sensing fiber. We conducted a validation experiment on a polyimide-coated SMF to measure salinity. With a coating radius of 15 μm and a fiber length of 1100 m, we achieved a salinity sensitivity of 782.4 MHz/(mol/L). The response time of the polyimide-coated fiber to salinity changes was measured to be 8 minutes. We also analyzed the measurement accuracies of the system for different pulse widths, revealing an inverse relationship between measurement accuracy and pulse width. Furthermore, we proposed a method for discriminating between salinity and temperature using frequency-scanning Φ-OTDR and a polyimide-coated PMF. The anisotropic structure of the PMF allowed for different sensitivities to temperature and salinity on its slow and fast axes, enabling the decoupling of these parameters using a single fiber. In our experiments, the frequency-scanning Φ-OTDR probed the two polarization axes of the polyimide-coated PMF with orthogonal pulse sequences to obtain the temperature and salinity sensitive coefficients for each axis. The system demonstrated temperature sensitivities of -1407.8 MHz/K and -1348.9 MHz/K on the slow and fast polarization axes, respectively. Additionally, it exhibited salinity sensitivities of 1028 MHz/(mol/L) and 1008.6 MHz/(mol/L) on the slow and fast polarization axes, respectively.

Simultaneous measurement of temperature and salinity was successfully performed, with systematic measurement uncertainties of 0.0344 K and 0.0469 mol/L, respectively. These results demonstrate the sensor's excellent discrimination ability for temperature and salinity measurements.

3.2 Salinity-induced strain on polyimide-coated fiber

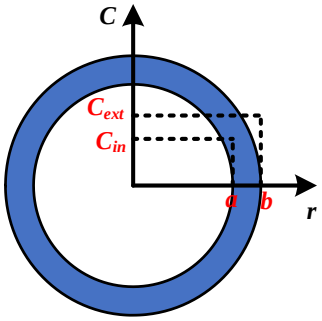

Figure 3-1: Water concentration distribution of the fiber cross-section [122].

To achieve distributed salinity measurement, it is necessary to utilize special fibers, as the commonly used standard SMF are less sensitive to salinity changes. One effective approach for salinity measurement is to coat silica fibers with hygroscopic materials. When a concentration gradient exists between the hygroscopic coating and the surrounding solution, water molecules will diffuse between the two mediums. The diffusion process can be described using Fick's second law [111], [122]:

$$\frac{\partial c}{\partial t} = D\nabla^2 c \tag{3-1}$$

where c represents the water concentration, t and D are the diffusion time and diffusion coefficient, respectively.

As can be seen in Fig. 3-1, the fiber coating can be modeled as a cylinder. Eq. (3.1) can be expressed in cylindrical coordinate:

$$\frac{\partial c}{\partial t} = D\frac{1}{r}\frac{\partial}{\partial r}\left(r\frac{\partial c}{\partial r}\right) \tag{3-2}$$

At time t, the radical diffusion at position *r* in the cylinder has the boundary condition:

$$c\left(a < r < b, t = 0\right) = C_{in} \tag{3-3 a}$$

$$c(r = b, t \geq 0) = C_{ext} \tag{3-3 b}$$

$$\frac{\partial c}{\partial r}(r = a, t \geq 0) = 0. \tag{3-3 c}$$

where C_{in} and C_{ext} are water concentrations at the inner and outer coating boundaries.

In this study, we opted for a polyimide coating due to the material's advantageous properties, such as its excellent linear response, high repeatability, and stable chemical attributes. When exposed to a test solution with relatively high salinity, water molecules will permeate unidirectionally from the coating into the solution. This osmotic process results in the dehydration and consequent shrinkage of the polyimide coating. In contrast, when the salinity of the test solution is comparatively low, the coating will absorb water molecules from the solution, leading to its expansion. Eventually, an equilibrium state is achieved between the coating and the solution. The solution to Eq. (3-2), which describes this equilibrium, is as follows:

$$c\left(r,t\right) = C_{ext}\ \text{erf}\, c\left(\frac{r}{\sqrt{4Dt}}\right) \tag{3-4}$$

As the polyimide coating swells or shrinks by absorbing or releasing water, the salinity of the solution can be converted into a mechanical response on the fiber in the form of strain, which is the basis of salinity measurement.

3.3 Distributed salinity sensor based on frequency-scanning Φ-OTDR and polyimide-coated single-mode fiber

3.3.1 System configuration

To validate the feasibility of measuring salinity using polyimide-coated fiber, we constructed a frequency-scanning Φ-OTDR setup and conducted experiments. The configuration is depicted in Fig. 3-2.

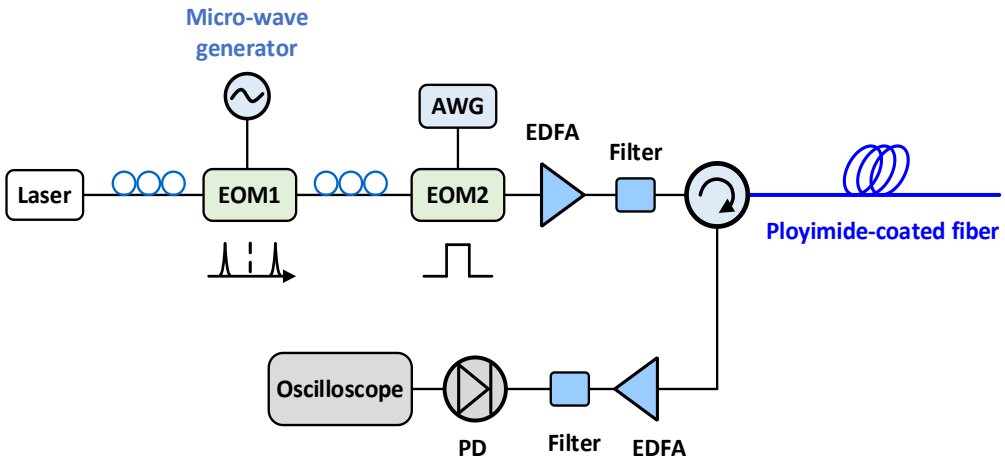

Figure 3-2: System configuration of frequency-scanning Φ-OTDR. EOM: electro-optic modulator; AWG: arbitrary waveform generator; EDFA: erbium-doped fiber amplifier; PD: photodetector.

As shown in Fig. 3-2, we utilize a laser featuring a narrow linewidth of 100 Hz, operating at a wavelength of 1550 nm, as the light source for our setup. The continuous wave emitted by the laser undergoes a frequency shift facilitated by the first EOM, which operates in a double-side-band modulation mode. This frequency shift is meticulously scanned by adjusting the output frequency of the microwave generator in increments of 20 MHz, ranging from 8.01 GHz to 11.99 GHz, thereby generating a total of 200 distinct frequencies. Subsequently, the frequency-shifted light is segmented into pulses by another EOM with a high extinction ratio (>40dB), referred to as EOM2, which is modulated by the electrical pulse signal output from the AWG. To optimize

the extinction ratio, two PCs are strategically placed at the input of each EOM. The peak power of the probe pulses is significantly amplified to 23 dBm using an erbium-doped fiber amplifier (EDFA), followed by a band-pass filter that eliminates unwanted sidebands and ASE noise. These prepared probe pulses are then introduced into the FUT, which spans a length of 1100 m, via a circulator. The Rayleigh backscattering light emanating from the FUT undergoes pre-amplification by a second EDFA (EDFA2), with its ASE noise further mitigated by another band-pass filter. A photodetector with a 200 MHz bandwidth converts the optical signals into electrical voltage, which is subsequently digitized by a high-speed oscilloscope (Osc) capable of sampling at a rate of 2 GSa/s.

In this experiment, the FUT is a commercially sourced polyimide-coated SMF, with a coating thickness of 15 μm (YOFC HT9/125-14/155(300)). The fiber is suspended in air within a relatively stable environment. At the distal end, a fiber segment approximately 6 m in length is submerged in a water bath maintained at room temperature. To create solutions of varying salinity, NaCl solution is added to pure water. For comparative purposes, the salinity levels of these solutions are concurrently measured using a commercially available salinometer, which boasts a nominal measurement accuracy of 0.0034 mol/L.

3.3.2 Measurement results of salinity sensitivity

Initially, the system's response to salinity was examined using a pulse width of 10 ns, which corresponds to an SR of 1 m. To determine the frequency shift associated with a specific salinity level, we conducted two sets of 3-D Rayleigh scattering spectrum measurements. In these experiments, the fiber was submerged in pure water and then in a NaCl solution of a given salinity. A 10-minute interval was allowed between the

two measurements to ensure the fiber coating adequately responded to the external change in salinity. To enhance the SNR, the traces were averaged 128 times, resulting in each measurement taking approximately 120 seconds. Fig. 3-3 displays the detected frequency spectra and their cross-correlation results for a salinity level of 1.33 mol/L. Fig. 3-3 (a) illustrates the frequency spectra before and after the salinity change at the location of 1079 m, where the fiber was exposed to air. It is evident that the two frequency spectra are similar in shape and exhibit no frequency shift, with their cross-correlation curve depicted in blue in Fig. 3-3 (c). Fig. 3-3 (b) presents the frequency spectra before and after the salinity change at the location of 1129 m, where the fiber was immersed in a water bath. Although the shapes of these two spectra are similar, a frequency shift is observed between them. The cross-correlation of these two spectra is represented by the red line in Fig. 3-3 (c). To accurately determine the frequency shift value, the peaks of the cross-correlation curves were subjected to quadratic polynomial fitting, as indicated by the black line in Fig. 3-3 (c). The abscissa value at the peak of the fitting curve provides the required frequency shift value. The two frequency shift values identified in Fig. 3-3 (c) are 0.015 GHz and 0.893 GHz, respectively.

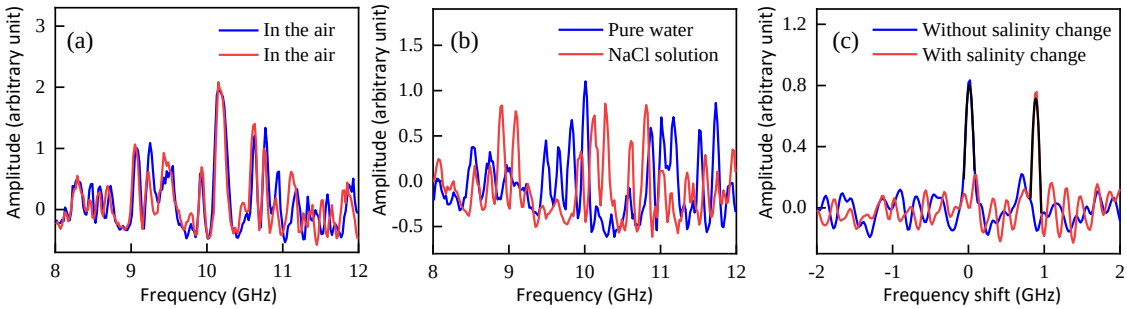

Figure 3-3: The detected frequency spectra before and after salinity change at different fiber locations at the concentration of 1.33 mol/L and their cross-correlation curves. (a) The frequency spectra before and after salinity change at the location 1079 m; (b) The frequency spectra before and after salinity change at the location 1129 m; (c) The cross-correlation curves of traces in Fig.3-3 (a) (blue) and (b) (red).

The cross-correlation spectrum was obtained by performing cross-correlation along the fiber distance, as depicted in Fig. 3-4 (a). From Fig. 3-4 (a), it is evident that the frequency shift approaches zero when the environmental conditions are stable. Fig. 3-4 (b) presents a magnified view of the spectrum, as indicated by the red dashed box in Fig. 3-4 (a). A discernible frequency shift spanning a length of 6 m is observed, which aligns well with the actual conditions encountered. To quantitatively assess the extent of the frequency shift, an average is computed over the segment between 1126.8 m and 1132.8 m, yielding an average frequency shift of 0.88 GHz at a salinity concentration of 1.33 mol/L.

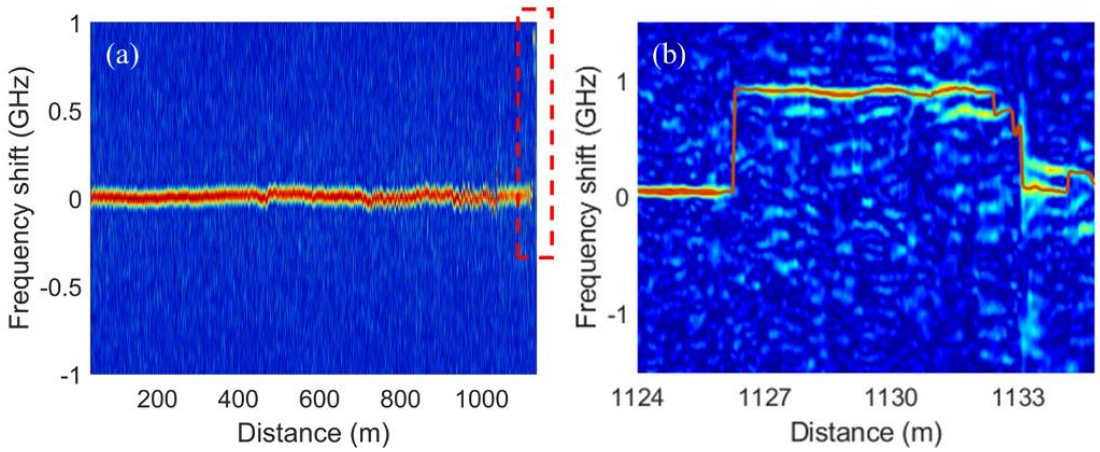

Figure 3-4: (a) The cross-correlation spectrum of 3-D Rayleigh backscattering spectra in the case of pure water and 1.33 mol/L salinity solution. (b) The enlarged cross-correlation spectrum at the location near the fiber end.

The frequency shift measurement results for different salinities are shown in Fig. 3-5 (a). The salinity ranges from 0 mol/L to 1.61 mol/L. We can see that as the salinity increases, the frequency shift increases accordingly. The average frequency shift in Fig. 3-5 (a) is plotted as a function of salinity, as shown in Fig. 3-5 (b). The frequency shift has a linear relationship with salinity. The fitting curve of the experimental results has a slope of 782.4 MHz/(mol/L), suggesting a high salinity sensitivity of the system. It is

worth noting that the dynamic range of the system is not restricted to 1.61 mol/L, since it can be easily increased by enlarging the frequency sweep range of probe pulses.

As can be seen from Fig. 3-5 (a), the frequency shift fluctuates over the distance between 1126.8 m and 1132.8 m, especially in the case of salinity of 0.41 mol/L and 1.61 mol/L. The uniformity of the frequency shift can be affected by different reasons such as the uniformity of NaCl solution, the contact between the fiber and solution, and the environmental perturbations. Since each salinity was measured independently, these experimental conditions might be slightly different in different measurements. The dip at 1131.5 m at the salinity of 0.41 mol/L might result from the insufficient contact between the fiber and the solution, and the fluctuation in the case of 1.61 mol/L salinity might be a comprehensive result of the nonuniformity of NaCl solution and the environmental perturbations.

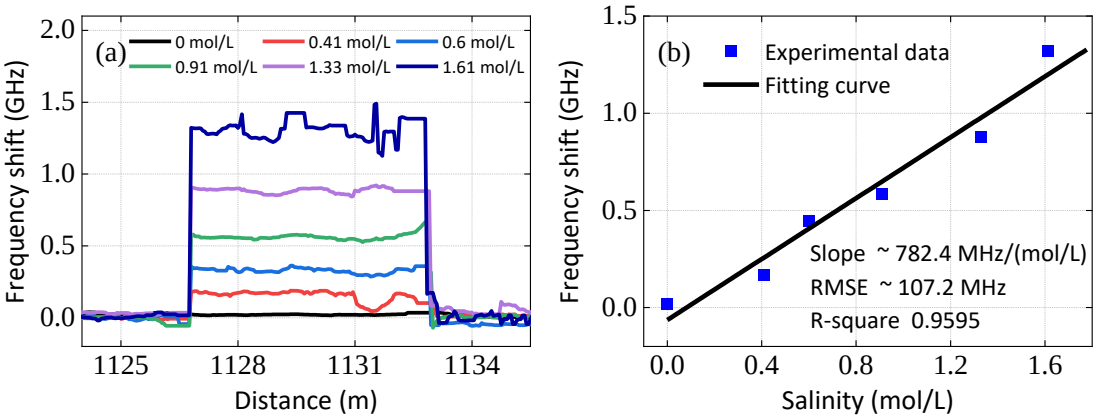

Figure 3-5: (a) The measured frequency shift of different salinities; (b) the frequency shift variation with salinity.

3.3.3 Measurement results of response time

Then we tested the response time of the fiber to salinity change. In this experiment, the frequency shift of optical pulses was swept from 9.765 GHz to 14.235 GHz at a step of 30 MHz, thus generating 150 frequencies in total. To make each measurement faster,

the average time of traces was set to 64, and the time taken for each Rayleigh backscattering spectrum measurement was 44.2 seconds. The response times of salinity 0.48 mol/L and 1.76 mol/L were measured with 3 ns pulse width respectively. For each salinity, we collected 18 Rayleigh spectra consecutively starting from the NaCl solution added into pure water, which took 13.3 minutes in total. Then the cross-correlation was performed to the adjacent spectra and 17 frequency shift curves were obtained. The results for different salinities are shown in Fig. 3-6. As time goes by, the magnitude of the frequency shift decreases, and the fiber reaches a stable state gradually. The frequency shift almost reaches zero at the time of 8 min.

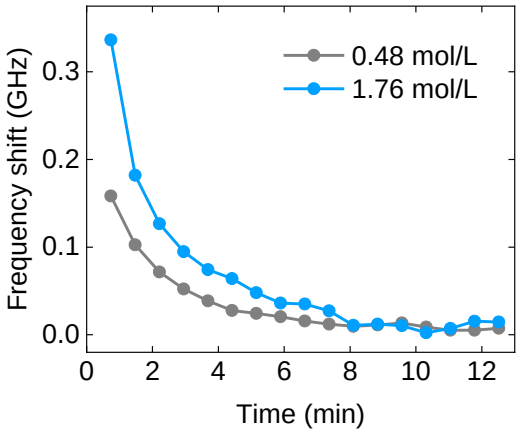

Figure 3-6: The response time of the fiber to salinity change

3.3.4 Analysis and evaluation of measurement accuracy

For each salinity, the 3-D Rayleigh scattering spectra were measured once in pure water and once in saline solution, and the cross-correlation of the two spectra provided the measured frequency shift results. The frequency shift measurement uncertainties σ can be characterized by the root mean square error between the true frequency shift Δf and the estimated frequency shift Δf , which is formulated as [123]:

$$\sigma = \sqrt{\frac{1}{I}\sum_{m=1}^{I}\left(\Delta f - \Delta f\right)^2} \tag{3-5}$$

where I is the total measurement times. In radar and sonar systems, the time delay estimation problem has been widely studied [124], [125], [126], [127], and the lower limit of mean-square error for time delay estimation is provided by the CRLB which indicates the optimal performance when utilizing a minimum variance unbiased estimator. The frequency shift estimation here is mathematically equivalent to the 'time delay estimation' in the radar system. The systematic noise is modeled as zero-mean additive white Gaussian noise to the true Rayleigh spectrum. The frequency shift estimation uncertainty is determined by:

$$\sigma = \frac{1}{\beta\sqrt{M_e}} = \frac{1}{\beta M_o} \tag{3-6}$$

where M_e and M_o represent the SNR of electrical power and optical power, respectively. β is given by:

$$\beta^2 = 4\pi^2 \frac{\int f^2 \left|U(f)\right|^2 df}{\int \left|U(f)\right|^2 df} \tag{3-7}$$

in which f and $U(f)$ are the optical frequency and the Fourier transform of the Rayleigh spectrum, respectively. For a frequency scanning Φ-OTDR interrogated with a rectangular pulse, the expected power density is in a triangular shape, and β with a triangular shape power density takes the following analytical form:

$$\beta = \frac{2\pi\tau}{\sqrt{6}} \tag{3-8}$$

where τ is the rectangular pulse width. Finally, the theoretical frequency shift estimation uncertainty can be written as:

$$\sigma = \frac{\sqrt{6}}{2\pi\tau M_o} \tag{3-9}$$

According to Eq. 3-9, the pulse width and the optical SNR of the signal are the two factors that affect the measurement accuracy. Then we experimentally investigated the measurement accuracy of frequency shift and compared it with the theoretical value. To investigate the measurement accuracy of frequency shift in the case of different pulse widths, a group of measurements was carried out. The pulse widths in this group of measurements were set to be 20 ns, 10 ns, 5 ns, and 3 ns respectively, the salinities were 1.33 mol/L in four experiments, and other parameters were the same as those in section 3.3.1.

Fig. 3-7 demonstrates the power density of the RBS spectra in case of different pulse widths. The horizontal axes are normalized frequencies, and the amplitudes of power density are normalized to the max. The envelopes are triangular shapes, which is as expected. As the pulse width increases, the bandwidth of the power density increases too. According to Eq. 3-7 and Eq. 3-8, the theoretical and measured β can be calculated respectively, the results are shown in Fig. 3-8.

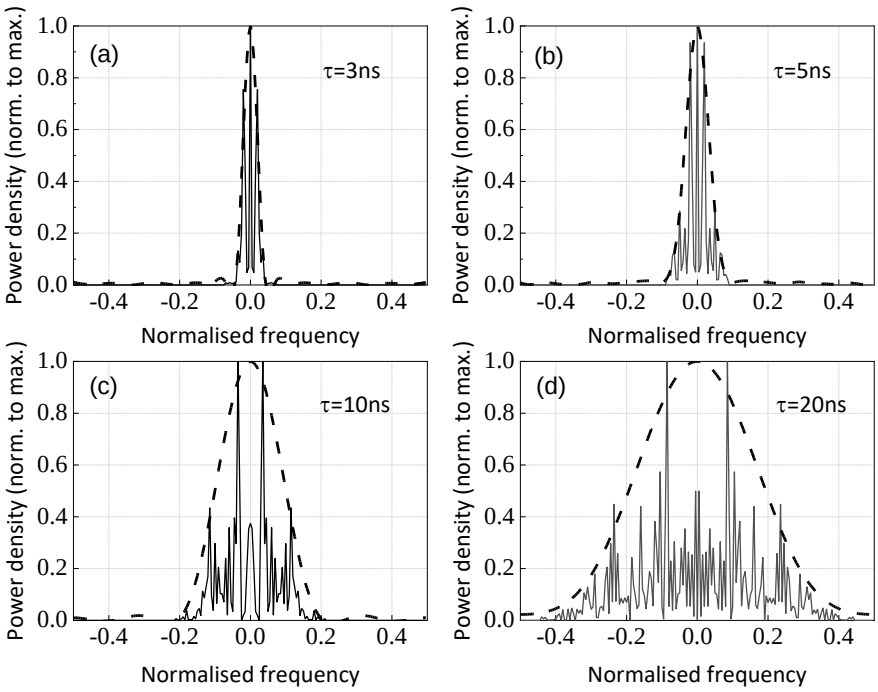

Figure 3-7: The power density $|U(f)|^2$ in case of pulse widths of (a) 3ns; (b) 5 ns; (c) 10 ns; (d) 20 ns (solid lines: power densities, dash lines: their envelops).

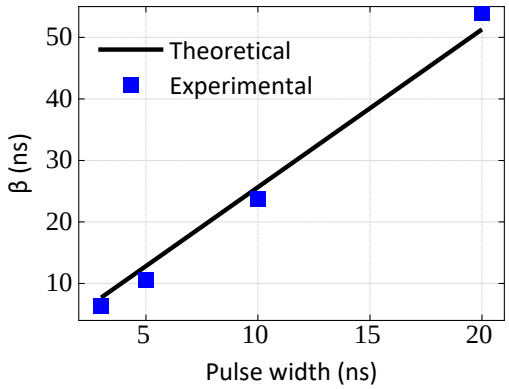

Figure 3-8: The change of β with pulse width.

Another parameter that affects the measurement accuracy is the signal-noise ratio M_o. In the Φ-OTDR, the RBS traces are random fluctuated patterns that follow exponential PDFs due to the non-uniformity of scattering points. In [123], it has been proved that the average value of the jagged intensity trace is nearly the same as the true optical power, and the noise level can be assessed by the standard deviation (SD) of the signal. Fig. 3-9 shows the SNR with different pulse widths, indicating a proportional

relationship between them. The fitting result shows a linearity of 0.9865.

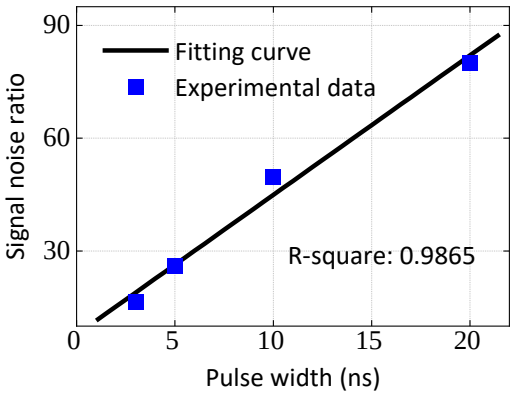

Figure 3-9: The change of signal-to-noise ratio M_o with pulse width.

From Fig. 3-8 and Fig. 3-9, as the pulse width increases, both the parameter β and M_o linearly increase, which will decrease the frequency shift estimation uncertainty σ in Eq. 3-6. Therefore, when the system noise is determined, increasing the pulse width will be effective for improving the measurement accuracy of the system. However, the spatial resolution will deteriorate as the increase of pulse width, which leads to a tradeoff between the SR and the measurement accuracy. As shown in Fig. 3-10, the theoretical frequency shift uncertainties calculated by Eq. 3-9 and the measured frequency uncertainties are presented in the black line and magenta dots, respectively. Since the measurement results of frequency shift at different fiber locations are independent, the frequency shift measurement uncertainties can be characterized by the SD of frequency shift at different fiber locations. To eliminate the influence of ambient perturbations like temperature change on system measurement uncertainty results, we calculate the SD every 2.5 m, and an average of SD was calculated from 0 m to 960 m. In Fig. 3-10, the vertical axis on the left shows the frequency shift measurement uncertainty and the vertical axis on the right shows the corresponding salinity measurement uncertainty with a coefficient of 782.4 MHz/(mol/L).

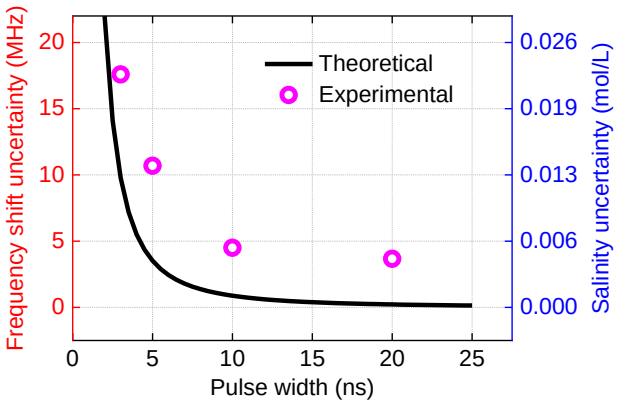

Figure 3-10: The measurement accuracy of frequency shift and salinity in case of different pulse widths.

In Fig. 3-10, the measured frequency uncertainties are larger than the theoretical frequency uncertainties. This is reasonable because the ambient perturbation will also result in measurement error although an average was used. The salinity uncertainty in the case of 20 ns is 0.005 mol/L (corresponding to 3.7 MHz frequency uncertainty), while the salinity uncertainty in the case of 3 ns is 0.022 mol/L (corresponding to 17.6 MHz frequency uncertainty).

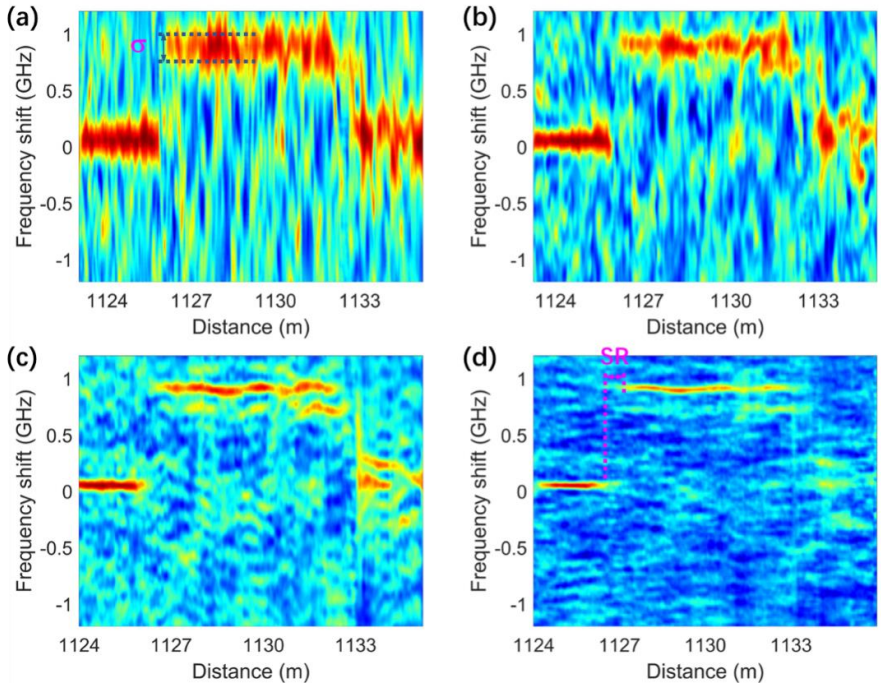

Figure 3-11: The measured cross-correlation spectra near the fiber end with pulse widths of (a) 3 ns; (b) 5 ns; (c) 10 ns; (d) 20 ns.

Fig. 3-11 demonstrates the cross-correlation of RBS spectra over the last ten meters of FUT where the salinity is changed. A clear trade-off between SR and frequency shift accuracy can be observed. As the pulse width increases from 3 ns to 20 ns, the frequency shift estimation results show less fluctuations. However, a wider rising edge can be seen at the location of the salinity jump, implying the deterioration of spatial resolution.

3.3.5 Discussion

Table 3.1 compares the salinity measurement performances of our salinity sensor with previous fiber-optic sensors. The proposed sensor employs an unmodified polyimide-coated single-mode fiber as the sensing medium, distributed salinity sensing can be realized over a long distance, and no complex process is required. Meanwhile, the proposed sensor shows a high salinity sensitivity, which enables good measurement accuracy. However, the cross-sensitivity between salinity and temperature can easily introduce errors in salinity measurement results. The following section will discuss how to mitigate the crosstalk between temperature and salinity, achieving simultaneous measurement of temperature and salinity.

Table 3.1 Comparison between frequency scanning Φ-OTDR with other fiber-optic sensors.

Technique	Sensitivity	Spatial resolution	Sensing range	Ref
FBG	15.40 nm/RI	-	-	[128]
MZI	64 pm/‰	-	-	[129]
F-P interferometer	0.45 nm/(mol/L)	-	-	[114]
SPR	0.3769 nm/‰	-	-	[130]
BDG	119 MHz/(mol/L)	15 cm	9 m	[75]
This work	782 MHz/(mol/L)	30 cm	1 km	

MZI: Mach-Zehnder interferometer.

3.4 Distributed salinity and temperature sensor based on frequency-scanning Φ-OTDR and polyimide-coated PMF

3.4.1 Principle of salinity and temperature discrimination using PMF

As is elaborated in Section 2.2, temperature or strain change will cause variations in the fiber RI and the distance between scatterers. When temperature and salinity change simultaneously, the variations of RI and the distance between scatterers are a superposition of the two effects. Under variations of temperature ΔT and strain $\Delta\varepsilon$, the refractive index of fiber core n_0 and the fiber length between m-th and n-th Rayleigh backscattering centers L_{mn} can be written as [131]:

$$n_0\left(T,\varepsilon\right)=n_0\left(T_0,\varepsilon_0\right)\left(1+c_\varepsilon\Delta\varepsilon+c_T\Delta T\right) \tag{3-10}$$

$$L_{mn}\left(T,\varepsilon\right)=L_{mn}\left(T_0,\varepsilon_0\right)\left(1+\Delta\varepsilon+p_T\Delta T\right) \tag{3-11}$$

where c_ε and c_T are strain coefficient and temperature coefficient of refractive index, respectively. p_T is the thermal expansion coefficient. To compensate for the phase change and recover the RBS intensity, the frequency shift of the light source $\Delta\nu$ should satisfy the following condition:

$$\begin{aligned}\frac{\Delta\nu}{\nu_0}&=-\left(1+c_\varepsilon\right)\Delta\varepsilon-\left(p_T+c_T\right)\Delta T\\&=\alpha_\varepsilon\Delta\varepsilon+\alpha_T\Delta T\end{aligned} \tag{3-12}$$

where ν_0 represents the frequency of the light source. α_ε and α_T denote the strain sensitivity coefficient and temperature sensitivity coefficient, respectively.

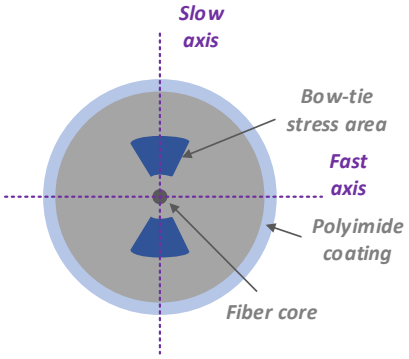

Figure 3-12: The cross section of polyimide-coated PMF.

SMFs are incapable of decoupling temperature and salinity. To address this issue, we employed a polyimide-coated bow-tie high birefringence PMF. Fig. 3-12 shows the cross section. A refractive index difference exists between the two polarization axes due to the introduction of the bow-tie stress region. Compared with common SMF whose modal birefringence is approximately 10^{-7}~10^{-5}, the birefringence of PMF can reach to 10^{-4} level. Therefore, the linearly polarized light can stably transmit along the fast axis or slow axis in PMF with its polarization state unchanged, and the fast polarization mode and slow polarization mode have different propagation constants.

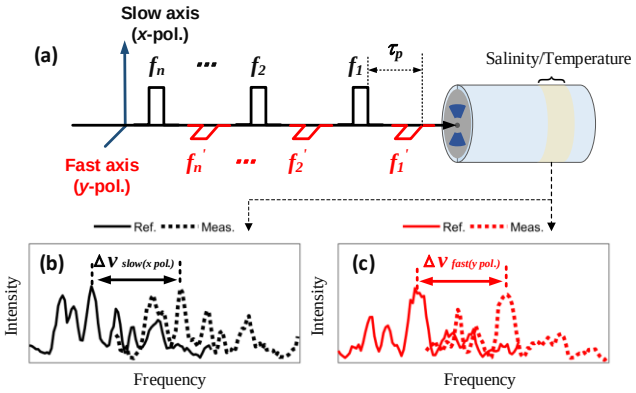

Figure 3-13: Principle of simultaneous salinity and temperature measurement. (b) The reference and the measurement Rayleigh backscattering spectra of the slow axis of disturbed area. (c) The reference and the measurement Rayleigh backscattering spectra of the fast axis of disturbed area.

The principle of using polyimide-coated PMF to simultaneously measure salinity and temperature is shown in Fig. 3-13. As shown in Fig. 3-13 (a), pulse sequences with

orthogonal polarization states are launched into the fast axis and slow axis of PMF respectively. To separately detect the backscattering light of the fast axis and slow axis, a time delay τ_p needs to be introduced between the two orthogonal pulse sequences. For each polarization axis, the pulse frequency is scanned with a certain frequency step, and two Rayleigh backscattering spectra can be obtained with one measurement. Due to the anisotropic structure of PMF, the Rayleigh spectra of the two polarization axes will show different frequency shifts under the variation of temperature or salinity, therefore enabling the discrimination between temperature and salinity with a single fiber. The frequency shifts of *x* polarization axis and *y* polarization axis $\Delta\nu_{x-pol.}, \Delta\nu_{y-pol.}$ can be written as the function of temperature variation ΔT and salinity (or strain) variation ΔS [132]:

$$\begin{bmatrix} \Delta\nu_{x-pol.} \\ \Delta\nu_{y-pol.} \end{bmatrix} = \begin{bmatrix} \alpha_{T,x-pol.} & \alpha_{S,x-pol.} \\ \alpha_{T,y-pol.} & \alpha_{S,y-pol.} \end{bmatrix} \begin{bmatrix} \Delta T \\ \Delta S \end{bmatrix}, \tag{3-13}$$

Where $\alpha_{T,x-pol.}$ and $\alpha_{S,x-pol.}$ are temperature and salinity sensitive coefficients of *x* polarization axis, $\alpha_{T,y-pol.}$ and $\alpha_{S,y-pol.}$ are temperature and salinity sensitive coefficients of *y* polarization axis. Once the four sensitivity coefficients are determined, independent temperature and salinity profiles can be retrieved by taking reverse matrix operation as follows:

$$\begin{bmatrix} \Delta T \\ \Delta S \end{bmatrix} = \frac{1}{\alpha_{T,x-pol.}\alpha_{S,y-pol.} - \alpha_{T,y-pol.}\alpha_{S,x-pol.}} \begin{bmatrix} \alpha_{S,y-pol.} & -\alpha_{S,x-pol.} \\ -\alpha_{T,y-pol.} & \alpha_{T,x-pol.} \end{bmatrix} \begin{bmatrix} \Delta\nu_{x-pol.} \\ \Delta\nu_{y-pol.} \end{bmatrix} \tag{3-14}$$

The measurement uncertainties for temperature $\sigma_{\Delta T}$ and salinity $\sigma_{\Delta S}$ can be calculated as follows [133]:

$$\sigma_{\Delta T}=\frac{\sqrt{\left(\alpha_{S,y-pol.}\cdot\sigma_{x-pol.}\right)^2+\left(\alpha_{S,x-pol.}\cdot\sigma_{y-pol.}\right)^2}}{\left|\alpha_{T,x-pol.}\alpha_{S,y-pol.}-\alpha_{T,y-pol.}\alpha_{S,x-pol.}\right|} \tag{3-15}$$

$$\sigma_{\Delta S}=\frac{\sqrt{\left(\alpha_{T,y-pol.}\cdot\sigma_{x-pol.}\right)^2+\left(\alpha_{T,x-pol.}\cdot\sigma_{y-pol.}\right)^2}}{\left|\alpha_{T,x-pol.}\alpha_{S,y-pol.}-\alpha_{T,y-pol.}\alpha_{S,x-pol.}\right|}\ , \tag{3-16}$$

where $\sigma_{x-pol.}$ and $\sigma_{x-pol.}$ stand for the measurement uncertainties in frequency shifts of *x* polarization axis and *y* polarization axis, respectively.

3.4.2 System configuration

The configuration of frequency-scanning Φ-OTDR is shown in Fig. 3-14. A narrow linewidth (100 Hz) laser operating at 1550 nm wavelength is used as the light source. The light is frequency-shifted by an EOM1 which works in a carrier-suppressed double-sideband modulation mode. The frequency scanning interval of the radio frequency source (RF) is 20 MHz, and the scanning range is between 17.5 GHz and 31.5 GHz. Then another EOM2 with a high extinction ratio larger than 30 dB modulates the continuous light into light pulses. The arbitrary waveform generator is used to produce a pulse signal to drive the EOM2. An EDFA is used to amplify the power of frequency-shifted light pulses. To separately probe the fast axis and slow axis of polyimide-coated PMF, the amplified light needs to be split into two beams with orthogonal polarization states and a time delay in between. To fully make use of the light power, a filter with a transmission end and a reflection end is used to split the upper sideband and lower sideband of the light pulse to serve as the *x* polarization state and *y* polarization state respectively. By employing a delay fiber with a length larger than twice the length of the FUT, the light in the *x*-polarization state and *y*-polarization state can be separated in the time domain. Two PCs are used to adjust the polarization states of light pulses in each branch to maximize the light power of two orthogonal polarization states aligned

to the polarization beam combiner (PBC). The combined light is launched into the polyimide-coated PMF through the circulator. The Rayleigh backscattering light is amplified by another EDFA with a bandpass filter (BPF) followed to remove the ASE noise generated by EDFA. Finally, a 200 MHz wide photodetector (PD, Thorlabs, PDB-450 C) converts the optical signal into an electric voltage and the detected signals are sent to the oscilloscope to be collected. In the experiment, the length of polyimide-coated PMF (Fibercore, HB1500P) is 100 m. Its operating wavelength is from 1520 nm to 1650 nm. The cladding diameter and the polyimide coating diameter are 125 μm and 155 μm respectively.

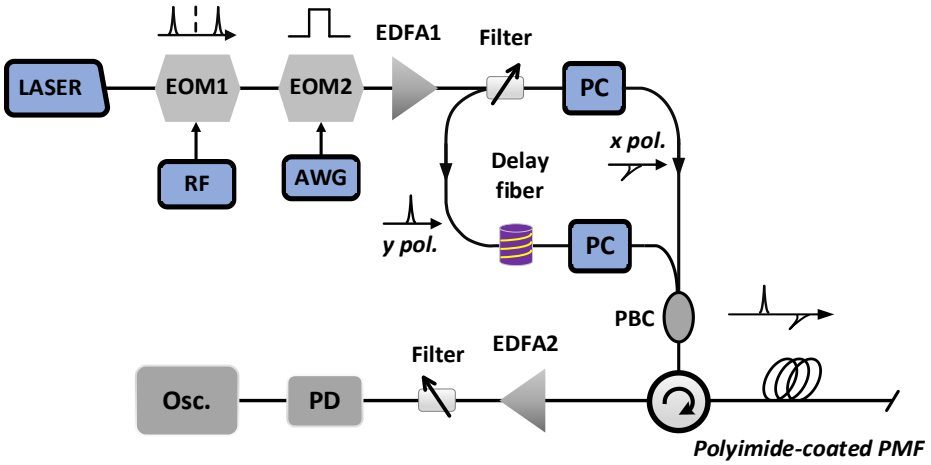

Figure 3-14: Schematic configuration of frequency scanning Φ-OTDR. EOM: electro-optic modulator; RF: radio frequency source; AWG: arbitrary waveform generator; EDFA: erbium-doped fiber amplifier; PC: polarization controller; PBC: polarization beam combiner; PD: photodetector; OSC: oscilloscope.

3.4.3 Characterization of temperature and salinity coefficients

To simultaneously measure the temperature and salinity profile along the fiber, a calibration experiment that specifies the four sensitivity coefficients related to temperature and salinity variation in Eq. (3-13) should be conducted first. To obtain the

temperature coefficients of fast and slow axes, a length of 6 m polyimide-coated PMF near the far end was immersed in the water bath with temperature control. The pulse width was 20 ns. Rayleigh backscattering trace was averaged 128 times, and the sampling rate of the oscilloscope was 2 GSa/s. Fig. 3-15 shows the measurement results for a temperature change of 1.5 K. Fig. 3-15 (a) and (b) represent the reference and measurement Rayleigh backscattering spectra for the *x*-axis and *y*-axis respectively (only a spectral range of 6 GHz is displayed for better visualization). Fig. 3-15 (c) displays the cross-correlation results between the reference and measurement spectra for both axes, revealing different frequency shifts under the same temperature change. Fig. 3-15 (d) and (e) demonstrate the frequency shift distributions along the fiber for the two axes, and the results are compared in Fig. 3-15 (f), with the *x*-axis and *y*-axis exhibiting frequency shifts of -2152 MHz and -2058 MHz, respectively.

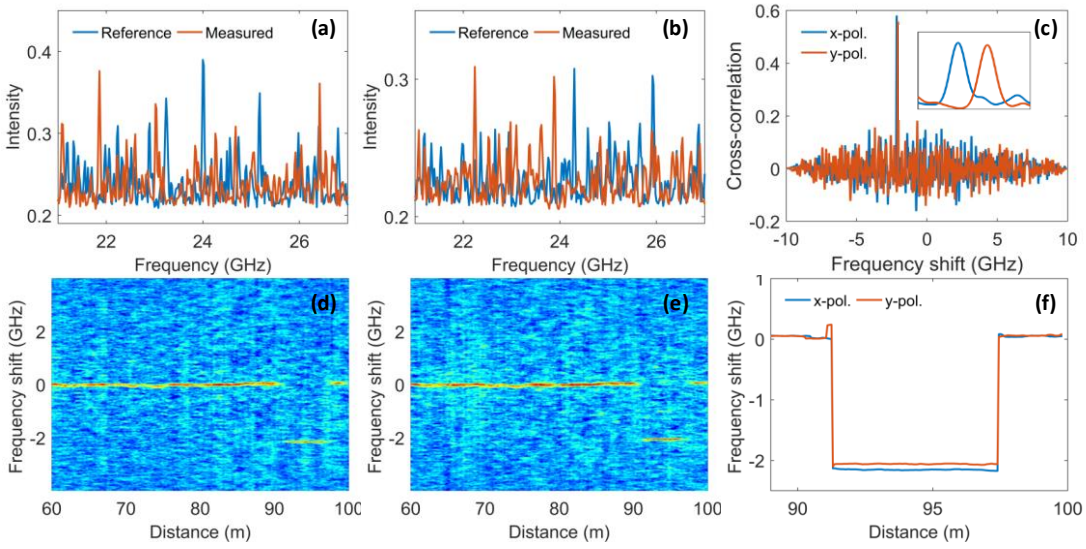

Figure 3-15 The reference and measurement Rayleigh backscattering spectra of (a) *x* polarization axis and (b) *y* polarization axis; (c) Cross-correlation results of frequency spectra of the two polarization states. (d-e) The frequency shift distributions along the sensing fiber of *x* polarization axis and *y* polarization axis; (f) The frequency shifts of the two axes between 89 m and 100 m.

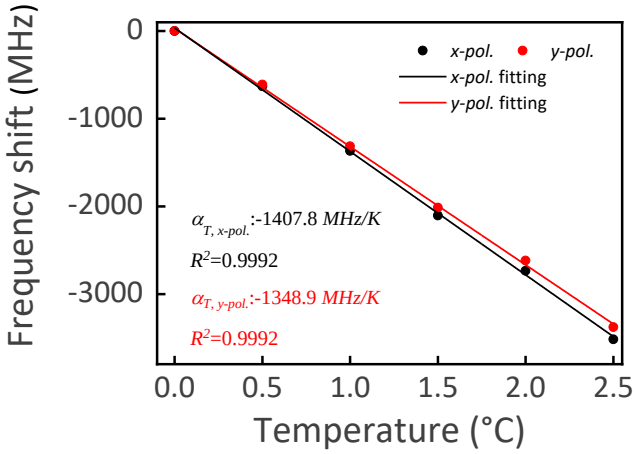

Figure 3-16: Temperature sensitivities of the proposed sensor. The dots are averaged results of 5 measurements. The lines are linear least square fitting to the data.

Fig. 3-16 shows the temperature coefficient measurement results. The temperature changes with a 0.5 K increment step from 0 K to 2.5 K. To improve the measurement accuracy, we repeated the measurement 5 times for each temperature and took the average value. The linear least square fitting results of *x* polarization and *y* polarization suggest -1407.8 MHz/K and -1348.9 MHz/K sensitivities, respectively.

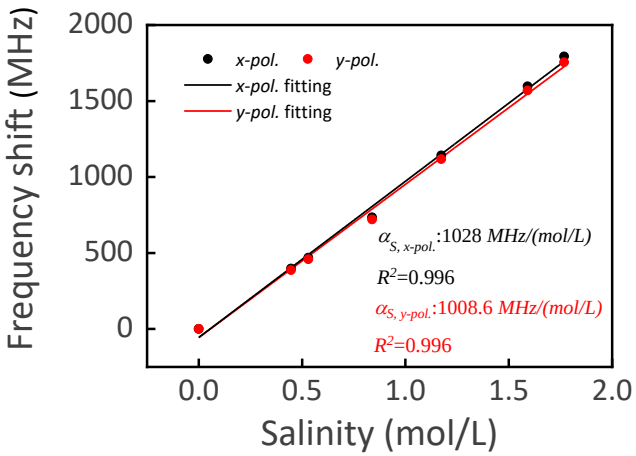

Figure 3-17: Salinity sensitivities of the proposed sensor.

In the salinity coefficient measurement experiments, the frequency shifts of different salinities are acquired by cross-correlating the reference RBS spectrum when the polyimide-coated PMF is in pure water and the measurement RBS spectrum when

the polyimide-coated PMF is in a certain concentration of NaCl solution. For comparison, a commercially available salinometer with a nominal range of 1.7 mol/L and measurement accuracy of 0.05 mol/L is used to measure the salinity of the solution at the same time. The pulse width is 5 ns, leading to a 0.5 m spatial resolution. The average time of trace and the sampling rate of the oscilloscope are 32 and 5 GSa/s, respectively. Fig. 3-17 demonstrates the measured frequency shift results of the *x* polarization state and *y* polarization state in the case of different salinities. The frequency shift exhibits a positive linear relationship with the salinity, indicating the linear response of polyimide coating-induced strain to salinity. The least-square fitting curves of *x* polarization axis and *y* polarization axis have slopes of 1028 MHz/(mol/L) and 1008.6 MHz/(mol/L), respectively.

3.4.4 Measurement results of response time to salinity change

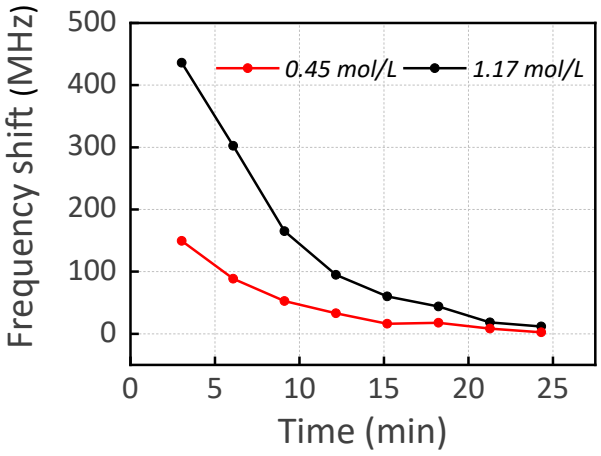

Figure 3-18: The response time of polyimide-coated fiber to salinity variation.

Then, we investigated the response time of the polyimide-coated fiber to salinity variation. Before the data acquisition of the reference spectrum, the polyimide-coated PMF with a length of 4 m was immersed in a water solution and left still for 2 hours to ensure the polyimide coating fully responded to the solution. After the reference

spectrum collection was finished, NaCl solution was poured in, and the RBS spectrum was collected every 3 minutes. In total, nine RBS spectra including the reference spectrum were detected. In data processing, the frequency shifts were calculated between every two adjacent RBS spectra. The measurement results for salinity of 0.45 mol/L and 1.17 mol/L are depicted in Fig. 3-18. It can be seen that the frequency shifts gradually approach zero as time increases. At the 21*st* minute, the response time curves reach a stable state.

3.4.5 Simultaneous temperature and salinity measurement results

After the sensitivity coefficients of temperature and salinity have been determined, the characteristic matrix in Eq. (3-13) can be obtained, enabling the simultaneous measurement of salinity and temperature. To validate the sensor's discrimination capability between temperature and salinity, we set up the optical fiber according to the configuration shown in Fig. 3-19. At about 58.2 m away from the incident end of the fiber, a 4.4 m long polyimide-coated PMF was placed in a temperature-controlled water bath for temperature measurement. The following 5 m was in the air and then 4.6 m long fiber was immersed in pure water for salinity detection.

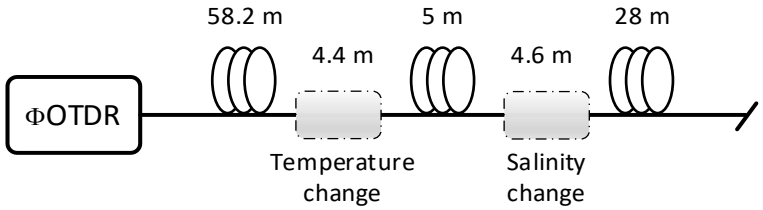

Figure 3-19: The deployment of polyimide-coated PMF for simultaneous temperature and salinity measurement.

Then the simultaneous measurement experiments for temperature and salinity were carried out. The pulse width, sampling rate, and trace averaging were set to be 20 ns, 5 GSa/s, and 32, respectively. Fig. 3-20 (a-c) shows the measurement results with a

temperature variation of 2 K and a salinity variation of 0.835 mol/L. Fig. 3-20 (a) depicts the frequency shift distributions of *x*-axis and *y*-axis along the fiber. It can be seen that the temperature change between 58.2 m to 62.6 m causes a negative frequency shift, while the salinity change between 67.6 m to 72.2 m leads to a positive frequency shift. This is as expected since the temperature coefficients are negative, but the salinity coefficients are positive. The inset zooms in on the frequency shift from 67.6 m to 72.2 m for better visualization. Fig. 3-20 (b) and (c) show the demodulated temperature and salinity profiles using the obtained characteristic matrix, in which the temperature and salinity are 1.95 K and 0.815 mol/L, respectively. Compared to the expected values, the measurement errors for temperature and salinity are 0.05 K and 0.02 mol/L, respectively. Fig. 3-20 (d-f) shows another group of measurement results with a temperature variation of 3 K and a salinity variation of 1.66 mol/L. The demodulation results of temperature and salinity in Fig. 3-20 (e) and (f) are 2.93 K and 1.72 mol/L respectively, slightly deviating from the true value. The experimental results agree very well with the values of applied parameters, demonstrating the sensor's remarkable ability to discriminate between temperature and salinity.

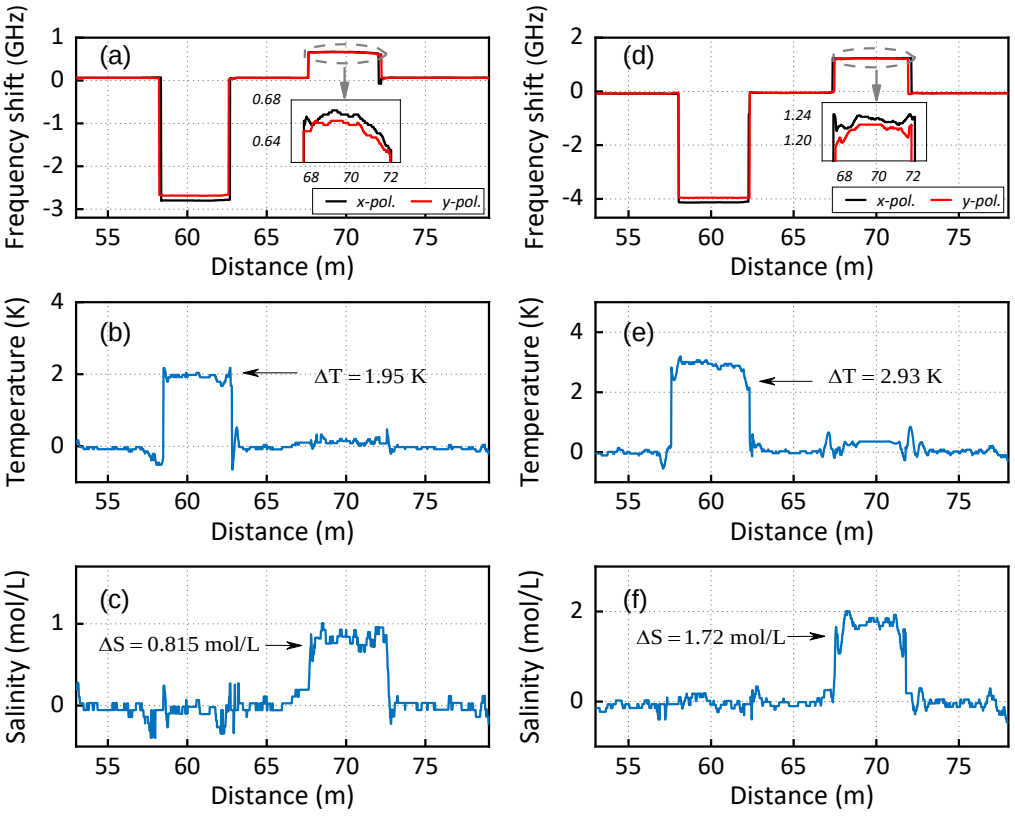

Figure 3-20: (a) Frequency shifts of *x* polarization axis and *y* polarization axis (T=2 K, S=0.835 mol/L); (b) Demodulated temperature profile (T=2 K, S=0.835 mol/L); (c) Demodulated salinity profile (T=2 K, S=0.835 mol/L); (d) Frequency shifts of *x* polarization axis and *y* polarization axis (T=3 K, S=1.66 mol/L); (e) Demodulated temperature profile (T=3 K, S=1.66 mol/L); (f) Demodulated salinity profile (T=3 K, S=1.66 mol/L).

In Fig. 3-20 (e), a tiny temperature change (~0.3 K) can be still observed between the positions 67.6 m and 72.2 m. Several factors may contribute to this phenomenon. Firstly, although the water and NaCl solutions have been placed in a stable environment for a long time to reach a steady state, the temperature of the two solutions cannot be identical, and small temperature fluctuations may occur in the measurement. Secondly, the temperature and salinity measurement by the water bath and salinometer exhibit certain inaccuracies, which results in slight deviations between the calibrated sensitivity coefficients and the true values, also leading to some errors in the demodulation results. Utilizing a more precise thermometer and salinometer can achieve a more accurate

estimation of sensitivity coefficients, thereby reducing measurement errors.

Comparing Fig. 3-20 (b) and (e) to Fig. 3-20 (c) and (f), we can find that the fluctuations of salinity measurement results along the fiber are larger than those of temperature measurement results. This phenomenon can be explained by the error estimation formula in Eq. (3-15) and Eq. (3-16), which have indicated that the measurement uncertainty of salinity is determined by the higher temperature sensitivity coefficients, while the temperature measurement uncertainty is essentially dominated by the lower salinity sensitivity coefficients. The measurement uncertainties of frequency shifts on *x* polarization axis and *y* polarization axis $(\sigma_{x-pol.}, \sigma_{y-pol.})$ can be characterized by calculating the standard deviations of frequency shifts at different fiber locations. In Fig. 3-20 (a), we chose the fiber position from 53 m to 56 m to calculate the standard deviations, which are 0.4495 MHz for *x* polarization axis and 1.0338 MHz for *y* polarization axis, respectively. According to Eq. (3-15) and Eq. (3-16), the estimated measurement uncertainties for temperature and salinity $(\sigma_{\Delta T}, \sigma_{\Delta S})$ should be 0.0352 K and 0.048 mol/L, respectively. These values match well with the measurement uncertainties on the same location of profiles in Fig. 3-20 (b) and (c), which are 0.0344 K and 0.0469 mol/L respectively.

In the conducted experiment, the frequency scanning range of the optical pulse extended to 14 GHz, enabling the detection of salinity levels up to approximately 6.8 mol/L. Given that the average salinity of ocean water is about 0.6 mol/L, our system's dynamic range comfortably exceeds that of marine environments. Furthermore, the measurement precision achieved is 0.0469 mol/L, which is considerably finer than the typical salinity of seawater, thus fulfilling the demands of practical applications. Regarding real-time monitoring, the response time of the polyimide

coating to variations in salinity is currently around 8 minutes. Consequently, employing frequency-scanning Φ-OTDR for salinity assessment meets and potentially surpasses the existing operational requirements.

3.5 Summary

In this chapter, we introduce a novel approach for high-sensitivity distributed salinity sensing that integrates frequency-scanning Φ-OTDR with polyimide-coated fibers. Our initial experiments utilize an SMF with a coating radius of 15 μm to gauge salinity levels. This setup yields a salinity sensitivity of 782.4 MHz/(mol/L) and achieves an SR of 1 m. We further examine the fiber's response time to changes in salinity, determining that it takes approximately 8 minutes to stabilize after variations of both 0.48 mol/L and 1.76 mol/L. Subsequently, we delve into the theoretical and practical aspects of measurement accuracy within the context of frequency-scanning Φ-OTDR. Our findings indicate a compromise between SR and the precision of frequency shift measurements related to salinity. Experimental data points to a measurement uncertainty of 0.005 mol/L and 0.022 mol/L for interrogation pulse widths of 20 ns and 3 ns, respectively.

Moreover, we extend our research to achieve concurrent measurements of salinity and temperature using a polyimide-coated PMF. The frequency-scanning Φ-OTDR system dispatches pulse sequences with orthogonal polarization states to independently track the optical path variations along the PMF's fast and slow axes. By scrutinizing the frequency shifts in the Rayleigh backscattering spectra, we ascertain the temperature and salinity sensitivity coefficients for the slow and fast axes of the polyimide-coated PMF. These coefficients are determined to be -1407.8 MHz/K and -1348.9 MHz/K for temperature, and 1028 MHz/(mol/L) and 1008.6 MHz/(mol/L) for salinity, respectively.

Through our experiments, we successfully demonstrate the capability of this system to perform simultaneous salinity and temperature measurements, with uncertainties of 0.0344 K for temperature and 0.0469 mol/L for salinity. The proposed system offers a promising solution for distributed, discriminative salinity and temperature sensing with high sensitivity and minimal measurement errors, making it suitable for applications that demand precise monitoring of these parameters.

4 Large Dynamic Range Distributed Fiber Sensor Based on Dual-Sideband Linear Frequency Modulated COTDR

4.1 Introduction

Dynamic range, which refers to the maximum range of measurand, is a crucial parameter for DOFS. In this chapter, we propose a COTDR based on a dual-sideband LFM pulse to enhance the dynamic range. The COTDR system utilizing the sub-chirp-pulse extraction algorithm offers several advantages, including fading immunity, high SNR, high SR, and the ability to perform single-shot measurements [46]. However, its dynamic range is limited by the frequency tuning range of the LFM pulse.

To address this constraint, we have developed a COTDR system that utilizes a dual-sideband LFM pulse. This system incorporates I/Q demodulation, enabling the effective demodulation of both the positive and negative frequency bands within the RBS signal. Consequently, this approach leads to a doubling of the dynamic range while circumventing the necessity to expand the bandwidth of the signal generator, PD, and oscilloscope.

In our experiment, we launch a chirped pulse with a pulse width of 10 μs and a frequency sweeping range of 498 MHz into the sensing fiber. With this setup, we achieve single-shot strain measurement over a 5 km single-mode fiber, providing an SR of 2.5 m and a strain sensitivity of 7.5 $p\varepsilon/\sqrt{Hz}$. Additionally, we successfully

measure a vibration signal with a peak-to-peak amplitude of 3.09 $\mu\varepsilon$ (corresponding to a 461 MHz frequency shift) using the double-sideband spectrum. This vibration signal cannot be accurately recovered using the single-sideband spectrum.

4.2 Principle of COTDR based on dual-frequency sidebands

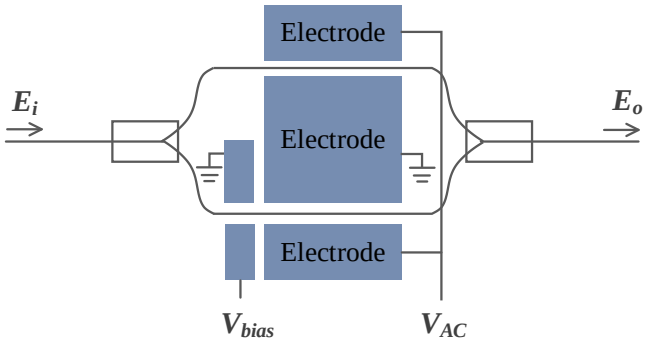

Figure 4-1: EOM based on MZI structure [100].

As shown in Fig. 4-1, a Mach–Zehnder EOM can be used to generate the dual sideband signal. In the EOM, the incident light is divided into two arms equally and recombined subsequently. Supposing that the phase delays of light in the two arms are φ_1 and φ_2, the input optical fields is E_i, and the output optical field E_o can be written as:

$$E_o = \frac{1}{2}(e^{j\varphi_1} + e^{j\varphi_2})E_i = \cos(\frac{\varphi_1 - \varphi_2}{2})e^{j\frac{\varphi_1+\varphi_2}{2}}E_i \tag{4-1}$$

The phase shifts of the two arms are given by:

$$\varphi_1 = \varphi_0 + \frac{\pi V_{AC}(t)}{2V_\pi} \tag{4-2}$$

$$\varphi_2 = \frac{\pi[V_{bias} - V_{AC}(t)]}{2V_\pi} \tag{4-3}$$

where φ_0 represents the inherent phase difference between the two arms without applied voltages. V_{bias} represents the bias voltage and the modulation voltage is expressed as $V_{AC}(t) = V_{AC}\cos(\omega_{AC}t)$, respectively. V_π means the half-wave voltage of

the modulator, which is the required voltage for the output light intensity to change from minimum to maximum. With Eq. (4-1) to Eq. (4-3), we can get:

$$E_o = \cos\left(\frac{\pi V_{AC}\cos(\omega_{AC}t)}{2V_\pi} - \frac{\pi V_{bias}}{4V_\pi} + \frac{\varphi_0}{2}\right) e^{j\left(\frac{\varphi_0}{2}+\frac{\pi V_{bias}}{4V_\pi}\right)} E_i \tag{4-4}$$

Considering the angle addition formulas and the real-valued expression of Jacobi–Anger expansion:

$$\cos(\alpha+\beta) = \cos(\alpha)\cos(\beta) - \sin(\alpha)\sin(\beta) \tag{4-5}$$

$$\cos(z\cos\theta) = J_0(z) + 2\sum_{n=1}^{\infty}(-1)^n J_{2n}(z)\cos(2n\theta) \tag{4-6}$$

$$\sin(z\cos\theta) = -2\sum_{n=1}^{\infty}(-1)^n J_{2n-1}(z)\cos\left((2n-1)\theta\right) \tag{4-7}$$

Eq. (4-4) can be expanded as follows:

$$\begin{aligned} E_o = E_i e^{j\left(\frac{\varphi_0}{2}+\frac{\pi V_{bias}}{4V_\pi}\right)} \Bigg\{ & \cos\left(\frac{\varphi_0}{2} - \frac{\pi V_{bias}}{4V_\pi}\right) J_0\left(\frac{\pi V_{AC}}{2V_\pi}\right) \\ & + 2\cos\left(\frac{\varphi_0}{2} - \frac{\pi V_{bias}}{4V_\pi}\right)\sum_{n=1}^{\infty}(-1)^n J_{2n}\left(\frac{\pi V_{AC}}{2V_\pi}\right)\cos(2n\omega_{AC}t) \\ & + 2\sin\left(\frac{\varphi_0}{2} - \frac{\pi V_{bias}}{4V_\pi}\right)\sum_{n=1}^{\infty}(-1)^n J_{2n-1}\left(\frac{\pi V_{AC}}{2V_\pi}\right)\cos\left[(2n-1)\omega_{AC}t\right]\Bigg\} \end{aligned} \tag{4-8}$$

$J_n()$ is the n-order *Bessel* function. When $\varphi_0/2-(\pi V_{bias})/4V_\pi=\pi/2$ and $\pi V_{AC}/2V_\pi \ll 1$ are satisfied, the EOM works at the null point, and the optical carrier and the higher order sidebands are suppressed. Only the first-order positive and negative sidebands need to be considered. In this situation, Eq. (4-8) can be simplified:

$$\begin{aligned} E_o(t) &= E_i e^{j[\frac{\varphi_0}{2}+\frac{\pi V_{bias}}{4V_\pi}]}\left[-2J_1(\frac{\pi V_{AC}}{2V_\pi})\cos(\omega_{AC}t)\right] \\ &= E_i e^{j[\frac{\varphi_0}{2}+\frac{\pi V_{bias}}{4V_\pi}]}\cdot\left\{-J_1(\frac{\pi V_{AC}}{2V_\pi})\cdot\left[\exp(j\omega_{AC}t)+\exp(-j\omega_{AC}t)\right]\right\} \end{aligned} \tag{4-9}$$

In pulse compression COTDR, an LFM pulse signal generated by the AWG drives the modulator, which can be written as:

$$\theta(t) = \left(2\pi f_0 t + \pi\kappa t^2\right) \cdot rect\left(\frac{t}{T}\right) \tag{4-10}$$

The output light field of modulator $E_o(t)$ can be written as

$$E_o(t) = -J_1(\frac{\pi\gamma}{2}) E_i e^{j[\frac{\varphi_0}{2} + \frac{\pi V_{bias}}{4V_\pi}]} \cdot \left\{\exp[\, j(2\pi f_c t + \theta(t))] + \exp[\, j(2\pi f_c t - \theta(t))]\right\} rect\left(\frac{t}{T}\right) \tag{4-11}$$

where $\gamma = V_{AC}/V_p$ is the modulation depth, f_c, f_0, and κ represent the optical carrier frequency, initial sweeping frequency, and the slope of the LFM signal, and T denotes the pulse duration. The Rayleigh backscattering signal probed with the LFM pulse is mixed with the LO to obtain the beat signal. The RBS signal and the LO can be written as:

$$E_{RBS}(t) = \sum_{i=1}^{N} r_i \exp\left(-\alpha \frac{c\tau_i}{n}\right) E_0(t - \tau_i) \tag{4-12}$$

$$E_L(t) = E_{LO} \exp(j2\pi f_c t) \tag{4-13}$$

Using an optical hybrid coupler, the optical field of the beat signal can be recovered using the I and Q components:

$$\begin{aligned} E_s(t) &\propto E_{RBS} E_{LO}^* \\ &= \sum_{i=1}^{N} a_i \cdot \left\{\exp\left[\, j\left(-2\pi f_c \tau_i + \theta(t - \tau_i)\right)\right] + \exp\left[\, j\left(-2\pi f_c \tau_i - \theta(t - \tau_i)\right)\right]\right\} rect\left(\frac{t - \tau_i}{T}\right) \end{aligned} \tag{4-14}$$

In the above equations, $a_i = -J_1(\frac{\pi\gamma}{2}) E_{LO} E_i e^{j[\frac{\varphi_0}{2} + \frac{\pi V_{bias}}{4V_\pi}]} r_i \exp(-\alpha \frac{c\tau_i}{n})$, r_i and t_i represent the amplitude and time delay of light reflected by the i-th reflector in FUT, and a is the fiber attenuation.

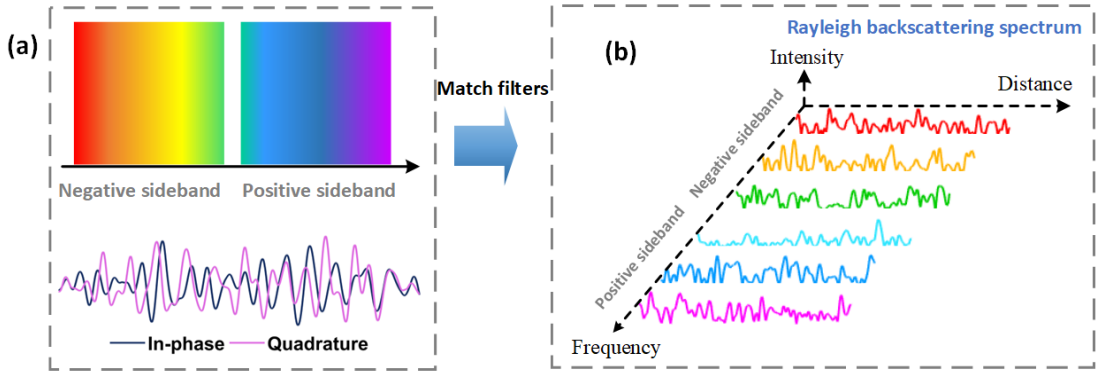

Figure 4-2: Principle of COTDR based on double frequency sidebands: (a) The detected RBS traces and the corresponding frequency spectrum; (b) The Rayleigh backscattering spectrum.

As shown in Eq. (4-14) and Fig. 4-2, the detected complex signal contains two frequency sidebands with different information. The RBS signals with different frequencies can be derived using matched filters with different frequency sweep ranges. Hypothesizing sub-chirped pulse sequence with initial frequency f_k and duration T_1 is used to perform matched filtering on positive and negative bands:

$$h_{+}(t) = \exp\{j(2\pi f_k t + \pi\kappa t^2)\} rect(t/T_1) \tag{4-15 a}$$

$$h_{-}(t) = \exp\{-j(2\pi f_k t + \pi\kappa t^2)\} rect(t/T_1) \tag{4-15 b}$$

The compressed signal of the *k-th* matched filter can be deduced according to Eq. (4-14) and (4-15):

$$\begin{aligned} s(t) &= E_s(t) * h_{+/-}(t) \\ &= -J_1(\frac{\pi\gamma}{2}) E_{Lo} E_i e^{j[\frac{\varphi_0}{2} + \frac{\pi V_{bias}}{4V_\pi}]} h_{FUT} * \left[\frac{\sin[\pi\kappa(T_1 - |t|)t]}{\pi\kappa t} \cdot \exp\left(\pm j2\pi(f_k + \frac{\kappa T_1}{2})t \right) \right] \end{aligned} \tag{4-16}$$

where $h_{FUT} = \sum_{i=1}^{N} r_i \exp(-\alpha \frac{c\tau_i}{n}) \cdot \exp\{-j2\pi f_c \tau_i\} \cdot \delta(t - \tau_i)$ is the impulse response of FUT. As can be seen from the above deduction the compressed signal is the convolution of h_{FUT} and a *sinc* function with different frequencies. Therefore, an RBS spectrum as

the function of time and frequency $s(t,f)$ can be constructed using matched filters with different center frequencies.

4.3 Experiments

4.3.1 System configuration

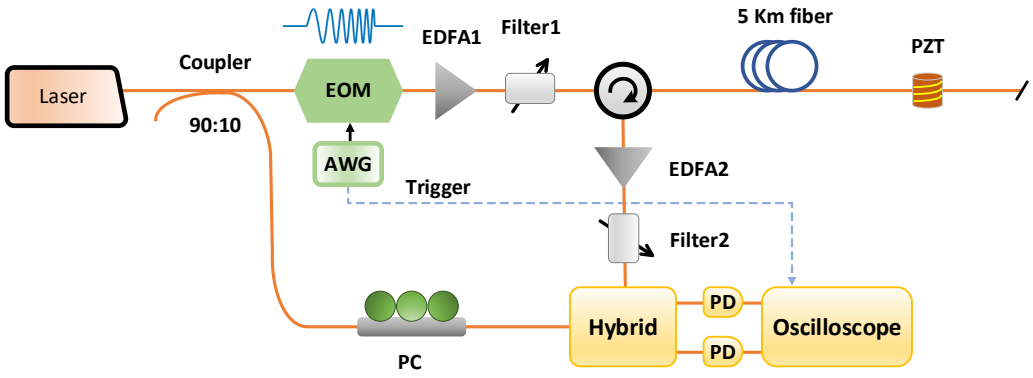

Figure 4-3: System configuration of dual-sideband COTDR based on pulse compression.

The configuration of dual-sideband COTDR is presented in Fig. 4-3. A laser with a narrow linewidth of 100 Hz operating at 1550 nm was split in a 90:10 ratio. In the upper branch, the light was modulated into a chirped pulse by an EOM driven by an AWG. The frequency of the chirp signal sweeps from 2 to 500 MHz, the pulse width and pulse period were 10 μs and 150 μs respectively. An EDFA and a bandpass filter were used to amplify the power of the chirp pulse and remove the ASE noise. Later, the amplified pulse was injected into a 5-km sensing fiber. And the Rayleigh backscattering light was amplified and filtered by another group of EDFA and bandpass filter. The fiber length of PZT was 10 m and it was put at the far end of the 5 km sensing fiber. In the lower branch, a PC was employed to control the polarization state of the LO. Finally, the LO in the lower branch and the backscattering signal were mixed in an optical hybrid. Two photodetectors with 500 MHz bandwidths were utilized to receive the I and Q

components and the detected signals were sent to the oscilloscope to be collected at the sampling rate of 2 GSa/s.

4.3.2 Frequency shift estimation based on a least mean square algorithm

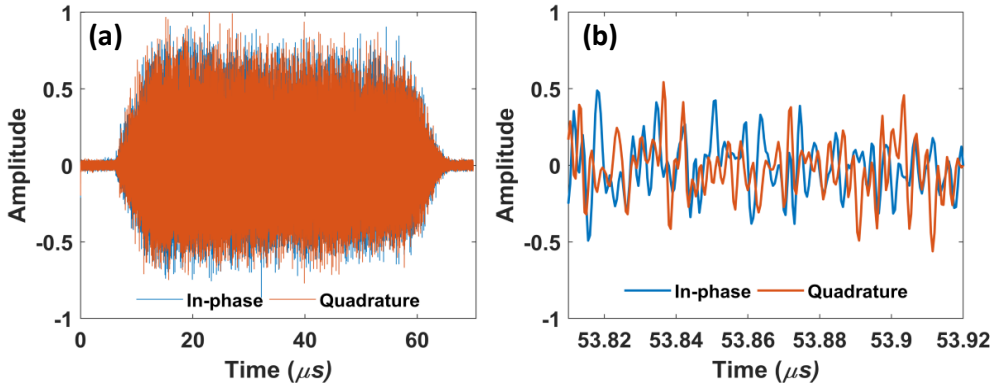

Figure 4-4: (a) The detected dual-sideband RBS signal. (b) A magnified view of Fig. 4-4 (a).

Fig. 4-4 (a) shows the detected In-phase and Quadrature components of Raleigh backscattering signal in a dual-sideband LFM COTDR system, and Fig. 4-4 (b) shows a magnified view at positions from 53.82 μs to 53.92 μs. In Fig. 4-4 (b), the intensities and phases of the I and Q components are different. The Rayleigh spectrum is constructed using matching filtering to the complex signal in Fig. 4-4 (a). The Rayleigh backscattering spectrum after match filtering is shown in Fig. 4-5, where different colors represent different RBS intensities. In our demodulation process, the bandwidth of the matched filter is 40 MHz and the frequency interval is 4 MHz, which results in 114 traces available for each sideband. It should be noted that the 44 MHz frequency spectrum around carrier frequency is not available (interpolate to 0 in Fig. 4-5) since the initial sweeping frequency is 2 MHz. During the frequency shift estimation process, if the commonly used cross-correlation algorithm is employed, the missed 44 MHz in the spectrum may adversely affect the frequency shift estimation result and potentially lead to erroneous estimations. To mitigate the impact of the missed 44 MHz spectrum

on the frequency shift estimation result, we utilized the frequency shift estimation based on a least mean square (LMS) algorithm here.

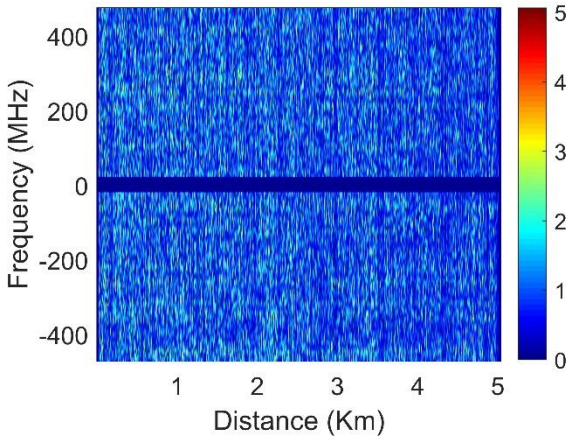

Figure 4-5: Rayleigh backscattering spectrum after match filtering.

Supposing that the Rayleigh spectrum range is F, the reference and the measurement RBS spectrum are represented by S_{ref} and S_{mea}, respectively. The mean square error with a frequency shift of δf is given by [43]:

$$R_{ref,mea}(t,\delta f)=\frac{1}{F-|\delta f|}\cdot\sum_{f=-(F-|\delta f|)}^{F-|\delta f|}\left[s_{ref}(t,\ f+\delta f)-s_{mea}(t,\ f)\right]^2 \tag{4-17}$$

The frequency shift is given by:

$$f_{shift}(t)=\arg\min_{\delta f}[R_{ref,mea}(t,\delta f)] \tag{4-18}$$

Fig. 4-6 illustrates the process of estimating frequency shift using the LMS algorithm. The figure presents two double sideband spectra, depicted in red and blue. Two spectra exhibit a strain-induced frequency shift relative to each other. The dotted lines shaded in blue represent the 44 MHz regions that are missing from the spectra. Using the blue spectrum as a reference, the red spectrum is shifted along the frequency axis incrementally. At each shift, the square errors between the two spectra are computed over their overlapping regions. The mean square error is then determined by averaging

these square errors, with the caveat that the shaded areas (the 44 MHz missed areas) are not included in the averaging process. The frequency shift caused by strain is identified by locating the position where the mean square error is minimized. Since the shaded areas are excluded in the calculation process, it doesn't affect the frequency shift results. To improve the accuracy, the frequency spectrum interval is interpolated to be 0.04 MHz by using cubic polynomial interpolation with a factor of 100.

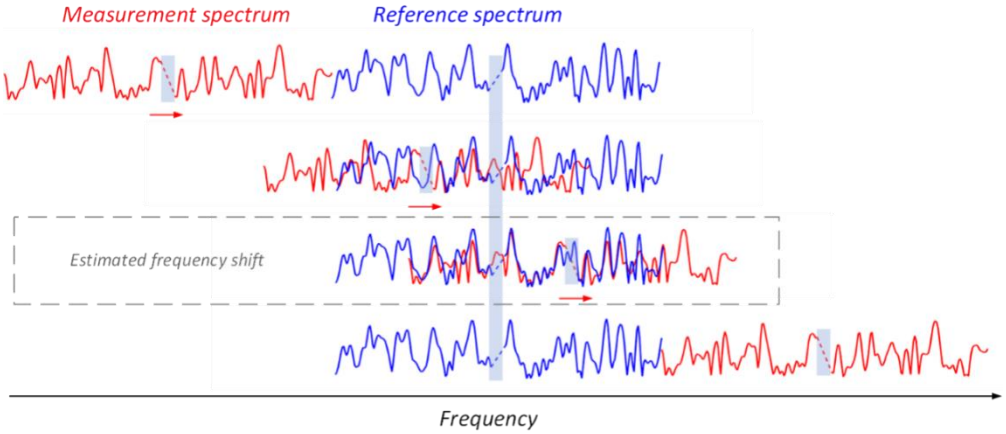

Figure 4-6: Frequency shift estimation principle based on LMS algorithm.

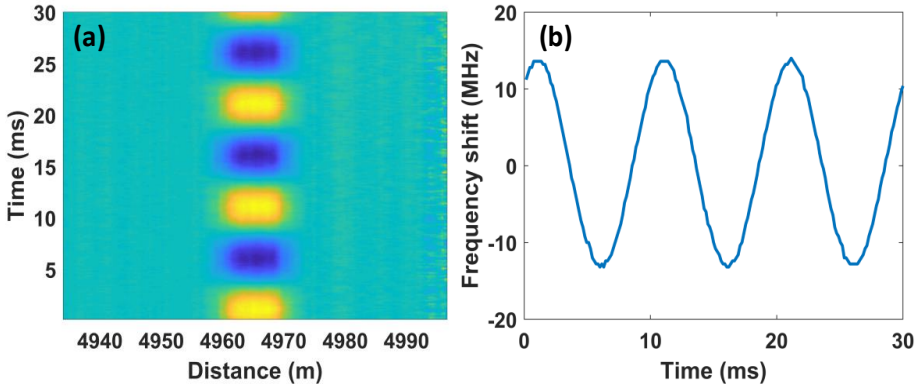

Figure 4-7: (a) The frequency shift result near the end of FUT. (b) The vibration at 4965 m.

Fig. 4-7 shows the calculated frequency shift map near the end of FUT. The applied voltage and frequency are 2 V and 100 Hz, respectively. A disturbed area can be identified from 4960 m to 4970 m. Fig. 4-7 (b) is the time trace of vibration at 4965 m, we can see that the *sine* waveform is well recovered with the LMS algorithm

4.3.3 Measurement results of dynamic strains

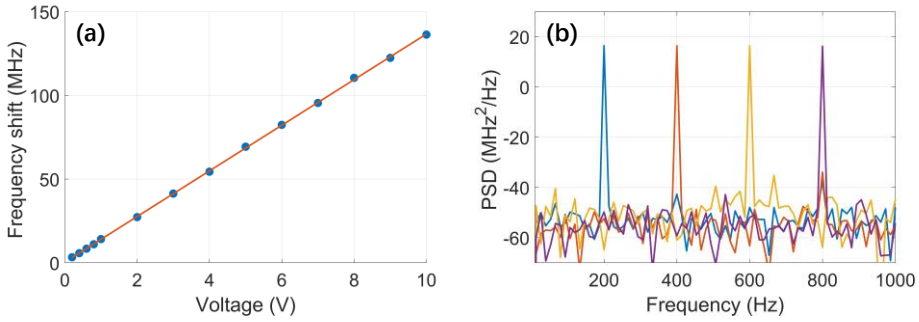

Figure 4-8: (a) Frequency shifts of RBS at different voltage; (b) Measured frequency spectra of different frequency vibrations.

Firstly, we measured the vibration signals with different amplitudes and different frequencies. The measurement results are displayed in Fig. 4-8. The vibration voltages applied to the PZT changed from 0.2 V to 10 V in Fig. 4-8 (a), and the frequency was kept at 100 Hz. The frequency shift coefficient is 13.63 MHz/V, and the coefficient of determination is 0.9999, suggesting a good linearity between the frequency shift and the amplitude of the vibration. Figure 4.8 (b) depicts the measurement results of vibrations with an amplitude of 5 V and frequencies ranging from 200 Hz to 800 Hz, which are consistent with the applied signals.

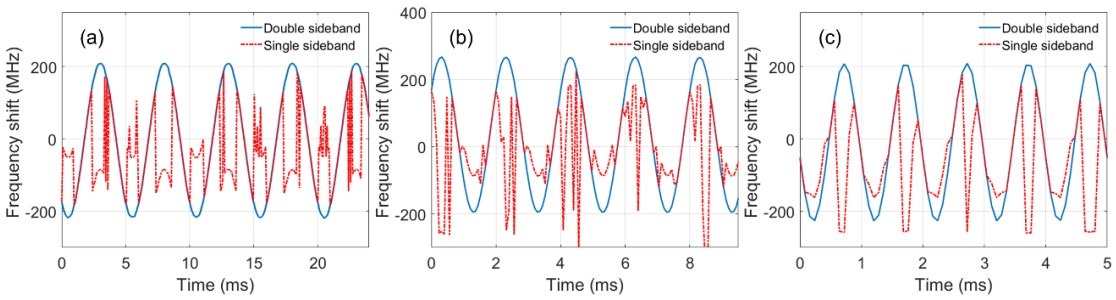

Figure 4-9: The measurement results of large amplitude vibrations (a) 200 Hz; (b) 500 Hz; (c) 1 KHz. (Blue: double sideband; Red: single sideband).

To investigate the dynamic range of our method, we used a piezo controller to amplify the vibration signal applied to the PZT. The pulse width and pulse period are

10 *m*s and 80 *m*s respectively in this case. Fig. 4-9 (a), (b), and (c) show the measurement results of vibrations with frequencies of 200 Hz, 500 Hz, 1 KHz, and amplitudes of 31 V, 34 V, and 32 V, respectively. The frequency shifts reach 424 MHz, 461 MHz, and 434 MHz, respectively. We can see that the results demodulated from the single-sideband frequency spectra are distorted, while the waveforms can be perfectly retrieved from the double-sideband spectra. In the demodulation process, a fixed reference RBS spectrum is used, and the maximum frequency shift between the measured spectrum and reference spectrum is 267 MHz (in Fig. 4-9 (b)). The strain range can be extended by calculating the frequency shifts between every two consecutive RBS spectra and then integrating the frequency shifts along the time axis.

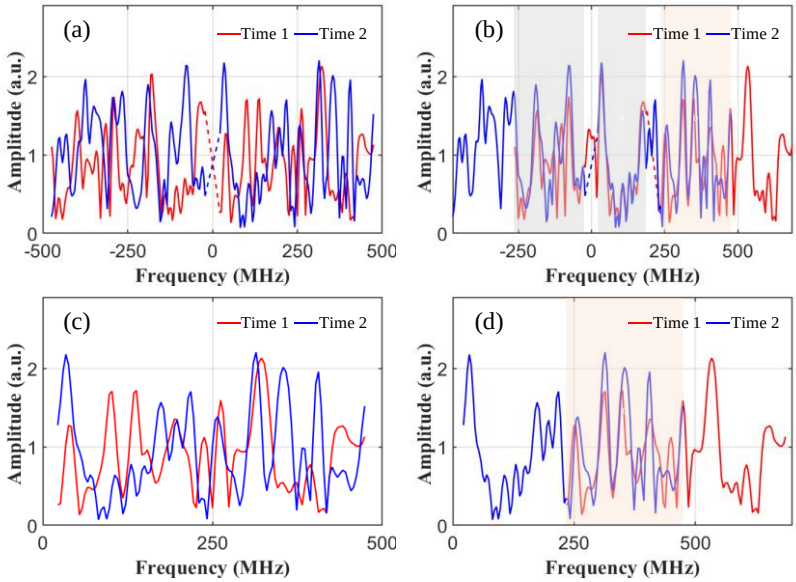

Figure 4-10 (a) The double-sideband frequency spectra two different times; (b) The frequency shifted double sideband spectra; (c) The positive sideband frequency spectra; (d) The frequency shifted positive sideband spectra.

Fig. 4-10 shows the frequency spectra of the same data in Fig. 4-9 (a) at 4.08 *ms* and 4.96 *ms*. Fig. 4-10 (a) shows the double sideband frequency spectra, where the 44 MHz missing frequency points are drawn with dashed lines. Fig. 4-10 (b) shows the double sideband frequency spectra after 222 MHz frequency shift. The gray and red shaded

areas are used to estimate the mean square error with the LMS algorithm. The unshaded areas with dashed lines are invalid areas that are discarded in the calculation process to avoid frequency shift estimation errors. Fig. 4-10 (c) shows the positive sideband in Fig. 4-10 (a), and Fig. 4-10 (d) displays the frequency-shifted positive sideband spectra. The red shaded area which is used to estimate frequency shift corresponds to the red shaded area in Fig. 4-10 (b). It can be seen from Fig. 4-10 (d) that the frequency shift reaches almost half of the spectrum range, in which circumstance the frequency shift is easily estimated incorrectly. But in Fig. 4-10 (b), the valid area is larger, and the frequency shift can be estimated more accurately.

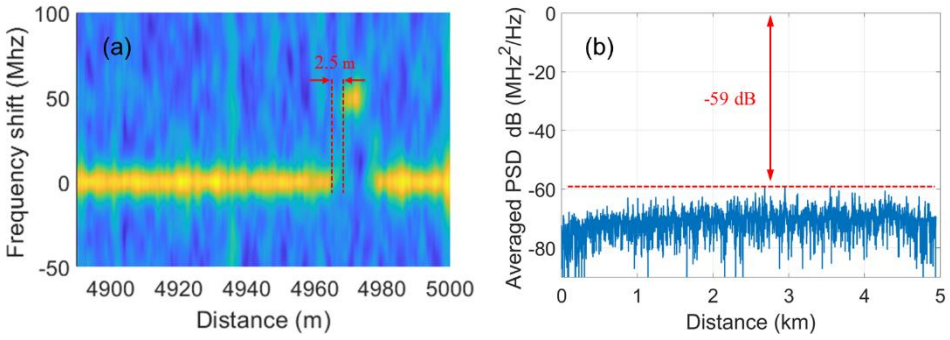

Figure 4-11 (a) Spatial resolution of the system; (b) Averaged power spectral density between 500 Hz and 3000 Hz along the fiber.

In the pulse compression scheme, the spatial resolution of the system is no longer restricted by the pulse width but determined by the bandwidth of matched filters. Therefore, long pulses can be used to improve the SNR of the signal. According to Eq. (2-67), a matched filter with 40 MHz bandwidth will lead to an SR of 2.5 m, as indicated in Fig. 4-11 (a). To evaluate the noise level of the system, the PSD along the fiber distance is calculated. As shown in Fig. 4-11 (b), the maximum averaged PSD between 500 Hz and 3 kHz is -59 dB, corresponding to a strain sensitivity of 7.5 $p\varepsilon/\sqrt{Hz}$. Compared with the phase demodulation scheme, interference and polarization fading free measurement is achieved over the entire FUT.

To further demonstrate the performance of double-sideband COTDR, complex waveforms are applied to the PZT. The pulse width and pulse period are set to be 10 μs and 150 μs respectively. Fig. 4-12 shows the measurement results of a chirped waveform (a-c) and a triangle waveform (d-f). The chirped waveform swept from 100 Hz to 1000 Hz with a duration of 20 ms and an amplitude of 2V. From the time-frequency map in Fig. 4-12 (c), we can see that the chirped waveform is well recovered. The frequency and amplitude of the triangle wave are 300 Hz and 2V respectively. The measurement result demonstrates the reliability of the system.

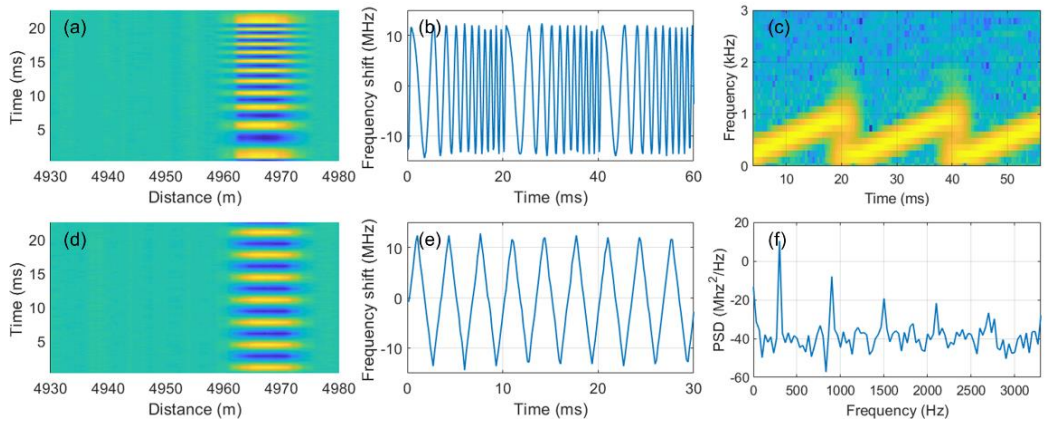

Figure 4-12 (a-c): Frequency shift, time-domain waveform, and time-frequency map of chirped wave; (d-f): Frequency shift, time-domain waveform, and frequency spectra of triangle wave.

It is noteworthy that the dual-sideband LFM scheme was introduced in COTDR to address the issue of phase drift noise in [134]. In this scheme, external disturbances are obtained directly through the cross-correlation of local RBS trace segments rather than first recovering the RBS spectrum using the SPEA and then cross-correlating the reference and measurement spectra. However, without implementing pulse compression, the constraint relationship between spatial resolution and pulse width cannot be overcome, which makes it challenging to achieve high spatial resolution and long sensing distance simultaneously in [134].

4.4 Summary

In this chapter, we propose a COTDR system based on dual-sideband LFM. This system is designed to fully utilize both the positive and negative frequency bands of the RBS spectrum, effectively doubling the dynamic range without necessitating an increase in the bandwidth of the electronic equipment within the system. By employing a dual-sideband LFM pulse with a 10 μs pulse width and a 498 MHz frequency sweep range, we have achieved fading-free distributed strain measurement over a 5 km single-mode fiber. The system's SR is 2.5 m, and it exhibits a strain sensitivity greater than 7.5 $p\varepsilon/\sqrt{Hz}$. The proposed scheme shows promise for application in the measurement of large vibration signals, offering a significant advancement in the field of optical fiber sensing.

5 Pressure Sensor with High-Sensitivity Based on Dual-Sideband Linear Frequency Modulated OFDR

5.1 Introduction

Pressure measurement is crucial in various fields, including oil and natural gas exploration, transportation, and pore water pressure monitoring in geotechnical structures, among others [76], [77] To meet the growing demands for pressure measurement, numerous studies have been carried out on pressure sensing techniques. OFS such as FBG, F-P cavity, and SPR [135], [136], [137], [138], [139] have been recognized as suitable candidates for pressure sensing due to their anti-electromagnetic interference, corrosion resistance, remote interrogation, and high robustness properties. For instance, the FBG can be securely attached to a structure that is easily deformed under pressure, like an elastic metal film [135] or a thin-walled cylinder [136], to facilitate pressure measurement. Using an elastic metal film and a thin-walled cylinder, pressure sensitivities of 23.8 pm/MPa and 69.4 pm/MPa were achieved, respectively. The FBG can also be inscribed on special fibers that are highly sensitive to pressure to enhance sensitivity. On a single-ring suspended fiber, the FBG achieved a pressure sensitivity of -43.6 pm/MPa [137]. Hydrostatic pressure sensors based on F-P cavity and hollow-core (HC) fibers were also proposed, with pressure sensitivities of -17.3 and -23.4 pm/MPa using a HC microstructured fiber and a HC photonic bandgap fiber, respectively [138]. However, these OFS can only provide single-point measurements, and distributed pressure profiles cannot be obtained.

To facilitate continuous pressure measurement, various DOFS have been developed. The BDG combined with a thin-diameter polarization-maintaining PCF was demonstrated as a

pressure sensor in 2016, achieving a sensitivity of 199 MHz/MPa with a measurement error of less than 0.03 MPa [78]. Due to the complexity of the BDG system, a simpler pressure sensor based on BOTDA was proposed in 2020, achieving a sensitivity of -3.61 MHz/MPa and a measurement error of 0.09 MPa with a double-layer polymer coating [79]. Despite the use of special optical fibers, the pressure sensitivities of Brillouin scattering-based DOFS remain limited. Pressure sensors based on Φ-OTDR have also been developed, exhibiting high sensitivities and measurement accuracies. For example, the Φ-OTDR combined with high birefringent PCF [80] or the elliptical core fiber with side air holes [81] achieved sensitivities of -2190 MHz/MPa and 1590 MHz/MPa, respectively. Although there was a significant improvement in pressure sensitivity compared to Brillouin scattering-based DOFS, dynamic pressure measurement was not reported. In 2022, Qiu et al. achieved dynamic pressure measurement with a 33.3 KHz sampling rate and a 2 m spatial resolution using Φ-OTDR and a standard SMF [82]. However, its sensitivity of 702.5 MHz/MPa is significantly lower than those achieved using special fiber.

This chapter introduces a highly-sensitive distributed dynamic pressure sensor based on a dual-linear frequency modulated optical frequency domain reflectometry and a coating thickness-enhanced SMF. A dual-sideband LFM signal is used to interrogate the sensing fiber, which allows us to obtain a dual-sideband Rayleigh backscattering signal. Due to the opposite slopes of the two LFM sidebands, the Rayleigh backscattering spectra of the two sidebands drift in opposite directions when the fiber is disturbed. By subtracting the frequency shifts of the two spectra, we can double the system's sensitivity. We further enhance the sensitivity by using an SMF with a coating thickness of 200 μm. This results in a pressure sensitivity of 3979 MHz/MPa, a measurement accuracy of 0.97 KPa, and a spatial resolution of 35 cm over a 500 m optical fiber. Our system successfully

detected a dynamic pressure change at a sampling rate of 1.25 KHz, demonstrating the sensor's excellent dynamic measuring capabilities.

5.2 Principle

5.2.1 Principle of dual-sideband linear frequency modulated OFDR

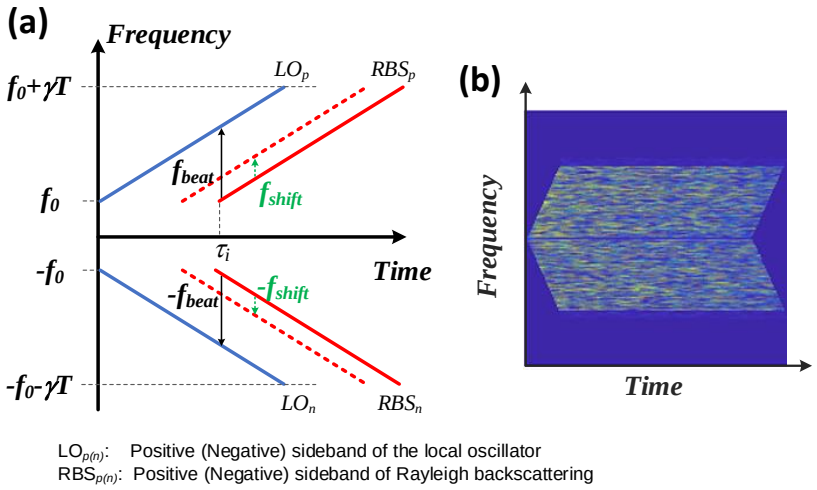

Figure 5-1: Principle of dual-sideband-modulated OFDR. (a) The time-frequency relationship between the LO and RBS based on dual-sideband modulation; (b) The time-frequency map of the beat signal.

Fig. 5-1 illustrates the principle of the dual sideband modulated OFDR. The frequency and amplitude of the laser source are f_c and A_L, and the starting frequencies and slopes of the dual-sideband LFM signal are $\pm f_0$ and $\pm\gamma$, respectively. The LO can be expressed as:

$$E_{LO} = A_L\left[\exp\left\{j(2\pi f_c t - 2\pi f_0 t - \pi\gamma t^2)\right\} + \exp\left\{j\left(2\pi f_c t + 2\pi f_0 t + \pi\gamma t^2\right)\right\}\right] \tag{5-1}$$

The RBS generated in fiber can be expressed as:

$$E_{RBS} = \sum_i a_i\left[\exp\left\{j\left(2\pi f_c\left(t-\tau_i\right) - 2\pi f_0\left(t-\tau_i\right) - \pi\gamma\left(t-\tau_i\right)^2\right)\right\} + \exp\left\{j\left(2\pi f_c\left(t-\tau_i\right) + 2\pi f_0\left(t-\tau_i\right) + \pi\gamma\left(t-\tau_i\right)^2\right)\right\}\right] \tag{5-2}$$

where a_i is the reflective amplitude of the scattering points, τ_i is the time delay of scattering points. For simplicity, the fiber attenuation is neglected here. So, the beat signal between the LO and the RBS I_{beat} can be expressed as:

$$\begin{aligned} I_{beat} &\propto E_{LO}(t)\cdot E_{RBS}^{*}(t) \\ &= R_{PD}A_L\sum_i a_i\Big[\exp\left\{j\left(2\pi f_c\tau_i - 2\pi f_0\tau + \pi\gamma\tau_i^{\,2} - 2\pi\gamma\tau_i t\right)\right\} \\ &\quad + \exp\left\{j\left(2\pi f_c\tau_i + 2\pi f_0\tau_i - \pi\gamma\tau_i^{\,2} + 2\pi\gamma\tau_i t\right)\right\}\Big] \end{aligned} \tag{5-3}$$

where R_{PD} is the responsivity of the PD. Note that only the beat frequency between LO_p and RBS_p, as well as the beat frequency between LO_n and RBS_n need to be considered. The unwanted beat signals between the positive sideband and the negative sideband can be set beyond the PD bandwidth by reasonably setting the frequency f_0 and the LFM bandwidth. From Eq. (5-3), we can find that two opposite beat frequencies are generated. When the fiber is disturbed by pressure, the time delay between LO and RBS changes, causing frequency shifts in the two frequency sidebands. The green arrows in Fig. 5-1 (a) depict the opposite changes in beat frequencies caused by the pressure. Fig. 5-1 (b) demonstrates the time-frequency distribution of the beat signal of dual-sideband OFDR. Since the frequency ranges of the two sidebands are different, the information contained in the two frequency spectra is different, too. Therefore, by calculating the positive and negative sideband frequency shifts separately and subtracting them, the sensitivity of the system can be increased to 2 times.

5.2.2 Pressure-induced strain on optical fibers

When the fiber is under pressure, axial and radial strains are generated in the fiber, therefore causing a phase change of light. The frequency shift caused by pressure can be written as [140], [141]:

$$\frac{\Delta v}{v} = \varepsilon_z - \frac{n^2}{2}\left[2\varepsilon_r\left(p_{11} - p_{44}\right) + \varepsilon_z\left(p_{11} - 2p_{44}\right)\right] \tag{5-4}$$

where p_{11} and p_{44} are the elasto-optic coefficients of silica glass fiber, and n is the RI of fiber. ε_z and ε_r are the axial and radial strains, which are given by:

$$\varepsilon_z \approx -\frac{1-2(1-f)v_p - 2fv_g}{fE_g + (1-f)E_p}\, p \tag{5-5}$$

$$\varepsilon_r \approx \left[\frac{v_g\left(1-2v_p\right) - f\left(1-v_g-2v_g v_p\right)}{fE_g + (1-f)E_p} - \frac{\left(1+v_g\right)\left(1-2v_g\right)(1-f)E_p/E_g}{fE_g + (1-f)E_p}\right] p \tag{5-6}$$

Representing the radius of fiber and polymer coating by a and b, we define $f = (a/b)^2$, which normally satisfies $f \ll 1$. p is the pressure. v_g, v_p denote the Poisson's ratios of glass fiber and polymer coating. E_g, E_p represent Young's modulus of glass fiber and polymer coating, respectively. According to Eq. (5-4), we simulated the pressure sensitivities in the case of different E_p and v_p. Taking p_{11}=0.1254, p_{44}=-0.0718, n=1.51, v_g =0.17, E_g = 73 GPa, p=1 MPa, a=62.5 μm, the simulation results of pressure sensitivities $\Delta v_{Coating}/\Delta v_{Uncoating}$ are demonstrated in Fig. 5-2, where $\Delta v_{Coating}$ and $\Delta v_{Uncoating}$ stand for the frequency shift of a coating fiber and an uncoating fiber, respectively. An increase in coating radius will increase pressure sensitivity. For the same coating radius, using coating materials with smaller E_p and v_p will result in higher pressure sensitivity. According to our calculation, the axial strain ε_z in Eq. (5-5) is negative when positive pressure is applied, proving that the silica glass fiber will contract in the axial direction along with the polymer coating. Our experiment adopted an optical fiber with a coating radius of 200 μm (YOFC PM 1550_125-13/400). Compared with

a standard SMF with a coating radius of 125 μm, the sensitivity can be increased by 2.19 times, 2.48 times, and 2.56 times in the three cases in Fig. 5-2.

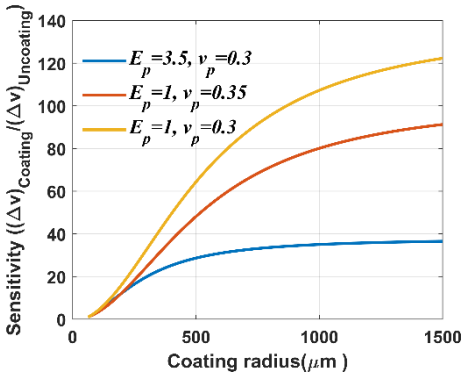

Figure 5-2: Pressure sensitivities $\Delta\nu_{Coating}/\Delta\nu_{Uncoating}$ in case of different coating Young's Modulus E_p and coating Poisson's ratios ν_p.

5.3 Experiments

5.3.1 System configuration

As shown in Fig. 5-3, an NLL light source operating at 1550 nm is injected into an electro-optic intensity modulator and modulated into a dual-sideband LFM pulse signal. The AWG is used to generate the LFM signal. EDFA1 and a BPF are used to amplify the power and remove the ASE noise, respectively. Then the light is split into two branches in a 90:10 ratio. The 10% serves as the LO, and the probe pulse is launched into the FUT with a length of 500 m through the circulator. Later, the Rayleigh-backscattering light from the FUT is amplified by EDFA2, whose ASE noise is suppressed by another band-pass filter. Finally, an optical hybrid recombines the LO and RBS signal, and the I and Q components in the *x* polarization state are detected by two 500 MHz bandwidth PD. The PC controls the polarization state of LO and makes the optical power detected by the PD maximized. The electrical signal output by PD is collected by the oscilloscope with a 1 GSa/s sampling rate.

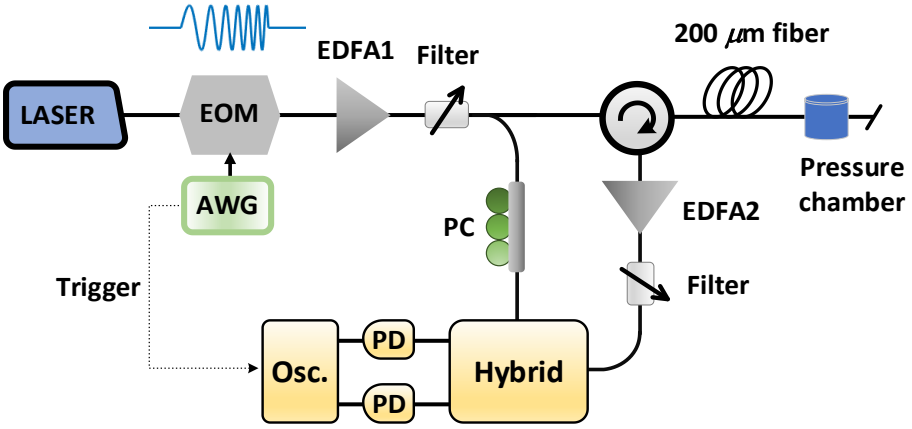

Figure 5-3: Experimental setup for high-sensitivity pressure measurement.

5.3.2 Pressure measurement results

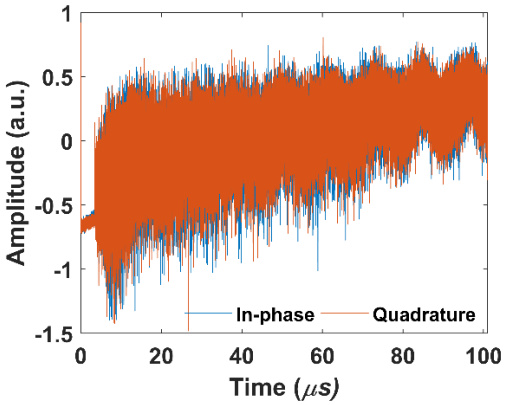

Figure 5-4: The detected in-phase and quadrature RBS signal.

In our experiments, the pulse width of the LFM signal is set to be 100 μs and the frequency scans from 500 MHz to 4 GHz, yielding a slope of 3.5×10^{13} Hz/s. As the length of FUT is 500 m, the maximum beat frequency between the RBS and the LO is calculated to be 175 MHz. Fig. 5-4 shows the detected complex RBS signal. A short-time Fourier transform (STFT) with an 8.192 μs Hamming window and a sliding step of 1.024 μs is applied to the detected signals, resulting in a 35 cm spatial resolution. Fig. 5-5 shows the demodulated RBS spectra. The pattern of the positive sideband is different from that of the negative sideband, which indicates that we can improve the sensitivity by synthesizing the frequency shifts of two sidebands.

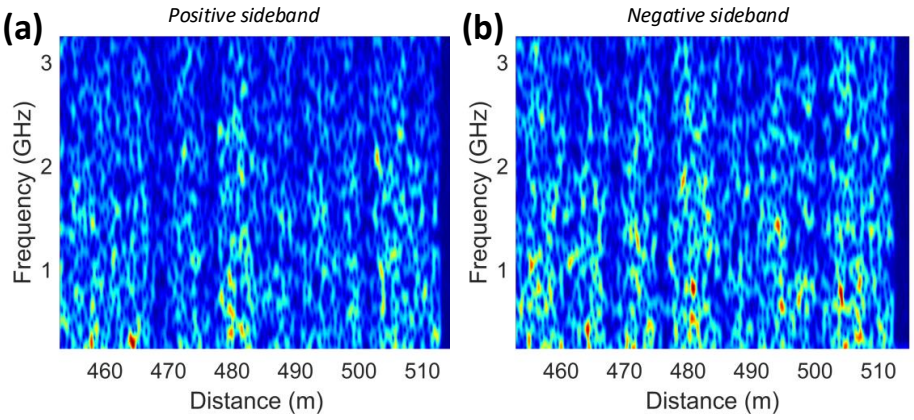

Figure 5-5: The measured RBS spectra along the sensing fiber for (a) the positive sideband and (b) the negative sideband.

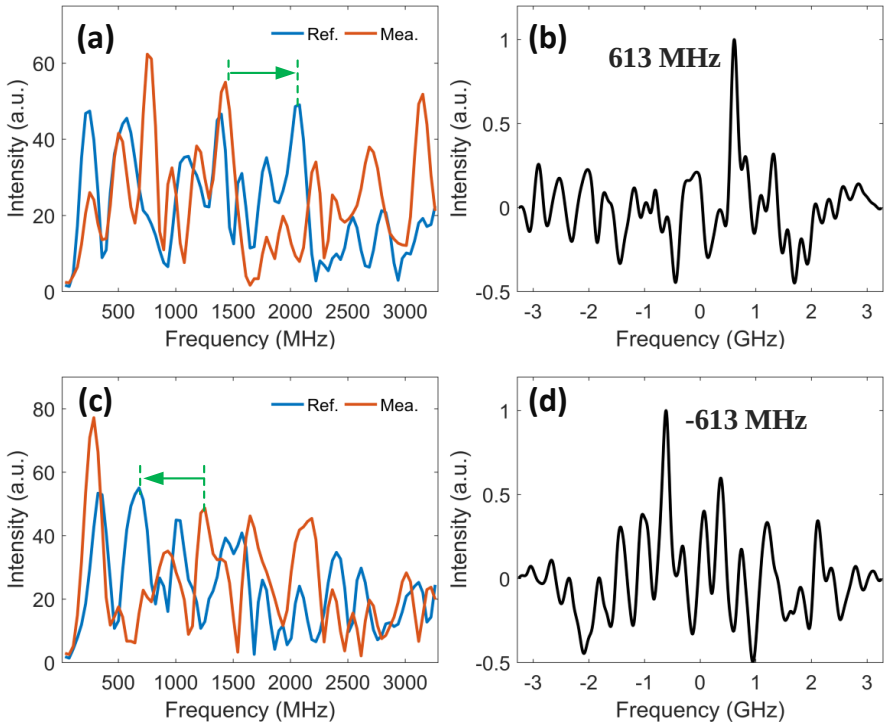

Figure 5-6: (a) The positive sideband of frequency spectra under 0.312 MPa pressure change and (b) their cross-correlation; (c) The negative sideband of frequency spectra under 0.312 MPa pressure change and (b) their cross-correlation.

To realize the pressure measurement, the SMF with a 200 μm coating radius is placed in an oil pressure chamber. Fig. 5-6 shows the measurement results of a 0.312 MPa pressure change. Fig. 5-6 (a) presents the positive sidebands of the reference spectrum at 0 MPa and the measured spectrum at 0.312 MPa. The patterns of the two spectra look similar but a frequency

shift exists between them. Fig. 5-6 (b) shows the frequency shift acquired by cross-correlating the two spectra, which is 613 MHz. The negative sideband frequency spectra and their cross-correlation result are shown in Fig. 5-6 (c) and Fig. 5-6 (d), respectively. We can find that the frequency shifts of the two sidebands are the same in magnitude but opposite in sign, which is consistent with our analysis as indicated in Fig. 5-1.

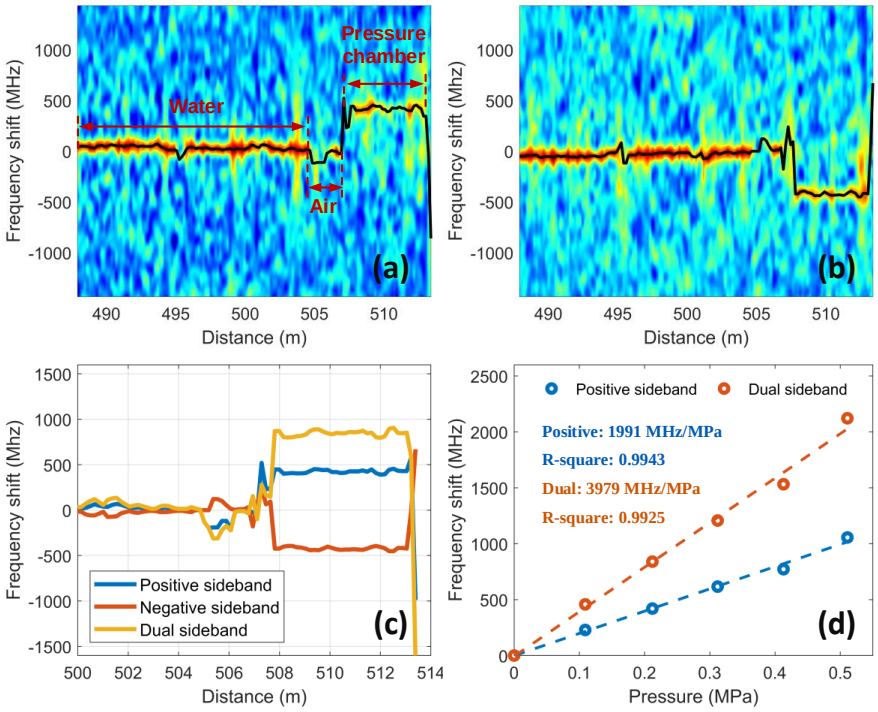

Figure 5-7: The pressure distributions of (a) the positive sideband and (b) the negative sideband; (c) The frequency shift comparison between the single sideband and dual sideband; (d) The sensitivities of the sensor.

Fig. 5-7 demonstrates the distributed measurement ability of the system and the pressure sensitivity measurement result. The pressure change is 0.212 MPa in Fig. 5-7 (a-c). The fiber length in the pressure chamber is about 5 m. Average frequency shifts of 422 MHz and -420 MHz are obtained from Fig. 5-7 (a) and (b). In Fig. 5-7 (c), a subtraction between the two sidebands is performed and an average frequency shift of 840 MHz is acquired. To obtain the pressure sensitivity of the proposed scheme, we measured the pressure from 0.11 MPa to 0.51 MPa at an interval of 0.1 MPa, and Fig. 5-7 (d) shows the frequency shift results. The dash lines

are linear fitting curves to dots. We can see that the pressure sensitivities are 1991 MHz/MPa for single-sideband demodulation and 3979 MHz/MPa for dual-sideband demodulation. The linearities are good, which reached 99.4% and 99.3%, respectively.

To assess the measurement precision of our scheme, we calculated the SD of the dual-sideband frequency shift at various fiber locations. To mitigate the impact of environmental disturbances such as temperature fluctuations, we selected a region with a minimal frequency shift, ranging from 442 m to 466 m, for the SD calculation. The measurement accuracy obtained was 3.87 MHz, corresponding to a pressure measurement accuracy of 0.97 KPa.

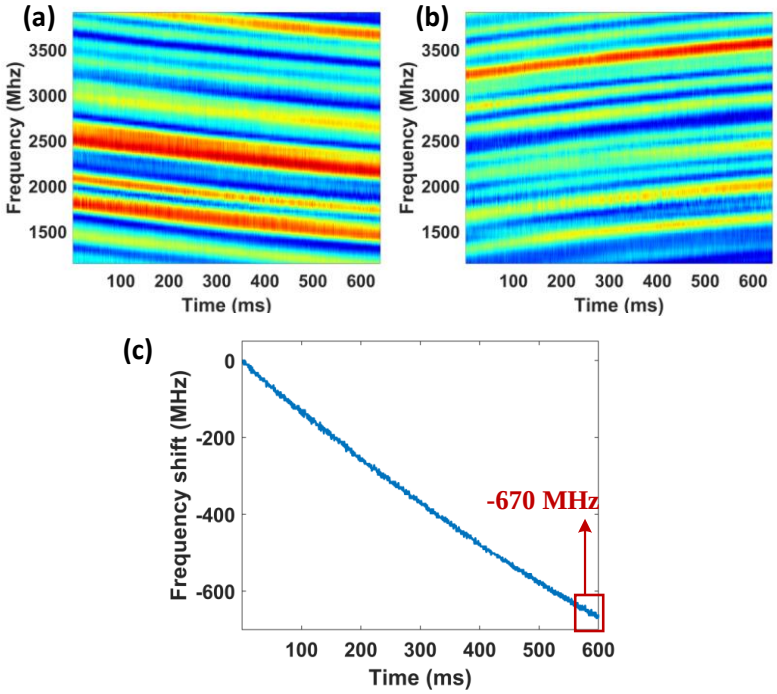

Figure 5-8: The temporal frequency spectral evolution of (a) the positive sideband and (b) the negative sideband under pressure change; (c) Frequency shift as a function of time under dynamic pressure.

Finally, the dynamic pressure sensing ability is verified experimentally. The pressure of the oil pressure chamber is increased to a certain level in advance, then the air valve is opened, and the pressure-releasing process is recorded. The sampling interval is set to be 800 μs, leading to a 1.25 KHz sampling rate to the dynamic pressure change. The temporal evolutions of the

positive and negative sideband frequency spectra are shown in Fig. 5-8 (a) and (b). And Fig. 5-8 (c) demonstrates the subtracted frequency shifts of the two sidebands. We can see that the frequency shift gradually increases negatively with time, leading to a total frequency shift of -670 MHz in a 600 ms time scale. The result shows that the system has a good dynamic measurement capability.

5.4 Summary

In summary, we have proposed and experimentally validated a dynamic distributed pressure sensor, leveraging a dual-sideband modulated OFDR and a coating thickness-enhanced SMF. The strain induced by pressure results in opposing frequency shifts in the positive and negative frequency spectrum sidebands of the Rayleigh scattering signal, thereby doubling the sensor's sensitivity. The pressure sensitivity was theoretically analyzed and simulated, confirming that the pressure sensitivity can be significantly amplified by increasing the fiber coating's thickness. We utilized an SMF with a 200 μm coating radius to measure the pressure with the OFDR. Over a 500 m fiber length, we achieved a pressure sensitivity of 3979 MHz/MPa and a measurement accuracy of 0.97 KPa, with a spatial resolution of 35 cm. Furthermore, we conducted a dynamic pressure measurement with a sampling rate of 1.25 KHz. Within 600 ms, a 670 MHz frequency shift was accurately detected. The proposed sensor demonstrated high-pressure sensitivity, superior accuracy, high SR, and rapid frequency response, offering a potential solution for application scenarios necessitating high-performance pressure measurements.

6 Summary and Outlook

6.1 Summary

DOFS technology, which exploits Rayleigh scattering, is renowned for its high sensitivity, capability for single-ended measurements, non-intrusive nature, and remote sensing potential. These attributes render it exceedingly valuable for applications in industrial production, intelligent transportation systems, security surveillance, and environmental monitoring. Currently, with a plethora of interrogation, demodulation, and performance enhancement strategies at hand, DOFS technology predicated on Rayleigh scattering has reached a mature stage of development. DOFS that rely on Rayleigh spectrum demodulation are inherently resistant to interference and polarization fading, and they are capable of measuring both dynamic and static parameters, which positions them as a particularly reliable demodulation technique. In response to the ever-evolving demands of practical measurement applications, this thesis undertakes a comprehensive investigation into DOFS based on Rayleigh spectrum demodulation. The research extends beyond the conventional sensing of temperature, strain, and vibration to explore the detection of other physical parameters and to seek performance enhancements. The principal contributions of this thesis are as follows:

1. A distributed salinity sensor featuring high sensitivity was developed, utilizing frequency scanning Φ-OTDR technology. This approach diverges from conventional DOFS methodologies that typically rely on standard SMF, which exhibits minimal sensitivity to salinity changes. Instead, our design incorporates a polyimide-coated SMF, significantly enhancing salinity sensitivity. The proposed

sensor achieved a remarkable salinity sensitivity of 782.4 MHz/(mol/L) over an 1100 m fiber length with an SR of 1 m, validating the efficacy of our approach. Additionally, the measurement accuracy of the cross-correlation frequency shift estimator was rigorously analyzed using CRLB and tested across various pulse widths. The results indicated measurement uncertainties of 0.022 mol/L (equivalent to a frequency uncertainty of 17.6 MHz) for a 3 ns pulse width and 0.005 mol/L (corresponding to a frequency uncertainty of 3.7 MHz) for a 20 ns pulse width.

2. To address the issue of cross-sensitivity between salinity and temperature, further research was conducted using a bow-tie PMF sensor to decouple these two parameters. The sensitivity coefficients for temperature and salinity along the fast and slow axes of the PMF were calibrated independently. Subsequent simultaneous measurement experiments successfully demodulated the distributed salinity and temperature profiles along the fiber, achieving measurement accuracies of 0.0344 K for temperature and 0.0469 mol/L for salinity, respectively.
3. With the objective of maximizing the utilization of frequency spectrum resources and enhancing the dynamic range, we introduced a dual-sideband LFM COTDR system based on SPEA. This method effectively doubles the dynamic range without necessitating an increase in the bandwidth of electronic devices, compared to the single-sideband modulation approach. In our experimental setup, we successfully measured a maximum frequency shift of 461 MHz using an LFM signal with a frequency sweep range of 498 MHz, a feat unattainable with single-sideband modulation.
4. We proposed a high-sensitivity pressure sensor employing OFDR. The implementation of dual-sideband modulation creates two opposing frequency

shifts in the sidebands, which, when subtracted from one another, enhance the overall sensitivity of the sensor. Theoretical analysis guided the choice of using SMF with a coating thickness of 200 μm to further increase the sensor's sensitivity. The culmination of these design choices led to the achievement of a pressure sensitivity of 3979 MHz/MPa, a measurement accuracy of 0.97 KPa, and an SR of 35 cm on a 500 m sensing fiber.

We have conducted a comprehensive comparison of the various sensing schemes proposed, as well as contrasting them with other contemporary state-of-the-art distributed sensing technologies. The performance characteristics of each sensing scheme have been succinctly summarized in Table 6.1 for ease of evaluation and reference.

Table 6.1 Comparison of distributed optical fiber sensors based on RBS

	Frequency-scanning Φ-OTDR (Chapter 3)	**Dual-sideband modulated COTDR (Chapter 4)**	**Dual-sideband modulated OFDR (Chapter 5)**	**Φ-OTDR with digital coherent detection [26]**	**Direct detection chirped pulse Φ-OTDR [44]**
Dynamic range	14 GHz (46 $u\varepsilon$)	1 GHz (3.09 $u\varepsilon$)	3.5 GHz (~11.5 $u\varepsilon$)	π rad (0.72 $u\varepsilon$/m)	Several GHz
Spatial resolution	2 m	2.5 m	35 cm	2.6 m	10 m
Frequency response	-	6.66 KHz @ 5 km fiber	1.25 KHz @ 0.5 km fiber	$c/2nL$	KHz @ 1 km fiber
Strain resolution	6.8 nε	1.4 nε	26 nε	Not available	4 nε
Fading	Immune	Immune	Immune	Not immune	Immune

The table presented above clearly illustrates that each sensing scheme possesses

unique advantages and disadvantages. The frequency-scanning Φ-OTDR stands out for its high dynamic range, yet it is limited to static parameter measurements only. Among the various sensing schemes, the dual-sideband LFM COTDR demonstrates a robust performance, with each of its performance parameters reaching satisfactory levels. On the other hand, OFDR distinguishes itself with its exceptional spatial resolution. When it comes to practical applications, the selection of a particular scheme should be guided by the specific requirements and needs at hand.

6.2 Outlook

Looking ahead, there is considerable scope for research and enhancement in the field of DOFS based on Rayleigh spectral demodulation. Future investigations could concentrate on the following areas:

1. In the practical deployment of salinity and pressure measurement applications, the encapsulation and protection of optical fibers are critical to ensure their longevity and reliability. However, this protective process can adversely affect the sensitivity of the fibers. It is, therefore, imperative to rigorously test the practical viability of the proposed sensing schemes. For salinity sensing in particular, there is a need for comprehensive studies to ascertain the long-term stability of the hygroscopic properties of polyimide coatings.
2. As discussed in Chapter 4, while the dynamic range of Φ-OTDR has been expanded using dual-sideband LFM, it still falls short when compared to other methodologies, such as those based on Brillouin scattering sensors. To further extend the dynamic range, one could consider utilizing PMF as the sensing

medium and concurrently measure its birefringence and Rayleigh spectra. The birefringence spectrum, derived from cross-correlating the Rayleigh spectra of the fast and slow axes, exhibits significantly lower strain coefficients than the Rayleigh spectrum [132]. This implies that within the same frequency sweep range of the LFM, the birefringence spectrum can accommodate a wider strain range than the Rayleigh spectrum. When strain-induced frequency shifts exceed the Rayleigh spectrum's capacity, the birefringence spectrum's frequency shift can be employed for strain demodulation. Conversely, when the strain is too subtle to be detected by the birefringence spectrum, the Rayleigh spectrum can provide the necessary strain information. By leveraging the properties of PMF, a substantial enhancement in dynamic range could be achieved.

References

[1] A. Sladen *et al.*, "Distributed sensing of earthquakes and ocean-solid Earth interactions on seafloor telecom cables," *Nature communications*, vol. 10, no. 1, p. 5777, 2019.

[2] G. A. Wellbrock *et al.*, "First field trial of sensing vehicle speed, density, and road conditions by using fiber carrying high speed data," in *2019 Optical Fiber Communications Conference and Exhibition (OFC)*, IEEE, 2019, pp. 1–3.

[3] Y. Aono, E. Ip, and P. Ji, "More than communications: environment monitoring using existing optical fiber network infrastructure," in *Optical Fiber Communication Conference*, Optica Publishing Group, 2020, pp. W3G-1.

[4] R. Tennyson, A. Mufti, S. Rizkalla, G. Tadros, and B. Benmokrane, "Structural health monitoring of innovative bridges in Canada with fiber optic sensors," *Smart materials and Structures*, vol. 10, no. 3, p. 560, 2001.

[5] X. Bao, C. Zhang, W. Li, M. Eisa, S. El-Gamal, and B. Benmokrane, "Monitoring the distributed impact wave on a concrete slab due to the traffic based on polarization dependence on stimulated Brillouin scattering," *Smart materials and structures*, vol. 17, no. 1, p. 015003, 2007.

[6] X. Fan, G. Yang, S. Wang, Q. Liu, and Z. He, "Distributed fiber-optic vibration sensing based on phase extraction from optical reflectometry," *Journal of Lightwave Technology*, vol. 35, no. 16, pp. 3281–3288, 2016.

[7] H. Zheng *et al.*, "Distributed vibration measurement based on a coherent multi-slope-assisted BOTDA with a large dynamic range," *Optics letters*, vol. 44, no. 5, pp. 1245–1248, 2019.

[8] H. Zheng, Y. Yan, Y. Wang, X. Shen, and C. Lu, "Deep learning enhanced long-range fast BOTDA for vibration measurement," *Journal of lightwave technology*, vol. 40, no. 1, pp. 262–268, 2021.

[9] X. Zhou *et al.*, "Chaos Raman optical time-domain reflectometry for millimeter-

level spatial resolution temperature sensing," *Journal of Lightwave Technology*, vol. 39, no. 23, pp. 7529–7538, 2021.

[10] K. Kikuchi, T. Naito, and T. Okoshi, "Measurement of Raman scattering in single-mode optical fiber by optical time-domain reflectometry," *IEEE journal of quantum electronics*, vol. 24, no. 10, pp. 1973–1975, 1988.

[11] M. Barnoski and S. Jensen, "Fiber waveguides: a novel technique for investigating attenuation characteristics," *Applied optics*, vol. 15, no. 9, pp. 2112–2115, 1976.

[12] R. Juškaitis, A. Mamedov, V. Potapov, and S. Shatalin, "Interferometry with Rayleigh backscattering in a single-mode optical fiber," *Optics letters*, vol. 19, no. 3, pp. 225–227, 1994.

[13] J. C. Juarez and H. F. Taylor, "Field test of a distributed fiber-optic intrusion sensor system for long perimeters," *Applied optics*, vol. 46, no. 11, pp. 1968–1971, 2007.

[14] Y. Lu, T. Zhu, L. Chen, and X. Bao, "Distributed vibration sensor based on coherent detection of phase-OTDR," *Journal of lightwave Technology*, vol. 28, no. 22, pp. 3243–3249, 2010.

[15] H. F. Martins, S. Martín-López, P. Corredera, M. L. Filograno, O. Frazao, and M. Gonzalez-Herráez, "Phase-sensitive optical time domain reflectometer assisted by first-order Raman amplification for distributed vibration sensing over> 100 km," *Journal of Lightwave Technology*, vol. 32, no. 8, pp. 1510–1518, 2014.

[16] Z. Wang *et al.*, "Ultra-long phase-sensitive OTDR with hybrid distributed amplification," *Optics letters*, vol. 39, no. 20, pp. 5866–5869, 2014.

[17] R. Posey Jr, G. Johnson, and S. Vohra, "Strain sensing based on coherent Rayleigh scattering in an optical fibre," *Electronics Letters*, vol. 36, no. 20, p. 1, 2000.

[18] A. Masoudi, M. Belal, and T. Newson, "A distributed optical fibre dynamic strain sensor based on phase-OTDR," *Measurement Science and Technology*, vol. 24, no. 8, p. 085204, 2013.

[19] A. Masoudi and T. P. Newson, "High spatial resolution distributed optical fiber

dynamic strain sensor with enhanced frequency and strain resolution," *Optics Letters*, vol. 42, no. 2, pp. 290–293, 2017.

[20] A. Masoudi and T. P. Newson, "Analysis of distributed optical fibre acoustic sensors through numerical modelling," *Optics express*, vol. 25, no. 25, pp. 32021–32040, 2017.

[21] G. Fang, T. Xu, S. Feng, and F. Li, "Phase-sensitive optical time domain reflectometer based on phase-generated carrier algorithm," *Journal of lightwave technology*, vol. 33, no. 13, pp. 2811–2816, 2015.

[22] A. Alekseev, V. Vdovenko, B. Gorshkov, V. Potapov, and D. Simikin, "A phase-sensitive optical time-domain reflectometer with dual-pulse phase modulated probe signal," *Laser Physics*, vol. 24, no. 11, p. 115106, 2014.

[23] A. Alekseev, V. Vdovenko, B. Gorshkov, V. Potapov, and D. Simikin, "A phase-sensitive optical time-domain reflectometer with dual-pulse diverse frequency probe signal," *Laser Physics*, vol. 25, no. 6, p. 065101, 2015.

[24] J. P. Dakin and C. Lamb, "Distributed fibre optic sensor system," GB2222247A, Feb. 28, 1990 Accessed: Jan. 08, 2024. [Online]. Available: https://patents.google.com/patent/GB2222247A/en?oq=GB2222247A

[25] X. He *et al.*, "Multi-event waveform-retrieved distributed optical fiber acoustic sensor using dual-pulse heterodyne phase-sensitive OTDR," *Optics letters*, vol. 42, no. 3, pp. 442–445, 2017.

[26] Z. Pan, K. Liang, Q. Ye, H. Cai, R. Qu, and Z. Fang, "Phase-sensitive OTDR system based on digital coherent detection," in *2011 Asia Communications and Photonics Conference and Exhibition (ACP)*, IEEE, 2011, pp. 1–6.

[27] Z. Wang *et al.*, "Coherent Φ-OTDR based on I/Q demodulation and homodyne detection," *Optics express*, vol. 24, no. 2, pp. 853–858, 2016.

[28] W. Zou, S. Yang, X. Long, and J. Chen, "Optical pulse compression reflectometry: proposal and proof-of-concept experiment," *Optics express*, vol. 23, no. 1, pp. 512–522, 2015.

[29] S. Wang, X. Fan, Q. Liu, and Z. He, "Distributed fiber-optic vibration sensing based on phase extraction from time-gated digital OFDR," *Optics Express*, vol.

23, no. 26, pp. 33301–33309, 2015.

[30] D. Chen, Q. Liu, X. Fan, and Z. He, "Distributed fiber-optic acoustic sensor with enhanced response bandwidth and high signal-to-noise ratio," *Journal of Lightwave Technology*, vol. 35, no. 10, pp. 2037–2043, 2017.

[31] J. Jiang, Z. Wang, Z. Wang, Z. Qiu, C. Liu, and Y. Rao, "Continuous chirped-wave phase-sensitive optical time domain reflectometry," *Optics Letters*, vol. 46, no. 3, pp. 685–688, 2021.

[32] K. Shimizu, T. Horiguchi, and Y. Koyamada, "Characteristics and reduction of coherent fading noise in Rayleigh backscattering measurement for optical fibers and components," *Journal of Lightwave Technology*, vol. 10, no. 7, pp. 982–987, 1992.

[33] J. Zhou, Z. Pan, Q. Ye, H. Cai, R. Qu, and Z. Fang, "Characteristics and explanations of interference fading of a ϕ-OTDR with a multi-frequency source," *Journal of lightwave technology*, vol. 31, no. 17, pp. 2947–2954, 2013.

[34] D. Chen, Q. Liu, and Z. He, "Phase-detection distributed fiber-optic vibration sensor without fading-noise based on time-gated digital OFDR," *Optics express*, vol. 25, no. 7, pp. 8315–8325, 2017.

[35] D. Chen, Q. Liu, and Z. He, "High-fidelity distributed fiber-optic acoustic sensor with fading noise suppressed and sub-meter spatial resolution," *Optics Express*, vol. 26, no. 13, pp. 16138–16146, 2018.

[36] Z. Zhao *et al.*, "Interference fading suppression in φ-OTDR using space-division multiplexed probes," *Optics Express*, vol. 29, no. 10, pp. 15452–15462, 2021.

[37] F. Peng, X. Zheng, and Q. Miao, "Large Dynamic Range and Anti-Fading Phase-Sensitive OTDR Using 2D Phase Unwrapping Via Neural Network," *IEEE Transactions on Instrumentation and Measurement*, 2023.

[38] F. Cunzheng *et al.*, "Large dynamic range optical fiber distributed acoustic sensing (DAS) with differential-unwrapping-integral algorithm," *Journal of Lightwave Technology*, vol. 39, no. 22, pp. 7274–7280, 2021.

[39] Y. Bai, T. Lin, Z. Zhong, and Y. Wu, "Phase Unwrapping Method of Φ-OTDR System Based on Recursive-Branch-Cut Algorithm," *IEEE Sensors Journal*,

2023.

[40] H. He, L. Yan, H. Qian, X. Zhang, B. Luo, and W. Pan, “Enhanced range of the dynamic strain measurement in phase-sensitive OTDR with tunable sensitivity,” *Optics express*, vol. 28, no. 1, pp. 226–237, 2020.

[41] L. Zhang *et al.*, “Distributed and dynamic strain sensing with high spatial resolution and large measurable strain range,” *Optics Letters*, vol. 45, no. 18, pp. 5020–5023, 2020.

[42] Y. Koyamada, M. Imahama, K. Kubota, and K. Hogari, “Fiber-optic distributed strain and temperature sensing with very high measurand resolution over long range using coherent OTDR,” *Journal of Lightwave Technology*, vol. 27, no. 9, pp. 1142–1146, 2009.

[43] S. Liehr, S. Münzenberger, and K. Krebber, “Wavelength-scanning coherent OTDR for dynamic high strain resolution sensing,” *Optics express*, vol. 26, no. 8, pp. 10573–10588, 2018.

[44] J. Pastor-Graells, H. Martins, A. Garcia-Ruiz, S. Martin-Lopez, and M. Gonzalez-Herraez, “Single-shot distributed temperature and strain tracking using direct detection phase-sensitive OTDR with chirped pulses,” *Optics express*, vol. 24, no. 12, pp. 13121–13133, 2016.

[45] L. Costa, H. F. Martins, S. Martín-López, M. R. Fernández-Ruiz, and M. González-Herráez, “Fully distributed optical fiber strain sensor with 10- 12 $\epsilon/\sqrt{\text{Hz}}$ sensitivity,” *Journal of Lightwave Technology*, vol. 37, no. 18, pp. 4487–4495, 2019.

[46] J. Xiong, Z. Wang, Y. Wu, and Y. Rao, “Single-shot COTDR using sub-chirped-pulse extraction algorithm for distributed strain sensing,” *Journal of Lightwave Technology*, vol. 38, no. 7, pp. 2028–2036, 2020.

[47] J. Yang *et al.*, “Noise Compensation Methods for Optical Fiber Frequency Sweeping Interferometry: A Review,” *Journal of Lightwave Technology*, 2022.

[48] W. Eickhoff and R. Ulrich, “Optical frequency domain reflectometry in single-mode fiber,” *Applied Physics Letters*, vol. 39, no. 9, pp. 693–695, 1981.

[49] Z. Guo, J. Yan, G. Han, Y. Yu, D. Greenwood, and J. Marco, “High-resolution Φ-

OFDR using phase unwrap and nonlinearity suppression," *Journal of Lightwave Technology*, 2023.

[50] C. Zhang, Y. Bao, T. Cui, L. Tian, and J. Pan, "Polarization Independent Phase-OFDR in Rayleigh-Based Distributed Sensing," *Journal of Lightwave Technology*, vol. 41, no. 8, pp. 2518–2525, 2023.

[51] Y. Meng *et al.*, "Submillimeter-spatial-resolution φ-OFDR strain sensor using femtosecond laser induced permanent scatters," *Optics Letters*, vol. 47, no. 23, pp. 6289–6292, 2022.

[52] S. Zhao, J. Cui, Z. Wu, Z. Wang, and J. Tan, "Distributed fiber deformation measurement by high-accuracy phase detection in OFDR scheme," *Journal of Lightwave Technology*, vol. 39, no. 12, pp. 4101–4108, 2021.

[53] J. Li *et al.*, "High spatial resolution distributed fiber strain sensor based on phase-OFDR," *Optics express*, vol. 25, no. 22, pp. 27913–27922, 2017.

[54] C. Wang *et al.*, "High sensitivity distributed static strain sensing based on differential relative phase in optical frequency domain reflectometry," *Journal of Lightwave Technology*, vol. 38, no. 20, pp. 5825–5836, 2020.

[55] J. Cui, S. Zhao, D. Yang, and Z. Ding, "Investigation of the interpolation method to improve the distributed strain measurement accuracy in optical frequency domain reflectometry systems," *Applied optics*, vol. 57, no. 6, pp. 1424–1431, 2018.

[56] M. Froggatt and J. Moore, "High-spatial-resolution distributed strain measurement in optical fiber with Rayleigh scatter," *Applied optics*, vol. 37, no. 10, pp. 1735–1740, 1998.

[57] Z. Ding *et al.*, "Distributed optical fiber sensors based on optical frequency domain reflectometry: A review," *Sensors*, vol. 18, no. 4, p. 1072, 2018.

[58] K. Iiyama, M. Yasuda, and S. Takamiya, "Extended-range high-resolution FMCW reflectometry by means of electronically frequency-multiplied sampling signal generated from auxiliary interferometer," *IEICE transactions on electronics*, vol. 89, no. 6, pp. 823–829, 2006.

[59] B. J. Soller, D. K. Gifford, M. S. Wolfe, and M. E. Froggatt, "High resolution

optical frequency domain reflectometry for characterization of components and assemblies," *Optics express*, vol. 13, no. 2, pp. 666–674, 2005.

[60] E. D. Moore and R. R. McLeod, "Correction of sampling errors due to laser tuning rate fluctuations in swept-wavelength interferometry," *Optics express*, vol. 16, no. 17, pp. 13139–13149, 2008.

[61] T.-J. Ahn, J. Y. Lee, and D. Y. Kim, "Suppression of nonlinear frequency sweep in an optical frequency-domain reflectometer by use of Hilbert transformation," *Applied optics*, vol. 44, no. 35, pp. 7630–7634, 2005.

[62] T.-J. Ahn and D. Y. Kim, "Analysis of nonlinear frequency sweep in high-speed tunable laser sources using a self-homodyne measurement and Hilbert transformation," *Applied optics*, vol. 46, no. 13, pp. 2394–2400, 2007.

[63] J. Xing *et al.*, "A method based on time-scale factor for correcting the nonlinear frequency sweeping in an OFDR system," *IEEE Photonics Journal*, vol. 11, no. 3, pp. 1–8, 2019.

[64] K. Yüksel, M. Wuilpart, and P. Mégret, "Analysis and suppression of nonlinear frequency modulation in an optical frequency-domain reflectometer," *Optics express*, vol. 17, no. 7, pp. 5845–5851, 2009.

[65] Z. Ding *et al.*, "Note: Improving spatial resolution of optical frequency-domain reflectometry against frequency tuning nonlinearity using non-uniform fast Fourier transform," *Review of Scientific Instruments*, vol. 83, no. 6, 2012.

[66] X. Fan, Y. Koshikiya, and F. Ito, "Phase-noise-compensated optical frequency domain reflectometry with measurement range beyond laser coherence length realized using concatenative reference method," *Optics letters*, vol. 32, no. 22, pp. 3227–3229, 2007.

[67] X. Fan, Y. Koshikiya, and F. Ito, "Phase-noise-compensated optical frequency-domain reflectometry," *IEEE journal of quantum electronics*, vol. 45, no. 6, pp. 594–602, 2009.

[68] X. Fan, Y. Koshikiya, and F. Ito, "Centimeter-level spatial resolution over 40 km realized by bandwidth-division phase-noise-compensated OFDR," *Optics express*, vol. 19, no. 20, pp. 19122–19128, 2011.

[69] F. Ito, X. Fan, and Y. Koshikiya, “Long-range coherent OFDR with light source phase noise compensation,” *Journal of Lightwave Technology*, vol. 30, no. 8, pp. 1015–1024, 2011.

[70] Z. Zhang, X. Fan, M. Wu, and Z. He, “Phase-noise-compensated OFDR realized using hardware-adaptive algorithm for real-time processing,” *Journal of Lightwave Technology*, vol. 37, no. 11, pp. 2634–2640, 2019.

[71] Z. Ding *et al.*, “Compensation of laser frequency tuning nonlinearity of a long range OFDR using deskew filter,” *Optics express*, vol. 21, no. 3, pp. 3826–3834, 2013.

[72] Y. Du *et al.*, “Method for improving spatial resolution and amplitude by optimized deskew filter in long-range OFDR,” *IEEE Photonics Journal*, vol. 6, no. 5, pp. 1–11, 2014.

[73] J. Song, W. Li, P. Lu, Y. Xu, L. Chen, and X. Bao, “Long-range high spatial resolution distributed temperature and strain sensing based on optical frequency-domain reflectometry,” *IEEE Photonics Journal*, vol. 6, no. 3, pp. 1–8, 2014.

[74] J. Xiong, Z. Wang, J. Jiang, B. Han, and Y. Rao, “High sensitivity and large measurable range distributed acoustic sensing with Rayleigh-enhanced fiber,” *Optics Letters*, vol. 46, no. 11, pp. 2569–2572, 2021.

[75] H. Zhang, L. Teng, and Y. Dong, “Distributed Salinity Sensor With a Polyimide-Coated Photonic Crystal Fiber Based on Brillouin Dynamic Grating,” *J. Lightwave Technol.*, vol. 38, no. 18, pp. 5219–5224, 2020, doi: 10.1364/JLT.38.005219.

[76] H. Shi, G. Li, Z. Huang, J. Li, and Y. Zhang, “Study and application of a high-pressure water jet multi-functional flow test system,” *Review of Scientific Instruments*, vol. 86, no. 12, 2015.

[77] W.-Q. Feng, Z.-Y. Liu, H.-Y. Tam, and J.-H. Yin, “The pore water pressure sensor based on Sagnac interferometer with polarization-maintaining photonic crystal fiber for the geotechnical engineering,” *Measurement*, vol. 90, pp. 208–214, 2016.

[78] L. Teng *et al.*, “Temperature-compensated distributed hydrostatic pressure sensor

with a thin-diameter polarization-maintaining photonic crystal fiber based on Brillouin dynamic gratings," *Optics letters*, vol. 41, no. 18, pp. 4413–4416, 2016.

[79] Y. Dong, L. Qiu, Y. Lu, L. Teng, B. Wang, and Z. Zhu, "Sensitivity-enhanced distributed hydrostatic pressure sensor based on botda in single-mode fiber with double-layer polymer coatings," *Journal of lightwave technology*, vol. 38, no. 8, pp. 2564–2571, 2020.

[80] S. Mikhailov, L. Zhang, T. Geernaert, F. Berghmans, and L. Thévenaz, "Distributed hydrostatic pressure measurement using Phase-OTDR in a highly birefringent photonic crystal fiber," *Journal of Lightwave Technology*, vol. 37, no. 18, pp. 4496–4500, 2019.

[81] L. Zhang *et al.*, "Long-distance distributed pressure sensing based on frequency-scanned phase-sensitive optical time-domain reflectometry," *Optics Express*, vol. 29, no. 13, pp. 20487–20497, 2021.

[82] L. Qiu, D. Ba, D. Zhou, Q. Chu, Z. Zhu, and Y. Dong, "High-sensitivity dynamic distributed pressure sensing with frequency-scanning φ-OTDR," *Optics Letters*, vol. 47, no. 4, pp. 965–968, 2022.

[83] Y. Yan and others, "Dynamic distributed optical fiber sensors based on digital optical communication techniques," 2021.

[84] A. Masoudi and T. P. Newson, "Contributed Review: Distributed optical fibre dynamic strain sensing," *Review of scientific instruments*, vol. 87, no. 1, 2016.

[85] K.-I. Aoyama, K. Nakagawa, and T. Itoh, "Optical time domain reflectometry in a single-mode fiber," *IEEE Journal of Quantum Electronics*, vol. 17, no. 6, pp. 862–868, 1981.

[86] M. Nakazawa, "Rayleigh backscattering theory for single-mode optical fibers," *JOSA*, vol. 73, no. 9, pp. 1175–1180, 1983.

[87] P. Healey, "Statistics of Rayleigh backscatter from a single-mode fiber," *IEEE transactions on communications*, vol. 35, no. 2, pp. 210–214, 1987.

[88] P. Healey, "Statistics of Rayleigh backscatter from a single-mode optical fibre," *Electronics Letters*, vol. 6, no. 21, pp. 226–228, 1985.

[89] A. H. Hartog, *An introduction to distributed optical fibre sensors*. CRC press,

2017.

[90] R. K. Staubli and P. Gysel, “Statistical properties of single-mode fiber Rayleigh backscattered intensity and resulting detector current,” *IEEE Transactions on Communications*, vol. 40, no. 6, pp. 1091–1097, 1992.

[91] X. Lu, “Coherent Rayleigh time domain reflectometry,” EPFL, 2016.

[92] L. Zhang, “Distributed optical fiber sensing based on frequency-scanned phase-sensitive optical time-domain reflectometry,” EPFL, 2020.

[93] J. W. Goodman, *Speckle phenomena in optics: theory and applications*. Roberts and Company Publishers, 2007.

[94] G. Hocker, “Fiber-optic sensing of pressure and temperature,” *Applied optics*, vol. 18, no. 9, pp. 1445–1448, 1979.

[95] C. D. Butter and G. Hocker, “Fiber optics strain gauge,” *Applied optics*, vol. 17, no. 18, pp. 2867–2869, 1978.

[96] H. F. Martins, S. Martin-Lopez, P. Corredera, P. Salgado, O. Frazão, and M. González-Herráez, “Modulation instability-induced fading in phase-sensitive optical time-domain reflectometry,” *Optics letters*, vol. 38, no. 6, pp. 872–874, 2013.

[97] Z. Wang *et al.*, “Phase-sensitive optical time-domain reflectometry with Brillouin amplification,” *Optics letters*, vol. 39, no. 15, pp. 4313–4316, 2014.

[98] K. Kikuchi, “Fundamentals of coherent optical fiber communications,” *Journal of lightwave technology*, vol. 34, no. 1, pp. 157–179, 2015.

[99] Y. Dong, X. Chen, E. Liu, C. Fu, H. Zhang, and Z. Lu, “Quantitative measurement of dynamic nanostrain based on a phase-sensitive optical time domain reflectometer,” *Applied Optics*, vol. 55, no. 28, pp. 7810–7815, 2016.

[100] R. Hui, *Introduction to fiber-optic communications*. Academic Press, 2019.

[101] J. Xiong, Z. Wang, Y. Wu, H. Wu, and Y. Rao, “Long-distance distributed acoustic sensing utilizing negative frequency band,” *Optics Express*, vol. 28, no. 24, pp. 35844–35856, 2020.

[102] D. Chen, Q. Liu, and Z. He, “Phase-detection distributed fiber-optic vibration sensor without fading-noise based on time-gated digital OFDR,” *Optics express*,

vol. 25, no. 7, pp. 8315–8325, 2017.

[103] D. Chen, Q. Liu, and Z. He, “108-km Distributed Acoustic Sensor With 220-pϵ/√Hz Strain Resolution and 5-m Spatial Resolution,” *Journal of Lightwave Technology*, vol. 37, no. 18, pp. 4462–4468, 2019.

[104] S. Hosoda, T. Suga, N. Shikama, and K. Mizuno, “Global surface layer salinity change detected by Argo and its implication for hydrological cycle intensification,” *Journal of Oceanography*, vol. 65, pp. 579–586, 2009.

[105] P. J. Durack and S. E. Wijffels, “Fifty-year trends in global ocean salinities and their relationship to broad-scale warming,” *Journal of Climate*, vol. 23, no. 16, pp. 4342–4362, 2010.

[106] R. W. SChmitt, “Salinity and the global water cycle,” *Oceanography*, vol. 21, no. 1, pp. 12–19, 2008.

[107] R. A. Cox, F. Culkin, and J. Riley, “The electrical conductivity/chlorinity relationship in natural sea water,” in *Deep Sea Research and Oceanographic Abstracts*, Elsevier, 1967, pp. 203–220.

[108] H. Minato, Y. Kakui, A. Nishimoto, and M. Nanjo, “Remote refractive index difference meter for salinity sensor,” *IEEE Transactions on Instrumentation and Measurement*, vol. 38, no. 2, pp. 608–612, 1989.

[109] A. W. Domanski, M. Roszko, and M. Swillo, “Compact optical fiber refractive index differential sensor for salinity measurements,” in *IEEE Instrumentation and Measurement Technology Conference Sensing, Processing, Networking. IMTC Proceedings*, IEEE, 1997, pp. 953–956.

[110] J. Cong, X. Zhang, K. Chen, and J. Xu, “Fiber optic Bragg grating sensor based on hydrogels for measuring salinity,” *Sensors and Actuators B: Chemical*, vol. 87, no. 3, pp. 487–490, 2002.

[111] L. Men, P. Lu, and Q. Chen, “A multiplexed fiber Bragg grating sensor for simultaneous salinity and temperature measurement,” *Journal of Applied Physics*, vol. 103, no. 5, p. 053107, 2008.

[112] D. A. Pereira, O. Frazao, and J. L. Santos, “Fiber Bragg grating sensing system for simultaneous measurement of salinity and temperature,” *Optical Engineering*,

vol. 43, no. 2, pp. 299–304, 2004.

[113] L. V. Nguyen, M. Vasiliev, and K. Alameh, “Water salinity fiber sensor with selectable sensitivity using a liquid-fillable composite in-fiber Fabry-Perot cavity,” in *7th International Symposium on High-capacity Optical Networks and Enabling Technologies*, 2010, pp. 161–165. doi: 10.1109/HONET.2010.5715765.

[114] X. Zhang and W. Peng, “Temperature-independent fiber salinity sensor based on Fabry-Perot interference,” *Optics express*, vol. 23, no. 8, pp. 10353–10358, 2015.

[115] X. Wei, Y. Peng, X. Chen, S. Zhang, and Y. Zhao, “Optimization of tapered optical fiber sensor based on SPR for high sensitivity salinity measurement,” *Optical Fiber Technology*, vol. 78, p. 103309, 2023.

[116] N. Díaz-Herrera, O. Esteban, M. Navarrete, M. Le Haitre, and A. González-Cano, “In situ salinity measurements in seawater with a fibre-optic probe,” *Measurement Science and Technology*, vol. 17, no. 8, p. 2227, 2006.

[117] D. J. Gentleman and K. S. Booksh, “Determining salinity using a multimode fiber optic surface plasmon resonance dip-probe,” *Talanta*, vol. 68, no. 3, pp. 504–515, 2006.

[118] Z. Lin, R. Lv, Y. Zhao, and H. Zheng, “High-sensitivity salinity measurement sensor based on no-core fiber,” *Sensors and Actuators A: Physical*, vol. 305, p. 111947, 2020.

[119] C. Wu, B.-O. Guan, C. Lu, and H.-Y. Tam, “Salinity sensor based on polyimide-coated photonic crystal fiber,” *Optics express*, vol. 19, no. 21, pp. 20003–20008, 2011.

[120] J. Wang and B. Chen, “Experimental research of optical fiber sensor for salinity measurement,” *Sensors and Actuators A: Physical*, vol. 184, pp. 53–56, 2012.

[121] D. Vigneswaran, N. Ayyanar, M. Sharma, M. Sumathi, M. Rajan, and K. Porsezian, “Salinity sensor using photonic crystal fiber,” *Sensors and Actuators A: Physical*, vol. 269, pp. 22–28, 2018.

[122] J.-Y. Guo *et al.*, “Groundwater salinity sensing using PI-FBG with improved capillary coating method,” *Measurement*, p. 113223, 2023.

[123] M. Galal, S. Sebastian, Z. Yang, L. Zhang, S. Zaslawski, and L. Thévenaz, “On

the measurement accuracy of coherent Rayleigh-based distributed sensors," *Optics Express*, vol. 29, no. 26, pp. 42538–42552, 2021.

[124] G. C. Carter, "Coherence and time delay estimation," *Proceedings of the IEEE*, vol. 75, no. 2, pp. 236–255, 1987.

[125] G. Carter, "Time delay estimation for passive sonar signal processing," *IEEE Transactions on Acoustics, Speech, and Signal Processing*, vol. 29, no. 3, pp. 463–470, 1981.

[126] I. Cespedes, Y. Huang, J. Ophir, and S. Spratt, "Methods for estimation of subsample time delays of digitized echo signals," *Ultrasonic imaging*, vol. 17, no. 2, pp. 142–171, 1995.

[127] A. Quazi, "An overview on the time delay estimate in active and passive systems for target localization," *IEEE Transactions on Acoustics, Speech, and Signal Processing*, vol. 29, no. 3, pp. 527–533, 1981.

[128] D. Luo, J. Ma, Z. Ibrahim, and Z. Ismail, "Etched FBG coated with polyimide for simultaneous detection the salinity and temperature," *Optics Communications*, vol. 392, pp. 218–222, 2017.

[129] S. Wang, T. Liu, X. Wang, Y. Liao, J. Wang, and J. Wen, "Hybrid structure Mach-Zehnder interferometer based on silica and fluorinated polyimide microfibers for temperature or salinity sensing in seawater," *Measurement*, vol. 135, pp. 527–536, 2019.

[130] E. Siyu, Y.-N. Zhang, B. Han, W. Zheng, Q.-L. Wu, and H.-K. Zheng, "Two-channel surface plasmon resonance sensor for simultaneous measurement of seawater salinity and temperature," *IEEE Transactions on Instrumentation and Measurement*, vol. 69, no. 9, pp. 7191–7199, 2020.

[131] Y. Zhi, S. Pengxiang, and L. Yongqian, "Research on COTDR for measuring distributed temperature and strain," in *2011 Second International Conference on Mechanic Automation and Control Engineering*, IEEE, 2011, pp. 590–593.

[132] X. Lu, M. A. Soto, and L. Thévenaz, "Temperature-strain discrimination in distributed optical fiber sensing using phase-sensitive optical time-domain reflectometry," *Optics express*, vol. 25, no. 14, pp. 16059–16071, 2017.

[133] J. R. Taylor and W. Thompson, *An introduction to error analysis: the study of uncertainties in physical measurements*, vol. 2. Springer, 1982.

[134] Z. Ma *et al.*, "Phase drift noise suppression for coherent-OTDR sensing based on heterogeneous dual-sideband LFM pulse," *Applied Physics Express*, vol. 13, no. 8, p. 082002, 2020.

[135] Q. Jiang, H. Du, D. Hu, and M. Yang, "Hydraulic pressure sensor based on fiber Bragg grating," *Optical engineering*, vol. 50, no. 6, pp. 064401–064401, 2011.

[136] Y.-F. Gu, Y. Zhao, R.-Q. Lv, and Y. Yang, "A practical FBG sensor based on a thin-walled cylinder for hydraulic pressure measurement," *IEEE Photonics Technology Letters*, vol. 28, no. 22, pp. 2569–2572, 2016.

[137] L. Htein, Z. Liu, D. Gunawardena, and H.-Y. Tam, "Single-ring suspended fiber for Bragg grating based hydrostatic pressure sensing," *Optics express*, vol. 27, no. 7, pp. 9655–9664, 2019.

[138] L. Jin, B.-O. Guan, and H. Wei, "Sensitivity characteristics of Fabry-Perot pressure sensors based on hollow-core microstructured fibers," *Journal of lightwave technology*, vol. 31, no. 15, pp. 2526–2532, 2013.

[139] D. P. Duarte, N. Alberto, L. Bilro, and R. Nogueira, "Theoretical design of a high sensitivity SPR-based optical fiber pressure sensor," *Journal of Lightwave Technology*, vol. 33, no. 22, pp. 4606–4611, 2015.

[140] B. Budiansky, D. Drucker, G. Kino, and J. Rice, "Pressure sensitivity of a clad optical fiber," *Applied optics*, vol. 18, no. 24, pp. 4085–4088, 1979.

[141] L. Schenato, A. Galtarossa, A. Pasuto, and L. Palmieri, "Distributed optical fiber pressure sensors," *Optical Fiber Technology*, vol. 58, p. 102239, 2020.